

# Mechanical Effects of Flow on CO<sub>2</sub> Corrosion Inhibition of Carbon Steel Pipelines

A dissertation presented to  
the faculty of  
the Russ College of Engineering and Technology of Ohio University

In partial fulfillment  
of the requirements for the degree  
Doctor of Philosophy

Wei Li

August 2016

© 2016 Wei Li. All Rights Reserved.

This dissertation titled  
Mechanical Effects of Flow on CO<sub>2</sub> Corrosion Inhibition of Carbon Steel Pipelines

by  
WEI LI

has been approved for  
the Department of Chemical and Biomolecular Engineering  
and the Russ College of Engineering and Technology by

Srdjan Nesic  
Professor of Chemical and Biomolecular Engineering

Dennis Irwin  
Dean, Russ College of Engineering and Technology

### **Abstract**

LI, WEI, Ph.D., August 2016, Chemical Engineering

#### Mechanical Effects of Flow on CO<sub>2</sub> Corrosion Inhibition of Carbon Steel Pipelines

Director of Dissertation: Srdjan Nestic

Transportation of multiphase fluids using carbon steel pipelines is ubiquitous in the oil and gas industry. These pipelines are prone to internal corrosion when exposed to an aqueous CO<sub>2</sub> environment. The mitigation of CO<sub>2</sub> corrosion can be achieved by the use of organic corrosion inhibitors or by reliance on formation of protective corrosion product layers. However, the mechanisms for their potential failure in flow conditions are still being debated.

Wall shear stress induced by turbulent multiphase flow is considered an important parameter in CO<sub>2</sub> corrosion as it has been claimed to be responsible for the removal of protective corrosion product layers and corrosion inhibitor films. In this study, a floating element wall probe was used to directly measure the wall shear stresses in single-phase and horizontal gas-liquid two-phase flow, instead of the more common indirect measurement of the wall shear stress. Wall shear stress measurements were complemented by high speed video camera recordings of the flow field. In single-phase pipe and channel flow, the wall shear stress was in good agreement with empirical shear stress calculations. In two-phase pipe flow, video-recorded observations confirmed that the high wall shear stress pulses captured by the probe in the slug flow pattern were in sync with the passage of liquid slugs; the highest measured wall shear stress values were of the order of 100 Pa. Wall shear stress values in the slug body varied along the inner

pipe circumference with the top of the pipe having the highest values and the bottom of the pipe having the lowest values. The maximum wall shear stress measured was about 2 to 4 times higher than the calculated mean wall shear stress in the slug body, obtained by using the mixture velocity, which can serve as a guideline for slug flow modeling. Findings suggest that the wall shear stress alone, produced in single-phase and multiphase flow patterns covered in the present study, is insufficient to mechanically damage the protective corrosion product layers or corrosion inhibitor films.

In addition, corrosion experiments with an imidazoline-based inhibitor were performed on X65 pipeline steel in a thin channel flow cell (TCFC). Local flow velocities were up to 28 m/s with wall shear stresses up to 4.8 kPa. Electrochemical measurements, surface analysis and computational fluid dynamics (CFD) were used as diagnostic tools. Localized corrosion was observed on a protrusion in the flow cell and depended on local flow conditions and inhibitor concentration. Overall, the wall shear stress was unable to affect performance of corrosion inhibitors. However, the low static pressure at the protrusion caused cavitation with bubble collapse leading to accelerated desorption of inhibitor from the steel surface, which explained the localized corrosion. An excess amount of inhibitor was found to mitigate localized corrosion by cavitation.

## **Dedication**

*To my love, my family and my friends.*

## **Acknowledgments**

I am indebted to many individuals who have helped me during my PhD journey, personally and professionally. First and foremost, I would like to express my genuine gratitude to my advisor, Dr. Srdjan Nesic, for his academic advice and constant support throughout my entire graduate studies. His dedication and energy to research and life serve as my role model and will continue to inspire me, which would be my lifelong fortune.

Many thanks also go to my dissertation committee members, Drs. David Young, Yoon-Seok Choi, Marc Singer, Douglas Green and Lauren McMills for their academic assistance and time.

I am deeply grateful to my mentors, Drs. B.F.M. Pots, Luciano Paolinelli and Sumit Sharma for their invaluable advice and discussion related to my research.

Thank you to all members of the Institute for Corrosion and Multiphase Technology. Particularly, I would like to thank my research group leader, Dr. Bruce Brown, for his technical support and constant availability during my research program. Thank you to the technical staff for their support during my experimental research, especially Alexis Barxias, Daniel Cain, Phil Bullington and Cody Shafer. Thanks to Becky Gill for administrative support.

Many thanks go to my fellow colleagues at the institute for their help and support. I particularly thank Drs. Kok Eng Kee, Channa De Silva and Xiankang Zhong for their help with my experimental work. In addition, I would like to acknowledge

Dr. Fardis Najafifard, Dr. Baotang Zhuang, Dr. Haijun Hu and Yingrodge Suntiwuth for their assistance on computer simulation.

Thank you to Dr. David Young and Lisa Mosier for their help in proofreading for this dissertation.

Finally, I am indebted to my parents, my love and other family members for their support, encouragement, prayers and patience throughout my long journey of pursuing graduate studies.

## Table of Contents

	Page
Abstract.....	3
Dedication.....	5
Acknowledgments.....	6
List of Tables .....	12
List of Figures .....	13
List of Abbreviations .....	20
Chapter 1: Introduction.....	23
Chapter 2: Background and Literature Review .....	27
2.1 Basics of CO <sub>2</sub> Corrosion .....	27
2.1.1 CO <sub>2</sub> corrosion mechanisms .....	28
2.1.2 Mitigation of CO <sub>2</sub> corrosion.....	30
2.2 Flow Patterns in Gas-Liquid Two-Phase Flow .....	39
2.3 Effects of Flow on Mitigation of CO <sub>2</sub> Corrosion.....	42
2.3.1 Effect of mass transfer.....	43
2.3.2 Effect of mechanical forces.....	45
2.3.3 Other miscellaneous effects found in multiphase flow .....	48
2.4 Wall Shear Stress Measurements .....	49
2.4.1 Direct measurements .....	49
2.4.2 Indirect measurements.....	53
Chapter 3: Research Objectives .....	59
Chapter 4: Experimental Methodology.....	61
4.1 Physical Measurement of Wall Shear Stress.....	61

	9
4.2 Instrumentation and Methods for Flow Tests.....	64
4.2.1 Equipment for single-phase flow .....	64
4.2.2 Equipment for gas-liquid two-phase flow .....	67
4.2.3 Equipment for flow visualization .....	68
4.2.4 Computational fluid dynamics (CFD).....	69
4.3 Electrochemical Characterization Techniques for Corrosion Tests.....	69
4.4 Techniques for Surface Characterization .....	70
Chapter 5: Direct Wall Shear Stress Measurements in Gas-Liquid Two-Phase Flow .....	71
5.1 Introduction .....	71
5.2 Experimental Methodology.....	71
5.3 Wall Shear Stress Measurements in Single-Phase Flow .....	74
5.4 Wall Shear Stress Measurements in Gas-Liquid Two-Phase Horizontal Pipe Flow .....	80
5.4.1 Wall shear stress measurements in slug flow .....	80
5.4.2 Assessment of the location with the highest wall shear stress in a slug.....	98
5.4.3 Determination of slug frequency.....	101
5.4.4 Wall shear stress measurements in stratified flow and annular flow .....	106
5.5 Discussion .....	109
5.6 Summary .....	112
Chapter 6: Mechanical Effects of Flow on CO <sub>2</sub> Corrosion Inhibition.....	114
6.1 Introduction .....	114
6.2 Experimental .....	114
6.2.1 Flow system for corrosion tests.....	114
6.2.2 Corrosion specimens .....	115

	10
6.2.3 Experimental procedures .....	119
6.3 Experimental Results.....	122
6.3.1 Corrosion tests without inhibitor.....	122
6.3.2 Corrosion tests with inhibitor .....	127
6.3.3 Effect of oxygen ingress on corrosion inhibition .....	134
6.3.4 Effect of wall shear stress on corrosion inhibition .....	142
6.3.5 Effect of cavitation on corrosion inhibition .....	145
6.3.6 Mitigation of cavitation induced localized corrosion.....	151
6.4 Discussion .....	157
6.4.1 Effect of pre-corrosion on corrosion inhibition at high flow velocity .....	158
6.4.2 B value at high flow velocity .....	158
6.4.3 Mechanisms of flow cavitation induced pitting corrosion and its mitigation .....	160
6.4.4 Microscopic expressions for continuum hydrodynamics .....	170
6.5 Summary .....	171
Chapter 7: Conclusions and Recommendations .....	173
7.1 Conclusions .....	173
7.2 Recommendations .....	175
References.....	177
Appendix 1. Measurement of the Mass Transfer Limiting Current Using the Ferricyanide-Ferrocyanide Couple.....	191
Appendix 2. Procedures for Calibrating the Paddlewheel Flow Meter and the Orifice Plate Flow Meter.....	193
Appendix 3. Calculation of Corrosion Rate by Weight Loss and Linear Polarization Resistance .....	196

Appendix 4. Calculation of the Absolute Pressure at the Inlet of the CFD Simulation for  
Protrusion in the Thin Channel Flow Cell ..... 198

## List of Tables

	Page
Table 2-1: Key chemical reactions of aqueous CO <sub>2</sub> corrosion and the corresponding chemical equilibrium expressions.....	29
Table 2-2: Key electrochemical reactions of aqueous CO <sub>2</sub> corrosion.....	29
Table 2-3: Chemical formulation of the model inhibitor K1 [wt.%].....	39
Table 4-1: Typical parameter settings for electrochemical measurements.....	70
Table 5-1: Test matrix for single-phase flow.....	73
Table 5-2: Test matrix for gas-liquid two-phase flow.....	73
Table 5-3: Wall shear stress measurements for slug flow in the 4 inch pipe loop.....	85
Table 5-4: Maximum local liquid velocity ( $V_{max}$ ) calculated from the video data in the slug body, for 4 inch pipe loop.....	95
Table 5-5: Selected empirical correlations for slug frequency determination [82,84,85].....	104
Table 5-6: Error statistics for slug frequency: (predicted – measured)/measured, for the data produced by using different empirical correlations.....	105
Table 5-7: WSS data measured for annular flow at the bottom and on the side wall of the 6 inch pipe.....	109
Table 6-1: Chemical analysis [wt.%] of API 5L X65 carbon steel.....	116
Table 6-2: Test matrix for corrosion inhibition test with high flow velocity.....	120

## List of Figures

	Page
Figure 2-1: A top view SEM image of a steel surface covered by a $\text{FeCO}_3$ layer. $80^\circ\text{C}$ , 0.53 bar $\text{CO}_2$ , pH 7.8, stagnant. ....	32
Figure 2-2: A cross-sectional side view TEM image of a $\text{FeCO}_3$ covered steel surface. $80^\circ\text{C}$ , 0.53 bar $\text{CO}_2$ , pH 7.1, stagnant. The specimen was coated with Au and Pt during specimen preparation. ....	32
Figure 2-3: Adsorption mechanisms of ionic surfactants on the charged substrate surface (adapted from [54]). ....	37
Figure 2-4: Curve of surface tension – surfactant concentration. ....	37
Figure 2-5: Molecular structure of TOFA/DETA imidazolium ion. ....	39
Figure 2-6: Schematics of flow patterns in horizontal gas-liquid two-phase flow (adapted from [62]). ....	41
Figure 2-7: A flow pattern map for horizontal gas-liquid two-phase flow. $\text{H}_2\text{O} / \text{CO}_2$ , $25^\circ\text{C}$ , 1 bar, 4 inch ID pipe (generated by an in-house gas-liquid flow model [63]). ....	42
Figure 2-8: Potentiodynamic polarization curves measuring the mass transfer limiting currents of the ferri/ferrocyanide. Nickel RCE electrode (a diameter of 12 mm and length of 14 mm), $25^\circ\text{C}$ , 2 M NaOH, 0.01 M $\text{K}_4[\text{Fe}(\text{CN})_6] / \text{K}_3[\text{Fe}(\text{CN})_6]$ , 1 bar $\text{N}_2$ . ....	44
Figure 2-9: Classification of methods for wall shear stress measurements (adapted from [68–70]). ....	49
Figure 2-10: Schematic of classical floating element WSS sensor (adapted from [69]). ..	50
Figure 2-11: Schematic of heat or mass transfer WSS sensor (adapted from [28]). ....	55
Figure 2-12: Schematic of laser-based WSS sensor (adapted from [70]). ....	57
Figure 4-1: (A) Schematic of a floating element WSS measurement system showing sample measurement; (B) schematic diagram of WSS probe body (by Lenterra with permission). ....	62
Figure 4-2: Visual representations of: (A) thin channel flow cell assembly and (B) zoomed-in view of the bottom plate of the test section (top lid not shown). ....	65
Figure 4-3: Representation of 10.2 cm ID (4 inch) pipe flow loop. ....	66

Figure 4-4: Schematic of the WSS probe holder flush-mounted to the pipe wall. ....	67
Figure 4-5: Representation of 15.2 cm ID (6 inch) once-through pipe system. ....	68
Figure 5-1: Tested flow conditions for WSS measurements in a horizontal two-phase flow pattern map [63] for 1 bar, 25°C, CO <sub>2</sub> -water, and 4-inch pipe loop. ....	74
Figure 5-2: Comparison of measured WSS values with Patel calculations for channel flow (h=3 mm). ....	76
Figure 5-3: Comparison of measured WSS values with calculations for pipe flow (ID=0.102 m). ....	76
Figure 5-4: ANSYS geometry for the test section of the thin channel flow cell. ....	78
Figure 5-5: Mesh structure in the thin channel flow cell, a view from z-direction. ....	78
Figure 5-6: WSS distribution at the port locations by CFD simulation. 25°C, 9.5 m/s in the thin channel flow cell. ....	79
Figure 5-7: Comparison of WSS values obtained by different methods. ....	79
Figure 5-8: Wall shear stress measurement at the bottom of the 4 inch pipe for $V_{sl}=2.0$ m/s, $V_{sg} = 2.1$ m/s: (A) the full recording sequence; (B) data between 32 and 38 seconds (See Figure 5-20 for the synchronized video frames of the labeled peaks). ....	82
Figure 5-9: Wall shear stress measurement at the top of the 4 inch pipe loop for $V_{sl} = 2.0$ m/s, $V_{sg} = 2.6$ m/s: (A) the full recording sequence; (B) data between 70 and 80 seconds (See Figure 5-21 and Figure 5-22 for the synchronized video frames of the labeled peaks). ....	82
Figure 5-10: Wall shear stress measurement at the sidewall of the 4 inch pipe loop for $V_{sl} = 0.3$ m/s, $V_{sg} = 2.6$ m/s: (A) the full recording sequence; (B) data between 160 and 200 seconds. ....	83
Figure 5-11: $\tau_{max}$ (Pa) shown next to markers for slug flow measured at the bottom of the pipe overlain with the flow pattern map [63], at 1 bar, 25°C, CO <sub>2</sub> -water, and in the 4-inch loop. ....	86
Figure 5-12: $\tau_{max}$ (Pa) shown next to markers for slug flow measured at the top of the pipe overlain with the flow pattern map [63], at 1 bar, 25°C, CO <sub>2</sub> -water, and in the 4-inch loop. ....	86
Figure 5-13: $\tau_{max}$ (Pa) shown next to markers for slug flow measured at the sidewall overlain with the flow pattern map [63], at 1 bar, 25°C, CO <sub>2</sub> -water, and in the 4-inch loop. ....	87

- Figure 5-14: Comparison between measured maximum WSS values and calculated mean slug WSS values from Equation (5-12) by using mixture velocity ( $V_m$ ), for 4-inch loop.89
- Figure 5-15: Illustration of calculating the in situ liquid velocities in a slug body. Time difference between frames  $\Delta t = 0.003$  s.  $V_{sl}=1.0$  m/s,  $V_{sg}= 0.6$  m/s..... 91
- Figure 5-16: Illustration of tracking the tracer in the video frame at  $t = \Delta t$ ..... 93
- Figure 5-17: Illustration of tracking the tracer in two video frames using the cross correlation method. (A): the matrix **A** containing the tracer in grayscale at  $t = 0$  s (marked by blue rectangle in Figure 5-15); (B) the calculated correlation coefficients between the matrix **A** and the moving matrix **B**; (C) the moving matrix **B** with the maximum correlation to matrix **A** in grayscale at  $t = 0.003$  s..... 94
- Figure 5-18: Comparison between maximum local liquid velocity ( $V_{max}$ ) in the slug body calculated from the video data and the mixture velocity ( $V_m$ ) at each flow condition, for 4 inch pipe loop..... 96
- Figure 5-19: Comparison between measured maximum WSS values and calculated maximum slug WSS values from Equation (5-12) by using  $V_{max}$  from the video data, for 4 inch pipe loop..... 97
- Figure 5-20: Video frames of slug passages corresponding to the three WSS measurement peaks marked in Figure 5-8(B),  $V_{sl} = 2.0$  m/s,  $V_{sg} = 2.1$  m/s: 1. the WSS probe is at the pipe bottom; 2. a scale tape of 2 cm long. .... 99
- Figure 5-21: Evolution of the WSS fluctuations with synchronized video frames of the slug around 74.29 s marked in Figure 5-9(B),  $V_{sl} = 2.0$  m/s,  $V_{sg} = 2.6$  m/s, 4 inch pipe. .... 100
- Figure 5-22: Video frames of slug passages corresponding to the three WSS measurement peaks marked in Figure 5-9(B),  $V_{sl} = 2.0$  m/s,  $V_{sg} = 2.6$  m/s: 1. the WSS probe is at the pipe top; 2. a scale tape of 2 cm long..... 101
- Figure 5-23: Comparison of measured slug frequencies by different methods (video data: hollow markers; WSS data: solid black markers) with the data of Heywood and Richardson (1979) [82] (solid gray markers)..... 103
- Figure 5-24: Comparison of measured slug frequencies with the Heywood correlation: (A) using the pipe diameter of this study; (B) using the pipe diameter of 42 mm. .... 106
- Figure 5-25: Wall shear stress measurement at the bottom of the 4 inch pipe for stratified flow at  $V_{sl} = 0.1$  m/s,  $V_{sg} = 6.1$  m/s: (A) the full recording sequence; (B) a typical video frame at this condition. .... 107

- Figure 5-26: Wall shear stress measurement at the bottom of the 6 inch pipe for annular flow at  $V_{sl} = 0.2$  m/s,  $V_{sg} = 42.2$  m/s: (A) the full recording sequence; (B) a typical video frame at this condition (1: the WSS probe location; 2: a scale tape of 2 cm long)..... 108
- Figure 6-1: Specification and flow orientation for flat weight loss specimens. Left: side view; right: top view. .... 116
- Figure 6-2: Specification and flow orientation of Specimen 3, protrusion weight loss specimen: left: side view; right: top view. .... 117
- Figure 6-3: Configuration of the electrochemical probe..... 118
- Figure 6-4: Location arrangement of the specimens in the TCFC..... 119
- Figure 6-5: LPR corrosion rate for blank test,  $B = 65$  mV. 1 wt.% NaCl, pH 5, 0.97 bar  $CO_2$ , 25°C, 16 m/s, API 5L X65 carbon steel, 4 ppb to 30 ppb  $O_2$ ..... 124
- Figure 6-6: Profilometry results of protrusion Specimen 3 after the blank test. A: contour of the surface depth; B: line pattern depth scan of the surface marked by the red straight line in A. 1 wt.% NaCl, pH 5, 0.97 bar  $CO_2$ , 25°C, 16 m/s, 4 day, X65, 4 ppb to 30 ppb  $O_2$ . .... 125
- Figure 6-7: SEM images of protrusion Specimen 3 after the blank test. First row: 50X magnification; second row: 1000X magnification. Physical locations are defined by using 5 numbered individual regions in Figure 6-2. 1 wt.% NaCl, pH 5, 0.97 bar  $CO_2$ , 25°C, 16 m/s, 4 day test duration, X65, 4 ppb to 30 ppb  $O_2$ ..... 126
- Figure 6-8: EDS analysis of flat Specimen 2 (150 grit) after the blank test. 1 wt.% NaCl, pH 5, 0.97 bar  $CO_2$ , 25°C, 16 m/s, 4 day, X65, 4 ppb to 30 ppb  $O_2$ ..... 127
- Figure 6-9: LPR corrosion rate for blank and 72 ppm<sub>v</sub> TOFA imidazoline inhibitor tests,  $B = 65$  mV. 1 wt.% NaCl, pH 5, 0.97 bar  $CO_2$ , 25°C, 16 m/s, 4 day test duration, X65, 4 ppb to 30 ppb  $O_2$ . .... 128
- Figure 6-10: SEM images of flat Specimen 1 (600 grit finish) and Specimen 2 (150 grit finish) at 1000X magnification. 1 wt.% NaCl, pH 5, 0.97 bar  $CO_2$ , 25°C, 72 ppm<sub>v</sub> inhibitor, 16 m/s, 4 day test duration, X65, 4 ppb to 30 ppb  $O_2$ : A. Specimen 1 before test; B. Specimen 1 after test; C. Specimen 2 before test; D. Specimen 2 after test..... 129
- Figure 6-11: Profilometry results of flat Specimen 1 (600 grit finish) after the test. A: contour of the surface depth; B: line pattern depth scan of the surface marked by the red straight line in A..... 130
- Figure 6-12: Profilometry results of flat Specimen 2 (150 grit finish) after the test. A: contour of the surface depth; B: line pattern depth scan of the surface marked by the red straight line in A..... 130

- Figure 6-13: SEM images of protrusion Specimen 3. Before test: 1st row at 50X magnification. After test: 2nd row at 50X magnification; 3rd row at 1000X magnification. Physical locations are defined by using 5 numbered individual regions in Figure 6-2. 1 wt.% NaCl, pH 5, 0.97 bar CO<sub>2</sub>, 25°C, 72 ppm<sub>v</sub> inhibitor, 16 m/s, 4 day test duration, X65, 4 ppb to 30 ppb O<sub>2</sub>. ..... 131
- Figure 6-14: (A): Profilometry image of protrusion Specimen 3 after experiment on the top of protrusion, region 3 in Figure 6-2; (B): line pattern depth scan of the dotted red line marked in (A). 1 wt.% NaCl, pH 5, 0.97 bar CO<sub>2</sub>, 25°C, 72 ppm<sub>v</sub> inhibitor, 16 m/s, 4 day test duration, X65, 4 ppb to 30 ppb O<sub>2</sub>. ..... 132
- Figure 6-15: EDS analysis of protrusion Specimen 3 after test on the top of protrusion, region 3 in Figure 6-2. A: inside a pit; B. the surrounding flat area above the pit. .... 133
- Figure 6-16: LPR corrosion rate for 72 ppm<sub>v</sub> inhibitor tests with varied levels of O<sub>2</sub> concentration, B = 65 mV. 1 wt.% NaCl, pH 5, 0.97 bar CO<sub>2</sub>, 25°C, 16 m/s, 4 day test duration, X65. .... 135
- Figure 6-17: SEM images of flat Specimen 1 (600 grit finish) and Specimen 2 (150 grit finish) at 1000X magnification. 1 wt.% NaCl, pH 5, 0.97 bar CO<sub>2</sub>, 25°C, 72 ppm<sub>v</sub> inhibitor, 16 m/s, 4 day test duration, X65, O<sub>2</sub> < 2 ppb: A. Specimen 1 before test; B. Specimen 1 after test; C. Specimen 2 before test; D. Specimen 2 after test. .... 136
- Figure 6-18: SEM images of protrusion Specimen 3. Before test: 1st row at 50X magnification. After test: 2nd row at 50X magnification; 3rd row at 1000X magnification. Physical locations are defined by using 5 numbered individual regions in Figure 6-2. 1 wt.% NaCl, pH 5, 0.97 bar CO<sub>2</sub>, 25°C, 72 ppm<sub>v</sub> inhibitor, 16 m/s, 4 day test duration, X65, O<sub>2</sub> < 2 ppb. .... 137
- Figure 6-19: (A): Profilometry image of protrusion Specimen 3 after experiment on top of protrusion, region 3 in Figure 6-2; (B): line pattern depth scan marked by the dotted red line in (A). 1 wt.% NaCl, pH 5, 0.97 bar CO<sub>2</sub>, 25°C, 72 ppm<sub>v</sub> inhibitor, 16 m/s, 4 day test duration, X65, O<sub>2</sub> < 2 ppb. .... 138
- Figure 6-20: EDS analysis of flat Specimen 1 (600 grit finish). A: before experiment; B. after experiment. 1 wt.% NaCl, pH 5, 0.97 bar CO<sub>2</sub>, 25°C, 72 ppm<sub>v</sub> inhibitor, 16 m/s, 4 day test duration, X65, O<sub>2</sub> < 2 ppb. .... 139
- Figure 6-21: EDS analysis of flat Specimen 2 (150 grit finish). A: before experiment; B. after experiment. 1 wt.% NaCl, pH 5, 0.97 bar CO<sub>2</sub>, 25°C, 72 ppm<sub>v</sub> inhibitor, 16 m/s, 4 day test duration, X65, O<sub>2</sub> < 2 ppb. .... 140
- Figure 6-22: EDS analysis of protrusion Specimen 3. A: before experiment; B. after experiment, in a pit at the top of protrusion, region 3 in Figure 6-2. 1 wt.% NaCl, pH 5, 0.97 bar CO<sub>2</sub>, 25°C, 72 ppm<sub>v</sub> inhibitor, 16 m/s, 4 day test duration, X65, O<sub>2</sub> < 2 ppb. . 141

Figure 6-23: Schematic of the CFD simulation geometry with the symmetric plane outlined (red lines).....	142
Figure 6-24: Flow velocity magnitude distribution on the symmetric plane.....	144
Figure 6-25: Wall shear stress distribution at the bottom plate of the TCFC near the specimen protrusion.....	144
Figure 6-26: Wall shear stress distribution: A. on the symmetric plane; B. on the bottom wall of the symmetric plane.....	145
Figure 6-27: Gauge pressure distribution: A. on the symmetric plane; B. on the bottom wall of the symmetric plane.....	146
Figure 6-28: LPR corrosion rate for 72 ppm <sub>v</sub> inhibitor tests with changes of the protrusion specimen location, B = 65 mV. 1 wt.% NaCl, pH 5, 0.97 bar CO <sub>2</sub> , 25°C, 16 m/s, 4 day test duration, X65, O <sub>2</sub> < 2 ppb. ....	149
Figure 6-29: SEM images of flat Specimen 1 (600 grit finish) at 1000X magnification. 1 wt.% NaCl, pH 5, 0.97 bar CO <sub>2</sub> , 25°C, 72 ppm <sub>v</sub> inhibitor, 16 m/s, 4 day test duration, X65, O <sub>2</sub> < 2ppb: A. Specimen 1 before test; B. Specimen 1 after test. ....	149
Figure 6-30: SEM images of protrusion Specimen 3 on the most upstream port in the TCFC (port 1). Before test: 1st row at 50X magnification. After test: 2nd row at 50X magnification; 3rd row at 1000X magnification. Physical locations are defined by using 5 numbered individual regions in Figure 6-2. 1 wt.% NaCl, pH 5, 0.97 bar CO <sub>2</sub> , 25°C, 72 ppm <sub>v</sub> inhibitor, 16 m/s, 4 day test duration, X65, O <sub>2</sub> < 2 ppb. ....	150
Figure 6-31: LPR corrosion rate for 720 ppm <sub>v</sub> inhibitor test, B = 65 mV. 1 wt.% NaCl, pH 5, 0.97 bar CO <sub>2</sub> , 25°C, 16 m/s, 4 day test duration, X65. ....	152
Figure 6-32: SEM images of flat Specimen 1 (600 grit finish) and Specimen 2 (150 grit finish) at 1000X magnification. 1 wt.% NaCl, pH 5, 0.97 bar CO <sub>2</sub> , 25°C, 720 ppm <sub>v</sub> inhibitor, 16 m/s, 4 day test duration, X65, O <sub>2</sub> < 2ppb: A. Specimen 1 before test; B. Specimen 1 after test; C. Specimen 2 before test; D. Specimen 2 after test. ....	152
Figure 6-33: SEM images of protrusion Specimen 3. Before test: 1st row at 50X magnification. After test: 2nd row at 50X magnification; 3rd row at 1000X magnification. Physical locations are defined by using 5 numbered individual regions in Figure 6-2. 1 wt.% NaCl, pH 5, 0.97 bar CO <sub>2</sub> , 25°C, 720 ppm <sub>v</sub> inhibitor, 16 m/s, 4 day test duration, X65, O <sub>2</sub> < 2 ppb. ....	153
Figure 6-34: EDS analysis of flat Specimen 1 (600 grit finish). A: before experiment; B. after experiment. 1 wt.% NaCl, pH 5, 0.97 bar CO <sub>2</sub> , 25°C, 720 ppm <sub>v</sub> inhibitor, 16 m/s, 4 day test duration, X65, O <sub>2</sub> < 2 ppb. ....	154

- Figure 6-35: EDS analysis of protrusion Specimen 3. A: before experiment; B. after experiment, at the top of protrusion, region 3 in Figure 6-2. 1 wt.% NaCl, pH 5, 0.97 bar CO<sub>2</sub>, 25°C, 720 ppm<sub>v</sub> inhibitor, 16 m/s, 4 day test duration, X65, O<sub>2</sub> < 2 ppb..... 155
- Figure 6-36: Pressure drop measurements between port 3 and port 4 in the TCFC with various inhibitor concentrations. 1 wt.% NaCl, pH 5, 0.97 bar CO<sub>2</sub>, 25°C..... 157
- Figure 6-37: Corrosion rates calculated from averaged weight losses of specimens and from LPR corrosion rate curves with B = 65 mV. 1 wt.% NaCl, pH 5, 0.97 bar CO<sub>2</sub>, 25°C, 16 m/s, 4 day test duration, X65. .... 160
- Figure 6-38: Energy diagram of inhibitor adsorption/desorption reactions..... 165
- Figure 6-39: Energy diagram of inhibitor adsorption/desorption reactions with the additional energy due to collapsing cavitation bubbles. .... 168

**List of Abbreviations**

AFM	Atomic force microscopy
AISI	American Iron and Steel Institute
AOPL	Association of Oil Pipe Lines
API	American Petroleum Institute
CAS	Chemical Abstracts Service
CE	Counter electrode
CFD	Computational fluid dynamics
CMC	Critical micelle concentration
CO <sub>2</sub> -EOR	Carbon dioxide enhanced oil recovery
CR	Corrosion rate
DI water	Deionized water
DNS	Direct numerical simulation
EDS	Energy-dispersive X-ray spectroscopy
EIS	Electrochemical impedance spectroscopy
FBG	Fiber Bragg grating
fps	Frames per second

ID	Internal diameter
LPR	Linear polarization resistance
MD	Molecular dynamics simulation
MEMS	Microelectromechanical systems
OCP	Open circuit potential
OD	Outer diameter
PDP	Potentiodynamic polarization
ppb	Part per billion ( $10^9$ ), by weight
ppm <sub>v</sub>	Part per million ( $10^6$ ), by volume
PR	Penetration rate
PVC	Polyvinyl chloride
RCE	Rotating cylinder electrode
RE	Reference electrode
SEM	Scanning electron microscopy
TCFC	Thin channel flow cell
TEM	Transmission electron microscopy
TLC	Top-of-the-line corrosion

TOFA/DETA	Tall oil fatty acid / diethylenetriamine
UDC	Under-deposit corrosion
WE	Working electrode
WSS	Wall shear stress
ZRA	Zero resistance ammeter

## Chapter 1: Introduction

Production and transportation of multiphase fluids through pipelines and tubing is ubiquitous in the oil and gas industry. According to a report jointly published by the American Petroleum Institute (API) and Association of Oil Pipe Lines (AOPL), the total U.S. liquids pipeline mileage was more than 190,000 miles in 2014 [1]. Almost all the pipelines are made of carbon steels for economic reasons. Despite their satisfactory mechanical properties, carbon steels are prone to corrosion problems when exposed to an aqueous environment [2]. Therefore, understanding and mitigating corrosion of pipelines are vital for the economy and society.

Internal CO<sub>2</sub> corrosion, or sweet corrosion, is one of the most prevalent forms of corrosion in upstream oil and gas production and transportation pipelines due to the presence of water and CO<sub>2</sub>. The general mechanisms of CO<sub>2</sub> corrosion have been extensively researched and are well understood [2,3].

Mitigation of CO<sub>2</sub> corrosion can be achieved by the use of organic corrosion inhibitors which form a thin film (order of nm) on the steel surface or by reliance on formation of protective corrosion product layers, such as iron carbonate (thickness of the order of 10 μm). Regardless of the mechanisms related to their adhesion to the metal surface, both form a protective barrier between the corrosive fluids and the underlying steel [2,4–8]. The reduction in corrosion rate depends upon the integrity and protectiveness of these films or layers. Any partial damage or removal of these films or layers may lead to initiation of localized attack and propagation of the localized corrosion through the development of galvanic cells [8,9].

The effects of flow on the integrity of protective inhibitor films or corrosion product layers have been attributed to mass transfer, mechanical forces, and other factors such as the presence of solid particles [10]. Flow enhances the mass transport of corrosive species (e.g.,  $H^+$ ) from bulk solution to the steel surface and accelerates the corrosion of the underlying steel; flow also facilitates the mass transport of the corrosion products, e.g., ferrous ions ( $Fe^{2+}$ ) away from the steel surface and hinders the formation of protective iron carbonate layers [10].

The effect of mechanical forces exerted by single-phase or multiphase flow on these films or layers is not well understood. On one hand, experience from the field and some laboratory experiments indicates that protective films and corrosion product layers can fail at a high flow velocity [11–14]; in those cases high wall shear stress (WSS) has often been suggested as the main culprit [13,15,16]. On the other hand, some detailed laboratory experiments, that isolated pure mechanical effect of flow, found that high WSS in turbulent flow conditions did not affect inhibitor films [17] or corrosion product layers [18,19].

The presence of solid particles in the flow stream can undoubtedly affect corrosion inhibition. At low flow rates settling of particles may lead to under-deposit corrosion (UDC) [20], while at high flow rates the particle-wall impacts may cause damage to inhibitor films and corrosion product layers, often termed erosion-corrosion [21].

To answer the question as to whether flow could mechanically damage the protective inhibitor films and corrosion product layers in the absence of solid particles, the mechanical integrity and adhesion strength of these films/layers to the steel surface were

characterized in controlled laboratory experiments, which were of the order of 1-100 MPa [11,19,22]. Since these stress values are several orders of magnitude larger than the typical WSS values measured or calculated for multiphase pipe flow [9,10,23], it seems to be impossible that multiphase flow is able to mechanically remove a protective inhibitor film or a corrosion product layer. However, it is worth noting that a closer inspection of the literature indicates that there are no direct measurements of WSS in multiphase pipe flow, making the above-mentioned reasoning less convincing.

Accurately measuring WSS in multiphase flow is challenging. Very few studies related to WSS in multiphase flow have been conducted in the past [24–27]. There, the WSS was typically obtained from indirect methods, such as using an electrochemical mass-transfer sensor or a hot-film heat-transfer sensor, which rely on a correlation between the measured property (mass or heat transfer rate) to the WSS [28,29]. These correlations are justified by using the Reynolds analogy, which is strictly valid only in fully developed single-phase flow with no pressure gradients. Therefore, they have a limited range of validity and their extension to complex multiphase flow conditions is not easily justified.

In the present research, a floating element probe was used to directly measure the WSS of multiphase flow. The direct WSS measurements were complemented by high speed camera video recordings of the fluid field. The findings contributed to a better understanding of the complex behaviors of unsteady multiphase flow patterns and provided essential information about the possible magnitudes of mechanical stresses under practical flow conditions in pipelines.

Furthermore, the mechanical effects of flow on CO<sub>2</sub> corrosion inhibition of carbon steel were investigated in a flow loop at very high local flow velocities (up to 28 m/s). Electrochemical measurements, surface analysis and computational fluid dynamics (CFD) were used as diagnostic tools. It was found that cavitation produced by severe flow disturbances can mechanically affect the corrosion inhibitors on the steel surface. The mechanisms related to the cavitation induced localized corrosion and its mitigation were explored.

This dissertation continues in the following order. Chapter 2 provides a critical literature review on the topics of general CO<sub>2</sub> corrosion mechanisms and the effects of flow on CO<sub>2</sub> corrosion and its mitigation. The flow patterns of horizontal gas-liquid two-phase flow in pipes and methods for wall shear measurements are also described. Chapter 3 presents the objectives and hypotheses of this research. Chapter 4 describes the experimental methods and equipment that were utilized. In Chapter 5, the results of direct wall shear stress measurements for single-phase liquid flow and gas-liquid two-phase flow are discussed. In addition, hydrodynamic properties such as flow velocity and slug frequency are determined from the experimental results. Chapter 6 discusses the results of corrosion inhibition tests of carbon steel in the presence of high flow velocities. The related mechanisms of corrosion inhibition failure and its mitigation are also presented. Finally, Chapter 7 summarizes the key findings of this research and outlines future research suggestions.

## Chapter 2: Background and Literature Review

### 2.1 Basics of CO<sub>2</sub> Corrosion

Internal carbon dioxide (CO<sub>2</sub>) corrosion of pipeline steel is commonly seen in the oil and gas industry. This is because carbon steel, particularly low carbon steel (generally less than 0.30 wt.% carbon) [30], is a primary structural material for production tubing and transportation pipelines. Carbon steel has desirable mechanical properties such as high structural strength and low manufacturing cost. However, its corrosion resistance is limited, and often the aqueous CO<sub>2</sub> environment within steel pipes is corrosive.

CO<sub>2</sub> and water are natural constituents found in petroleum reservoirs [31]. During oil and gas production, the CO<sub>2</sub> and water are extracted and transported together with hydrocarbons through steel tubing and pipelines. In addition, due to global climate change, attention has been progressively drawn to carbon capture and sequestration (CCS) in recent decades [32–35], aiming at reducing global carbon emissions. One way to achieve CO<sub>2</sub> sequestration is compressing and depositing CO<sub>2</sub> into underground geological formations, such as depleted oil and gas wells. In the oil and gas industry, this is frequently achieved by means of carbon dioxide enhanced oil recovery (CO<sub>2</sub>-EOR) [36]. By injecting CO<sub>2</sub> and/or water into mature oil fields, the CO<sub>2</sub> is properly stored, and the oil production is significantly increased [37]. In the above-mentioned activities, the CO<sub>2</sub> and water traversing tubing and pipelines create a corrosive environment and pose a potential threat of internal corrosion [38,39]. To ensure safe operations, understanding the CO<sub>2</sub> corrosion mechanisms and providing means of corrosion control are of paramount importance.

### 2.1.1 CO<sub>2</sub> corrosion mechanisms

Mechanisms of CO<sub>2</sub> corrosion of carbon steel have been developed over the past decades and are considered well understood [2,3,40–43]. The process involves several chemical and electrochemical reactions. The key chemical reactions related to CO<sub>2</sub> corrosion are given in Table 2-1. First, gaseous CO<sub>2</sub> dissolves in the aqueous phase through a heterogeneous reaction (as given by Reaction (2-1)). The concentrations of gaseous CO<sub>2</sub> and dissolved aqueous CO<sub>2</sub> are often of the same order of magnitude [2]. The dissolved CO<sub>2</sub> reacts with water and forms carbonic acid (H<sub>2</sub>CO<sub>3</sub>), which is also called the CO<sub>2</sub> hydration reaction as given in Reaction (2-2). H<sub>2</sub>CO<sub>3</sub>, a weak acid, can partially dissociate in water by two steps (Reactions (2-3) and (2-4)), which results in the release of hydrogen ions (H<sup>+</sup>), bicarbonate (HCO<sub>3</sub><sup>-</sup>) and carbonate (CO<sub>3</sub><sup>2-</sup>). In addition, water can dissociate in an aqueous solution, releasing H<sup>+</sup> and hydroxide ion (OH<sup>-</sup>).

Besides chemical reactions in the bulk, aqueous CO<sub>2</sub> corrosion of carbon steel involves several electrochemical reactions occurring at the steel surface. The main anodic/oxidation reaction is the dissolution of iron, which releases ferrous ions (Fe<sup>2+</sup>) into the solution leaving behind the electrons (e<sup>-</sup>). Multiple cathodic/reduction reactions occur in the CO<sub>2</sub> corrosion process. The released electrons from iron are taken up by the readily available chemical species at the surface through reduction reactions, which are also called hydrogen evolution reactions as dissolved hydrogen gas is the common reaction product. The main electrochemical reactions of CO<sub>2</sub> corrosion are given in Table 2-2.

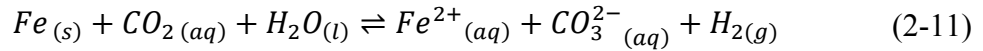
Table 2-1: Key chemical reactions of aqueous CO<sub>2</sub> corrosion and the corresponding chemical equilibrium expressions

Reaction	Chemical equilibrium expression
$CO_{2(g)} \xrightleftharpoons{K_{sol}} CO_{2(aq)}$	$K_{sol} = \frac{c_{CO_2}}{p_{CO_2}}$ (2-1)
$CO_{2(aq)} + H_2O_{(l)} \xrightleftharpoons{K_{hy}} H_2CO_{3(aq)}$	$K_{hy} = \frac{c_{H_2CO_3}}{c_{CO_2}}$ (2-2)
$H_2CO_{3(aq)} \xrightleftharpoons{K_{ca}} H^+_{(aq)} + HCO_3^-_{(aq)}$	$K_{ca} = \frac{c_{H^+} + c_{HCO_3^-}}{c_{H_2CO_3}}$ (2-3)
$HCO_3^-_{(aq)} \xrightleftharpoons{K_{bi}} H^+_{(aq)} + CO_3^{2-}_{(aq)}$	$K_{bi} = \frac{c_{H^+} + c_{CO_3^{2-}}}{c_{HCO_3^-}}$ (2-4)
$H_2O_{(l)} \xrightleftharpoons{K_{wa}} H^+_{(aq)} + OH^-_{(aq)}$	$K_{wa} = c_{H^+} + c_{OH^-}$ (2-5)

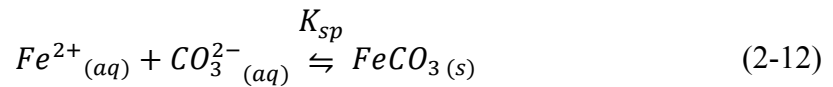
Table 2-2: Key electrochemical reactions of aqueous CO<sub>2</sub> corrosion

Anodic	$Fe_{(s)} \rightarrow Fe^{2+}_{(aq)} + 2e^-$ (2-6)
Cathodic	$2H^+_{(aq)} + 2e^- \rightarrow H_{2(g)}$ (2-7)
Cathodic	$2H_2CO_{3(aq)} + 2e^- \rightarrow H_{2(g)} + 2HCO_3^-_{(aq)}$ (2-8)
Cathodic	$2HCO_3^-_{(aq)} + 2e^- \rightarrow H_{2(g)} + 2CO_3^{2-}_{(aq)}$ (2-9)
Cathodic	$2H_2O_{(l)} + 2e^- \rightarrow H_{2(g)} + 2OH^-_{(aq)}$ (2-10)

From Table 2-1 and Table 2-2, the overall reaction of CO<sub>2</sub> corrosion of carbon steel may be summarized by the following reaction:



It can be seen that ferrous ion and carbonate ion are products of CO<sub>2</sub> corrosion. If the concentrations of these two species in the solution are sufficiently high, precipitation of solid iron carbonate (FeCO<sub>3</sub>) will occur, as shown by:



Due to the reversible nature of this reaction, the solid iron carbonate can also dissolve in the solution when the ferrous ion and carbonate ion concentrations are below the saturation level.

### *2.1.2 Mitigation of CO<sub>2</sub> corrosion*

In the previous section, the main reactions in aqueous CO<sub>2</sub> corrosion of carbon steel are concisely presented. In this section, the common approaches to mitigate CO<sub>2</sub> corrosion are introduced.

#### *2.1.2.1 Formation of a protective FeCO<sub>3</sub> corrosion product layer*

As described earlier, a FeCO<sub>3</sub> layer can form in CO<sub>2</sub> corrosion as long as the concentrations of ferrous and carbonate ions are above saturation. The saturation criterion of FeCO<sub>3</sub> layer formation is quantitatively defined as supersaturation,  $S_{(FeCO_3)}$ , given by:

$$S_{(FeCO_3)} = \frac{c_{Fe^{2+}}c_{CO_3^{2-}}}{K_{sp}} \quad (2-13)$$

where  $c_{Fe^{2+}}$  and  $c_{CO_3^{2-}}$  are the concentrations of ferrous ion and carbonate ion, respectively, and  $K_{sp}$  is the solubility product constant of  $FeCO_3$ . This equation represents the balanced reactions of  $FeCO_3$  precipitation and dissolution. When  $S_{(FeCO_3)}$  is greater than 1, the precipitation reaction prevails and a  $FeCO_3$  layer may form on the steel surface. Conversely, no  $FeCO_3$  layer is expected when the  $S_{(FeCO_3)}$  is less than 1, as the dissolution process is dominant. The  $S_{(FeCO_3)}$  is greatly dependent on the pH and  $c_{Fe^{2+}}$ . When substituting the equilibrium expressions presented in Table 2-1 into Reaction (2-13), the saturation value can be written as:

$$S_{(FeCO_3)} = \frac{c_{Fe^{2+}}K_{bi}K_{ca}K_{hy}K_{sol}p_{CO_2}}{K_{sp}c_{H^+}} \quad (2-14)$$

where  $p_{CO_2}$  is the partial pressure of  $CO_2$  in the gas phase. The reaction constants are functions of temperature, pressure and ionic strength [2].

The characteristics of the  $FeCO_3$  layer have been studied by various researchers [5,7,44]. It is generally accepted that a complete coverage of  $FeCO_3$  on a steel surface leads to protection because this layer presents a mass transfer barrier for corrosive species and slows down the corrosion process. To illustrate this by an example, Figure 2-1 shows the topography of a steel surface entirely covered by a dense  $FeCO_3$  layer consisting of prism-shaped  $FeCO_3$  crystals. Figure 2-2 shows the structure of a  $FeCO_3$  layer covered steel surface from the cross-sectional side view. A complete coverage of  $FeCO_3$  is clearly seen on the steel substrate.

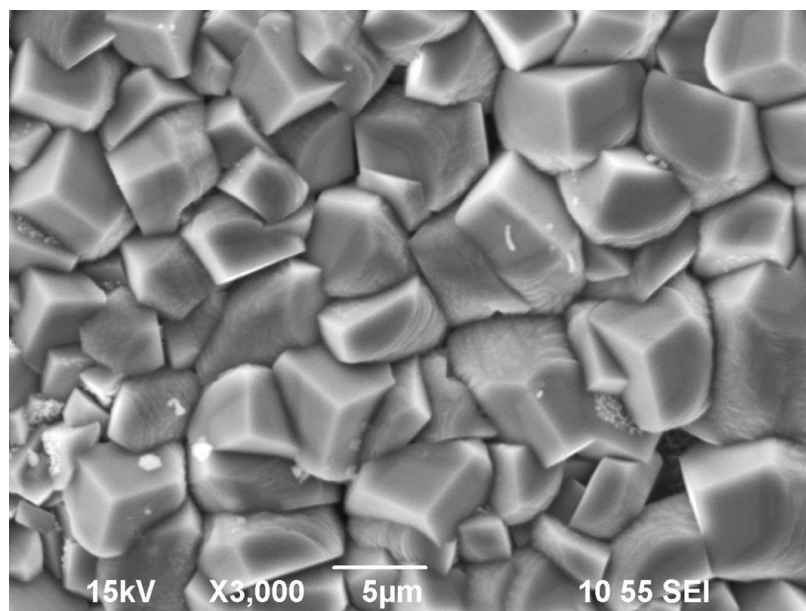


Figure 2-1: A top view SEM image of a steel surface covered by a FeCO<sub>3</sub> layer. 80°C, 0.53 bar CO<sub>2</sub>, pH 7.8, stagnant.

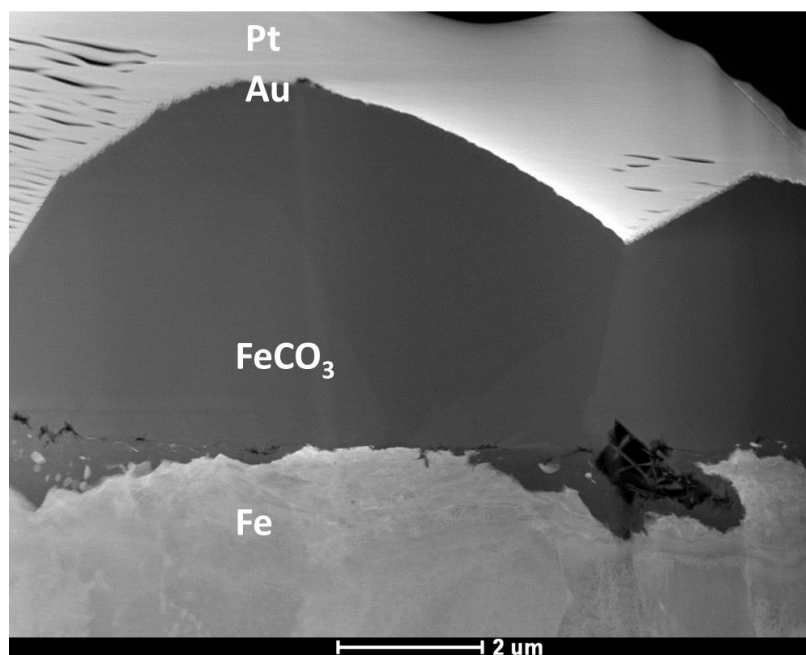


Figure 2-2: A cross-sectional side view TEM image of a FeCO<sub>3</sub> covered steel surface. 80°C, 0.53 bar CO<sub>2</sub>, pH 7.1, stagnant. The specimen was coated with Au and Pt during specimen preparation.

Multiple researchers [6,8,45] found that the corrosion rate was significantly retarded when the steel surface was fully covered by a  $\text{FeCO}_3$  layer; this decrease of corrosion rate was accompanied by a dramatic increase of open circuit potential. This behavior was termed pseudo-passivation [8] as the  $\text{FeCO}_3$  layer offered a corrosion protection similar to metal passivation in the sense that the corrosion potential becomes more positive as the corrosion rate is reduced. Pseudo-passivation was usually observed at a relatively high pH, which favored the precipitation of  $\text{FeCO}_3$ . The dependence of  $\text{FeCO}_3$  precipitation on pH is revealed by Equation (2-14). In laboratory experiments Han et al. [8] observed the pseudo-passivation at a pH of 8.0 and identified a trace amount of  $\text{Fe}_3\text{O}_4$  within the  $\text{FeCO}_3$  layer. Li et al. [6] found that pseudo-passivation occurred with a pH higher than 6.0 at 80°C and 0.53 bar  $\text{CO}_2$ .

Generally,  $\text{FeCO}_3$  forms a protective corrosion product layer against internal corrosion of pipelines when the environment has a high pH value. For example, de Moraes et al. found that a very protective  $\text{FeCO}_3$  layer formed in a flow loop at a pH higher than 5.5 at 93°C [46]. Therefore, formation of protective  $\text{FeCO}_3$  layers under specific conditions is deemed an effective means to mitigate  $\text{CO}_2$  corrosion.

#### *2.1.2.2 $\text{CO}_2$ Corrosion inhibitors*

It was stated above that  $\text{FeCO}_3$  corrosion product layers can provide corrosion protection for systems with a relatively high pH value. For systems with more acidic conditions, other corrosion mitigation approaches are required since no protective  $\text{FeCO}_3$  corrosion product layer would form on the steel surface. In the oil and gas industry,

applications of corrosion inhibitors are often deemed a cost-effective alternative to mitigate internal corrosion [39].

In general, corrosion inhibitors are chemical compounds added to aqueous environments in small concentrations which interact with the metal surface and reduce the oxidation rate of the metal [47]. The chemical corrosion inhibition process comprises two steps, mass transport of inhibitors from the bulk to the steel surface and interactions between the inhibitors and the steel surface [47]. Corrosion inhibitors have been generally classified as three types [48]: Type A inhibitors adsorb on the steel surface to form a protective inhibitor film that prevents corrosive species reaching the steel surface; Type B inhibitors change the solution chemistry and reduce the corrosivity of the environment, e.g., oxygen scavengers; and Type C inhibitors possess the properties of both Type A and Type B inhibitors.

An extensive amount of corrosion inhibitors fall into Type A, which are usually organic compounds [4,47–49]. These organic compounds are typically surface-active agents, or surfactants, which are amphiphilic. This is because a surfactant molecule contains both hydrophobic (non-polar tail) and hydrophilic (polar head) groups. The hydrophobic tails are long hydrocarbon chains (usually C6 to C22 [50]), while the hydrophilic heads are either non-ionic or ionic functional groups. Surfactants with ionic hydrophilic heads can be further classified as anionic, cationic and zwitterionic types [51], depending on the electrical charge on the heads. Anionic type surfactants have negative charge on the head groups; cationic type surfactants have head groups carrying

positive charge. For zwitterionic type surfactants, the heads contain both positively and negatively charged groups [52].

Due to their amphiphilic nature, surfactant inhibitors tend to adsorb orderly at interfaces [51]. Therefore, surfactants provide corrosion protection by forming an adsorbed film at the metal-solution interface. Adsorption of surfactants depends on a variety of factors, such as the nature of the substrate (adsorbent), the chemical and structural properties of the surfactant molecule (adsorbate), and the environment (e.g., temperature, pH and electrolyte) [51]. Generally, adsorption of surfactants is attributed to intermolecular interactions, which include electrostatic interactions, hydrophobic interactions, covalent bonding and hydrogen bonding [53].

The adsorption of ionic surfactants is mainly driven by electrostatic and hydrophobic interactions [54]. The mechanisms of ionic surfactant adsorption on oppositely charged surfaces have been extensively studied by using adsorption isotherms and are reasonably well understood [53–55]. The adsorption isotherm of ionic surfactants is typically classified by four regions [53,54], as shown in Figure 2-3. In region I, the surfactant concentration is low and the dominating driving force for adsorption is the electrostatic interaction between the hydrophilic head group of individual surfactant molecules and the charged substrate surface. The adsorbed surfactants on the surface are present in the form of single molecules unassociated with each other [53]. In region II, besides the electrostatic interactions, the hydrophobic interactions between the hydrophobic tail groups of the adsorbed molecules become significant, which lead to the formation of a monolayer by aggregation. Due to this additional driving force, the adsorption in this

region is drastically increased. At the end of this region, the surface is electrically neutralized by the oppositely charged surfactant ions [53,54]. In region III, as electrostatic interactions in direct association with the surface are no longer possible, increase of adsorption with a reduced rate occurs due to the hydrophobic interactions between the non-polar tails of the adsorbed surfactants and the free surfactants in the bulk, which results in the structural growth of the aggregates; in the figure this is shown as bilayer formation. In region IV, when further adding surfactants to the system above a threshold concentration, the steel surface is saturated with aggregates and reaches maximum coverage, and the excess surfactants form micelles in the bulk solution. Due to the hydrophobicity, the micelles have structures in which the hydrophobic groups of the molecules stick together and the hydrophilic groups face toward the aqueous environment. This threshold concentration is referred to as the critical micelle concentration (CMC). It is defined as the minimum concentration of surfactants at which micelles can be detected and all additional surfactants form micelles [56]. The CMC features abrupt changes in the physical properties of the solution such as surface or interfacial tension, electrical conductivity, and light scattering [51]; these characteristics are practically used for the determination of the CMC value. For example, Figure 2-4 shows a surface tension-concentration curve, where a sharp change of surface tension around CMC can be seen.

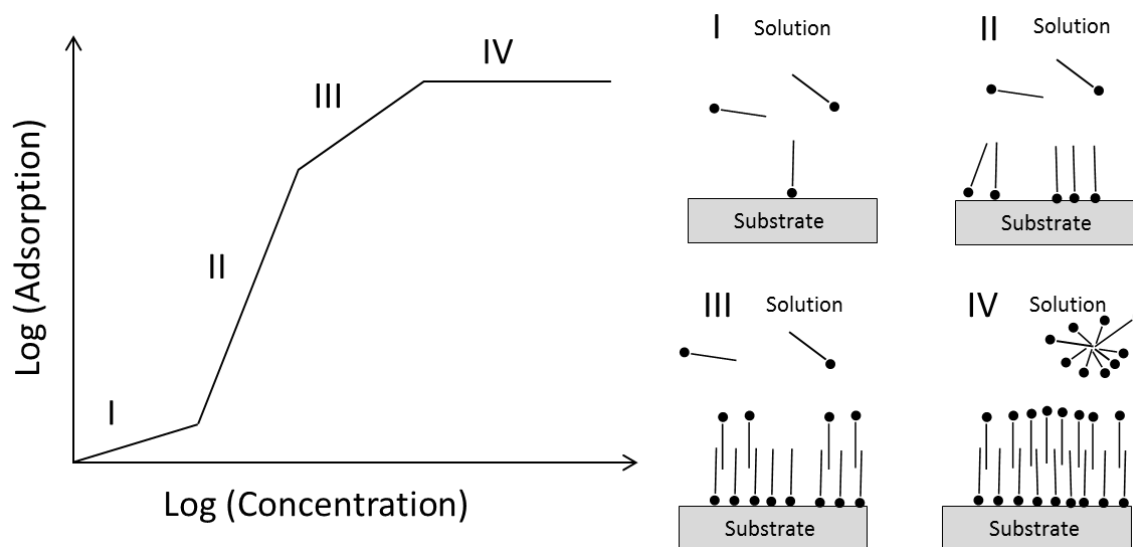


Figure 2-3: Adsorption mechanisms of ionic surfactants on the charged substrate surface (adapted from [54]).

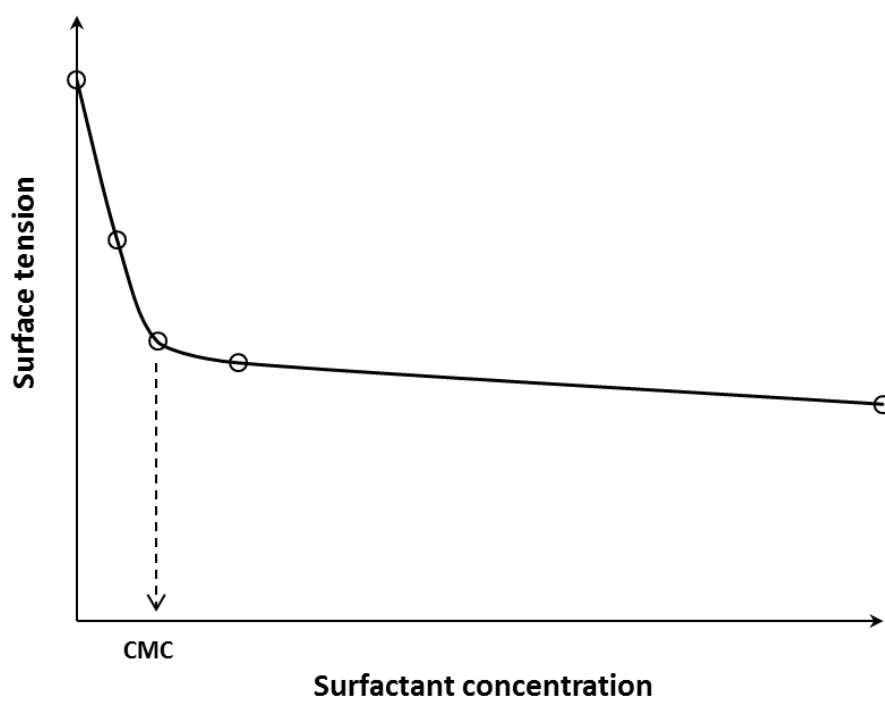


Figure 2-4: Curve of surface tension – surfactant concentration.

In the oil and gas industry, particularly in upstream operations, fatty imidazolines and various amine compounds are widely used as surfactant-type corrosion inhibitors [57]. Imidazolines and their derivatives are often utilized in CO<sub>2</sub> corrosion inhibition programs due to their high efficiency in an acidic environment [58]. Extensive studies of the related corrosion inhibition mechanisms have been conducted [4,58–61]. In the present research, a known composition generic imidazoline-based surfactant (hereafter named “K1”) provided by industrial operators was used as a model inhibitor to study the CO<sub>2</sub> corrosion inhibition of carbon steel. The chemical formulation of this inhibitor is given in Table 2-3. The inhibitor package was a chemical mixture containing 24% active component of tall oil fatty acid diethylenetriamine (TOFA/DETA) imidazolinium salt. The molecular structure of this inhibitor is depicted in Figure 2-5. Because the head group of the molecule (the five-membered nitrogen ring) is positively charged, it is a cationic type surfactant inhibitor. The adsorption mechanism for this type of inhibitor was elucidated earlier in this section. In addition, the pendant side chain may provide a secondary driving force for the inhibitor adsorption due to the additional electrostatic interaction between the lone pair in the amine group and the steel surface [58]. With a high enough concentration, these inhibitor molecules form a protective film and effectively reduce the corrosion rate of the underlying steel substrates in an aqueous CO<sub>2</sub> environment.

Table 2-3: Chemical formulation of the model inhibitor K1 [wt.%]

Water	Acetic acid	ARMOHIB CI-219	2-Butoxyethanol (CAS no. 111-76-2)
53	10	24	13

Note: ARMOHIB CI-219 consists of 95-100% tall oil, diethylenetriamine imidazoline (CAS no. 68442-97-7) and 1-5 % diethylenetriamine (CAS no. 111-40-0).

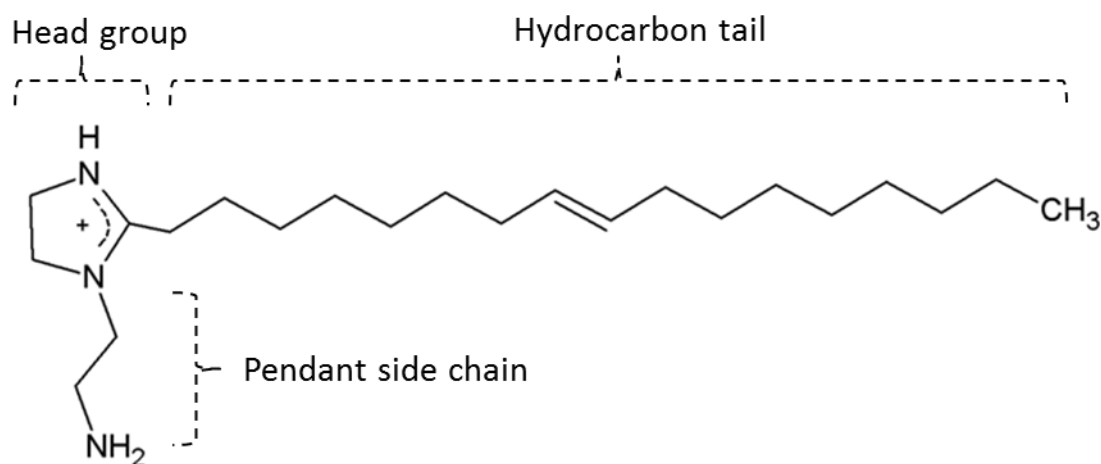


Figure 2-5: Molecular structure of TOFA/DETA imidazolinium ion.

## 2.2 Flow Patterns in Gas-Liquid Two-Phase Flow

Transporting gas and liquid concurrently through pipelines is often encountered in the oil and gas industry, which makes the internal CO<sub>2</sub> corrosion problem more complex. Gas-liquid two-phase flow features a variety of flow patterns. A flow pattern is the geometrical distribution of gas and liquid phases in the pipe [62], which depends on the properties of the two phases, the respective flow velocities of the two phases and the pipe configuration. Each flow pattern presents unique flow characteristics such as the phase distribution and the velocity profile, which have a profound effect on internal corrosion

and its inhibition. For horizontal flow, the flow patterns can be classified as stratified flow, slug flow, dispersed-bubble flow, and annular flow, as depicted in Figure 2-6.

Stratified flow occurs with relatively low gas and liquid velocities. The liquid phase flows at the bottom of the pipe while the gas phase flows at the top due to their difference in density. A small amount of gas bubbles may be entrained in the liquid phase. Stratified flow can be further categorized into stratified-smooth and stratified-wavy flow, depending on the gas phase velocity. Stratified-smooth flow occurs at lower gas velocities, featuring a smooth interface between the gas and liquid phases. Stratified-wavy flow is more likely to occur at higher gas velocities, characterized by the waves formed at the gas-liquid interface.

Slug flow has a relatively higher liquid velocity as compared to stratified flow. Horizontal slug flow features a repetitive passage of slug units at a given location. A slug unit consists of a liquid slug body followed by a stratified zone. In the liquid slug body, the liquid phase bridges the entire pipe cross-section. A highly turbulent mixing occurs in this region with a significant amount of entrained gas bubbles. In the stratified zone, a relatively slow liquid film moves at the bottom with faster moving gas above it.

Dispersed-bubble flow is expected when the liquid velocity is very high. In this pattern, the liquid phase is a continuous phase, while the gas phase is present as a discrete phase in the form of gas bubbles in the liquid.

Annular flow occurs at very high gas velocities. A thin wavy liquid film travels around the inner pipe periphery while the continuous gas phase with high velocity flows in the core. Usually, a thicker liquid film can be found at the bottom of the pipe compared

to that at the top [62]. In addition, part of the liquid will be entrained and travel as discrete droplets in the gas core. Due to the presence of entrained liquid droplets, this flow pattern is also called annular-dispersed flow.

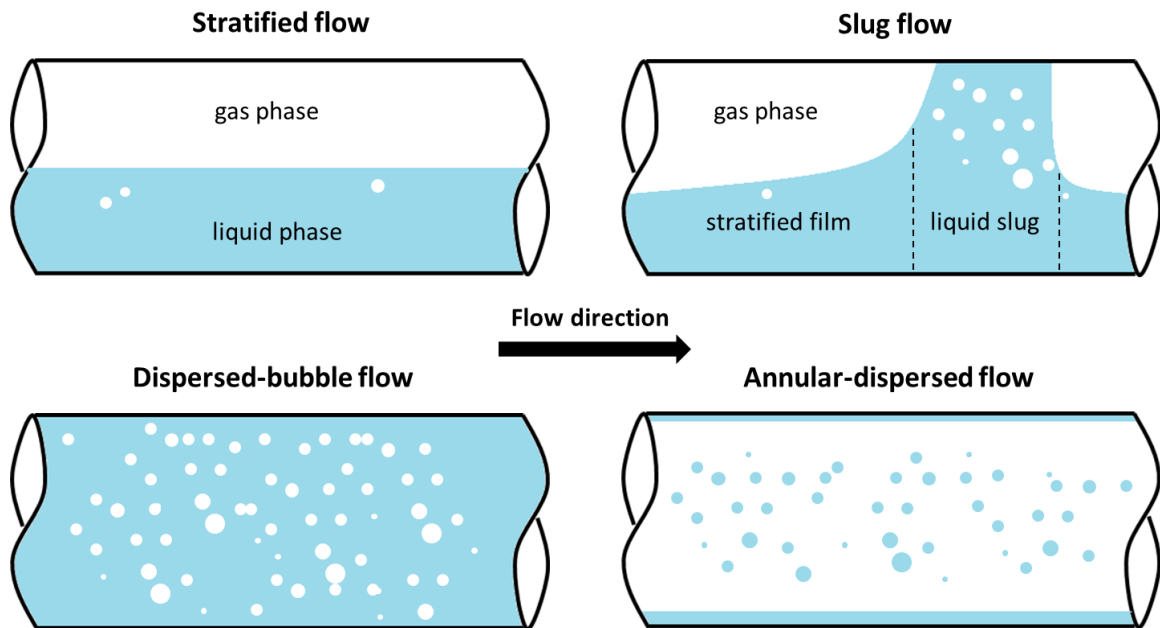


Figure 2-6: Schematics of flow patterns in horizontal gas-liquid two-phase flow (adapted from [62]).

As described, the flow patterns are strongly dependent on the flow velocities of the gas and liquid phases. Transitions between flow patterns can be represented by a flow pattern map constructed with respect to the gas and liquid flow velocities, as illustrated in Figure 2-7. For two-phase flow, the superficial velocities are usually used, which are defined as the volumetric flow rate of the phase divided by the cross-sectional area of the full pipe.

So far, the main flow patterns of gas-liquid two-phase flow have been described. Compared to single-phase flow, two-phase flow usually features inhomogeneous phase distributions and is highly turbulent. Therefore, the effect of two-phase flow on CO<sub>2</sub> corrosion is deemed more complex.

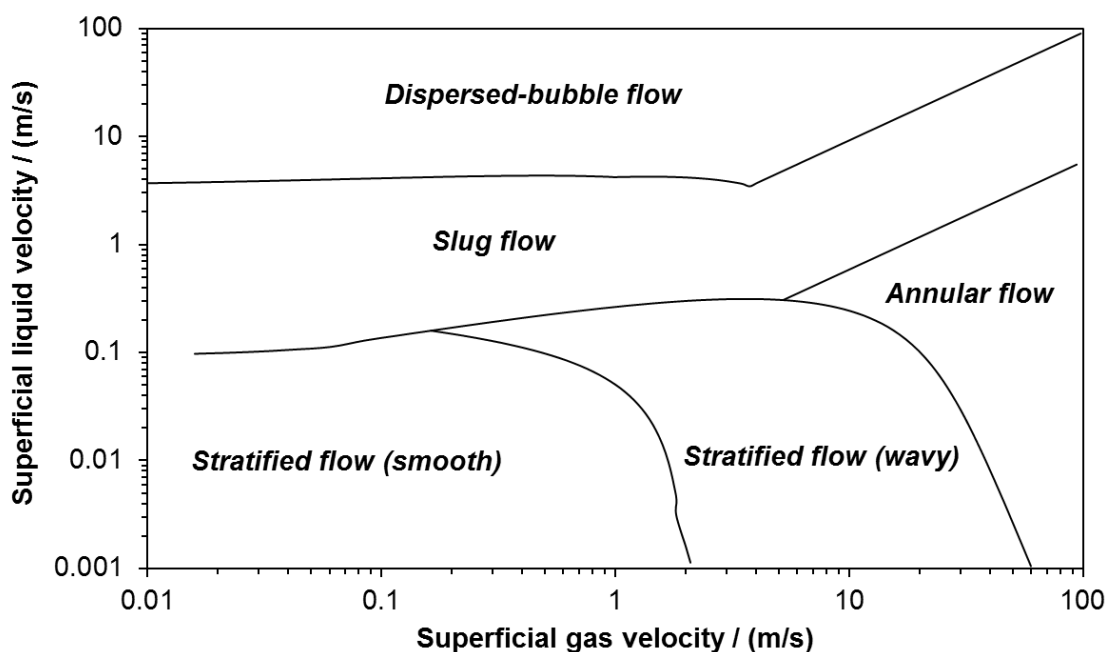


Figure 2-7: A flow pattern map for horizontal gas-liquid two-phase flow. H<sub>2</sub>O / CO<sub>2</sub>, 25°C, 1 bar, 4 inch ID pipe (generated by an in-house gas-liquid flow model [63]).

### 2.3 Effects of Flow on Mitigation of CO<sub>2</sub> Corrosion

It was mentioned earlier that a complete coverage of protective FeCO<sub>3</sub> layers or corrosion inhibitor films on the steel surface can significantly reduce the corrosion rate. However, any partial damage or removal of these films or layers may lead to severe localized corrosion [8,9]. In this section, several effects of flow on the integrity of protective inhibitor films and corrosion product layers are discussed.

### 2.3.1 Effect of mass transfer

Flow enhances the mass transport of corrosive species from bulk solution to the steel surface and accelerates the corrosion of the underlying steel [2]. In CO<sub>2</sub> corrosion, because all the electrochemical reactions simultaneously occur at the metal-solution interface, the mass transport of reactants (e.g., H<sup>+</sup>) from bulk to the metal surface is usually involved. If the mass transport cannot provide enough reactants to the steel surface where the fast electrochemical reactions occur, the corrosion rate/current will be affected by the mass transport process, referred to as mass transfer limiting current [64]. The mass transfer effect of flow on electrochemical reactions occurring at the metal surface can be best illustrated by using the oxidation-reduction reactions of the ferricyanide-ferrocyanide couple [65], which are written as:



For example, Figure 2-8 shows the measured mass transfer limiting currents for the anodic and cathodic reactions of the ferri/ferrocyanide couple on a nickel rotating cylinder electrode (RCE) in an alkaline solution (See Appendix 1 for more details). It clearly demonstrates that the mass transfer limiting currents increase with an increasing flow velocity. The flow dependent electrochemical limiting current is often measured to calculate the mass transfer coefficient ( $k_m$ ) with the following formula [65]:

$$k_m = \frac{i_{lim}}{n_e F A C_b} \quad (2-16)$$

where  $i_{lim}$  is the mass transfer limiting current;  $n_e$  is the number of electrons in the reaction;  $F$  is the Faraday's constant;  $A$  is the surface area of the electrode; and  $C_b$  is the bulk concentration of the reactant.

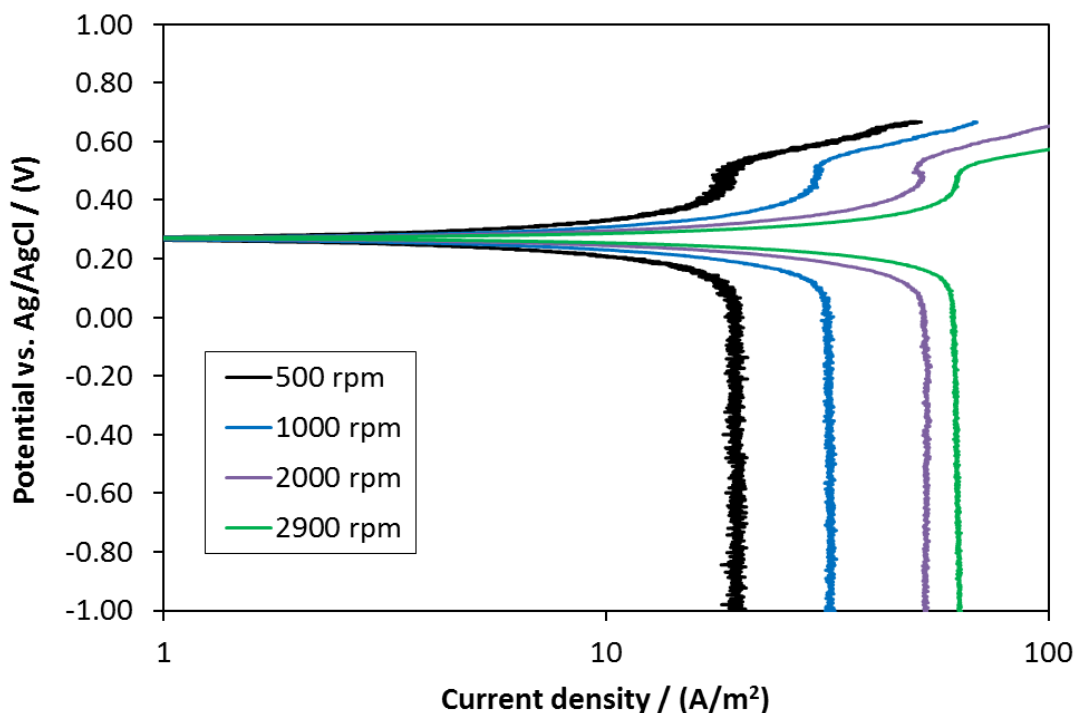


Figure 2-8: Potentiodynamic polarization curves measuring the mass transfer limiting currents of the ferri/ferrocyanide. Nickel RCE electrode (a diameter of 12 mm and length of 14 mm), 25°C, 2 M NaOH, 0.01 M  $\text{K}_4[\text{Fe}(\text{CN})_6] / \text{K}_3[\text{Fe}(\text{CN})_6]$ , 1 bar  $\text{N}_2$ .

Flow may not only enhance the mass transport of corrosive species toward the steel surface, but also interfere with the  $\text{FeCO}_3$  layer formation by facilitating the mass transport of the corrosion-generated ferrous ions ( $\text{Fe}^{2+}$ ) away from the steel surface. In acidic conditions such as  $\text{CO}_2$  corrosion, a decrease of  $\text{Fe}^{2+}$  concentration and increase of  $\text{H}^+$  concentration at the surface by enhanced mass transport result in a lower saturation value for  $\text{FeCO}_3$  according to Equation (2-14), which hinders the formation of protective  $\text{FeCO}_3$  layers.

### 2.3.2 *Effect of mechanical forces*

The effect of mechanical forces exerted by flow on the integrity of inhibitor films or  $\text{FeCO}_3$  layers is not well understood. Prevalent thinking is that high magnitude stresses produced by turbulent flow (e.g., WSS) mechanically damage the protective films or layers, resulting in partial removal of these films or layers from the steel surface and leading to accelerated corrosion rates or even severe localized corrosion [9,13]. This postulate seems to be supported by some field experience and laboratory observations. For example, Pots et al. executed a series of field tests and found that the corrosion inhibitor failed above certain flow velocities [14]. They assumed that the high WSS was the cause for the corrosion inhibitor failure. In another laboratory study Ruzic et al. observed the mechanical removal of  $\text{FeCO}_3$  layers on a rotating cylinder electrode at high rotating speeds. It was suspected that severe local WSS fluctuations exceeding the adhesive strength of the layers resulted in a fatigue-type damage [12]. Upon careful examination of the results, it is found that occurrence of high WSS is often inevitably coupled with other possible influencing factors in the high flow velocity environments, such as enhanced mass transfer rate and changed local water chemistry, formation of bubbles and droplets in multiphase flow, etc. Therefore, one could not always conclude that it is the WSS that causes to the failures of these protective films or layers, as was often done in the past, but rather only that WSS correlates with failures of these protective films or layers. Correlation does not always mean causation.

In other detailed laboratory experiments focused on the pure mechanical effect of flow, no failure of these films or layers due to WSS was found. Gulbrandsen and Grana

[17] used a jet impingement setup and found that the CO<sub>2</sub> corrosion inhibitor performance was independent of flow velocity up to 20 m/s with a calculated WSS up to 1400 Pa. They also observed that ingress of O<sub>2</sub> in the flow system greatly accelerated the corrosion rate due to the enhanced mass transfer rate of O<sub>2</sub> by the highly turbulent flow. In a very different flow geometry in a thin channel, Farelas found that the flow with a WSS value up to 350 Pa (flow velocity up to 13.8 m/s) was unable to mechanically remove the formed FeCO<sub>3</sub> layer on the steel surface [18].

With the inconsistency in the existing literature, the question as to whether flow could mechanically damage the protective inhibitor films and corrosion product layers remains unanswered. Obtaining the answer requires accurate measurements of the adhesion strength of these films / layers to the steel surface and the magnitudes of WSS exerted by flow. The adhesion strength of these films and layers has been previously characterized in controlled laboratory experiments. For example, the adhesion strength of the FeCO<sub>3</sub> layer to a steel substrate was measured by tensile testing [11,19]. In these experiments, an external stud was glued to a FeCO<sub>3</sub> layer pre-formed on the steel surface by using a strong adhesive and then separated. The required separation force was measured, and the adhesion strength of the FeCO<sub>3</sub> layers to the steel surface was calculated to be of the order of 1 - 10 MPa. In another study, Xiong et al. [22] used atomic force microscopy (AFM) to mechanically remove an inhibitor film from a steel surface. The adsorbed inhibitor film was “scratched” away by the lateral movements of the AFM tip that was in contact with the steel surface. The required lateral forces to remove the inhibitor molecules from the steel surface were calculated to be of the order of 50 - 100 MPa. The

experimental findings suggest that the adhesion strength of these protective films or layers is of the order of MPa. On the other hand, typical WSS values measured or calculated in multiphase pipe flow are of the order of 1 Pa–1 kPa [9,10,23]. Some researchers focused on the local fluctuations of turbulence by analyzing the electrochemical current noise data, they claimed that flow could generate a MPa magnitude turbulent energy density [9,66]. However, their conclusions were based only on indirect correlations and mathematic manipulations of the mass transfer electrochemical current noise data. No direct experimental evidence or the Direct Numerical Simulation (DNS)<sup>1</sup> data obtained in single phase liquid flow, indicates that flow can generate a WSS of such magnitude.

Since the adhesion strength values of the inhibitor films or corrosion product layers are several orders of magnitude larger than the generally believed WSS values in practical pipe flow systems, doubts exist as to whether multiphase flow is able to mechanically remove a protective film or corrosion product layer. However, a closer inspection of literature sources indicates that there are no direct measurements for WSS in multiphase pipe flow. Therefore, accurate measurements of the WSS for multiphase flow become imperative to answer the above-mentioned questions. The current available techniques for WSS measurements are reviewed in the following section.

---

<sup>1</sup> DNS is a numerical technique where the Navier Stokes equations are solved fully in time and space resulting in an unrestricted access to all the key aspects of the flow field.

### *2.3.3 Other miscellaneous effects found in multiphase flow*

Other miscellaneous effects found in multiphase flow complicate the problem of CO<sub>2</sub> corrosion mitigation, such as condensation in so called Top-of-the-line corrosion (TLC) and the presence of solids in the flow [10].

TLC corrosion occurs in “wet” gas transportation pipelines with a stratified flow pattern due to the water condensation at the top of the internal pipe wall, where the saturated vapor inside the pipe is cooled by the surrounding environment being at a much lower temperature [10]. The condensed water at the steel surface contains dissolved gases such as CO<sub>2</sub>, which locally forms a corrosive environment and leads to severe localized corrosion problems [67]. Due to the stratified flow pattern, mitigation of TLC by injection of corrosion inhibitors is challenging because the inhibitors in the liquid phase flowing at the bottom of the pipe may not reach the top of the pipe [10].

The presence of solids in pipe flow is often problematic. At low flow rates, solid particles precipitate at the bottom of the pipe and drastically change the local flow and water chemistry, leading to so called under-deposit corrosion. The solids may also influence the corrosion inhibition process. It was found that sand particles can adversely affect the inhibitor adsorption in the crevices between the settled particles and the underlying steel surface, resulting in severe localized corrosion due to the formation of galvanic cells [20]. At high flow rates, entrained solid particles in the flow stream frequently impinge on the pipe wall. The particle-wall impacts may cause damage to the protective corrosion product layers or prevent the formation of such layers [21], which is often termed erosion-corrosion.

## 2.4 Wall Shear Stress Measurements

Answering the question as to whether flow is able to mechanically remove protective corrosion product layers and inhibitor films relies on accurate measurements of WSS. Numerous methods for WSS determination have been developed in the past decades, which may be grouped as shown in Figure 2-9. Several prevalent methods of WSS measurements in flow studies are outlined below.

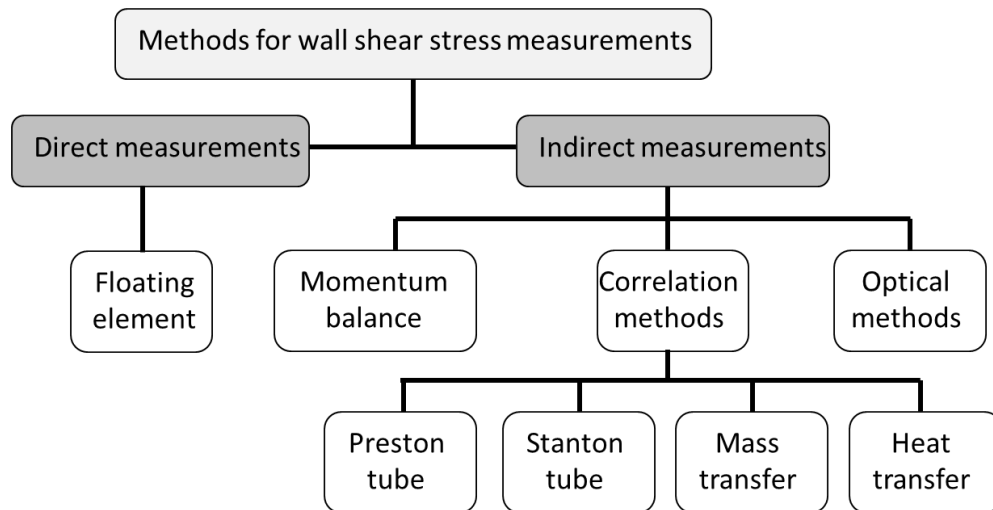


Figure 2-9: Classification of methods for wall shear stress measurements (adapted from [68–70]).

### 2.4.1 Direct measurements

Direct measurements of WSS are achieved by using a mechanical device with an element flush mounted on the wall that allows for lateral movements, often termed a floating element (as shown in Figure 2-10). The force exerted by the flow shear on the floating element results in displacement of the floating element, which is a function of the mechanical properties of the device. The displacement is directly correlated to the exerted

mechanical force on the floating element, by which the WSS is determined. The main advantage of this method is that the WSS is directly measured and no other assumptions are necessary. The historical prototypes of this device did have some shortcomings. Winter et al. [68] listed the experimental deficiencies as the effects of misalignment of the element, temperature changes, the necessary gaps around the floating element, heat transfer, etc.

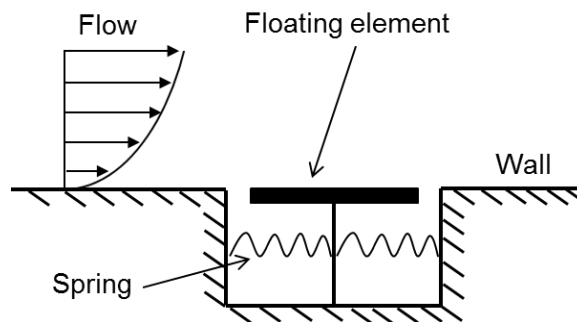


Figure 2-10: Schematic of classical floating element WSS sensor (adapted from [69]).

In order to address these issues, several modifications of this device have been recently implemented. The microelectromechanical systems (MEMS) based floating element sensors have been progressively developed for WSS measurement [28,69,71]. Thanks to the development of micromachining, this miniature floating element, usually with dimensions of the order of 1-1000  $\mu\text{m}$  [69], successfully solves problems related to its conventional macroscale counterparts such as the influence of gaps and misalignment of the element [28].

In principle, direct measurements rely on accurately measuring the lateral displacement of the floating element. The displacement can be measured by using

transduction techniques such as piezoresistive or capacitive detection [69]. Piezoresistive-type and capacitive-type floating elements change their electrical resistivity and capacitance, respectively, when they are under mechanical strain. These techniques have good sensitivity for mechanical stress. However, a major drawback is that they are also very sensitive to temperature and electromagnetic interference. In addition, it is not easy to isolate WSS from normal pressure forces exerted on the floating element. The optical technique is also used to accurately detect the lateral displacement of the floating element [69]. In one design of an optical-based WSS sensor [72], two photodiodes are mounted underneath the floating element, measuring the light from a laser source above the floating element. The displacement of the floating element due to WSS results in partial blockage of the light to the photodiodes. The change of the current signals transmitted by the photodiodes is directly related to the WSS exerted on the floating element. This technique requires an optically clean working environment, which is not easy to satisfy in liquid turbulent pipe flow.

The MEMS-based floating element significantly improves both the temporal and spatial resolution of the measurements due to its small physical dimensions and reduced inertia [28]. This type of device is often used in turbulent gas flow, especially in the aerospace industry, where accurate measurements of small WSS fluctuations are demanded [69]. This modified device has also been used in liquid environments, although infrequently. Shajii et al. [73] fabricated a floating element sensor with a surface dimension of  $120\ \mu\text{m} \times 140\ \mu\text{m}$  and tested its performance in liquid flow generated by a viscometer. It was claimed to have a measurement range from 1–100 kPa. However, due

to the low sensitivity, it was not readily applicable to liquid turbulent flow [69]. From this brief review, it appears that most of the earlier floating element WSS sensors are not robust enough for working in turbulent single-phase and multiphase flow that is similar to field conditions seen in the oil and gas industry.

Recently, another noticeable modification to the floating element sensor has been made by Lenterra, Inc. [74]. In their WSS probe design, the displacement of the floating element is measured using optical strain gauges. The floating element is connected to a mechanical cantilever. Two optical fiber strain gauges, with fiber Bragg grating (FBG), are attached to the cantilever. The top face of the floating element flush mounted on the internal pipe wall is laterally displaced when there is fluid shearing over its surface. Any movement of the floating element causes bending (mechanical deformation) of the cantilever, which changes the optical reflection spectra obtained from the attached strain gauges. The optical spectra are then processed followed by straightforward mechanical calculations that indicate the WSS value. Using two optical fiber strain gauges solves the problem of influence of temperature and has a measurement range (0.1 Pa to 1 kPa) close to the WSS values expected in practical liquid flow conditions. Due to the usage of durable fabrication materials such as stainless steel and glass fibers in this sensor, it is robust for WSS measurements in a liquid turbulent flow environment. Therefore, this floating element sensor was used in the present experimental study; the details will be introduced later.

### 2.4.2 Indirect measurements

Sensors using indirect methods are often employed for WSS measurements, especially in liquid turbulent flow, because they are generally easier to manufacture and more robust than floating element sensors [28]. All indirect methods rely on a theoretical or empirical correlation between the measured properties to the WSS through a set of assumptions. Several indirect methods, with their advantages and disadvantages, are given below.

#### 2.4.2.1 Pressure-difference based methods

Pressure-difference based methods, such as the Preston tube and the Stanton tube, are relatively simple to use for estimating the average shear stress. There is generally no direct correlation between WSS and pressure difference except in fully developed horizontal pipe flow [70], where the time-averaged WSS ( $\bar{\tau}$ ) can be calculated from the streamwise pressure drop over a certain pipe length, as given by:

$$\bar{\tau} = \frac{D}{4} \left( -\frac{dP}{dx} \right) \quad (2-17)$$

where  $D$  is the pipe diameter. This relationship is therefore often used for the calibration of other pressure-difference based WSS measurement methods.

The Preston tube and the Stanton tube are actually Pitot tubes resting on the pipe wall for pressure measurements, from which the flow velocities are determined. The measured velocities ( $\bar{U}$ ) are correlated with the WSS by using the law of the wall of the viscous sublayer, as given by [29]:

$$\bar{U} = \frac{\bar{\tau}}{\mu} y \quad (2-18)$$

where  $\mu$  is the dynamic viscosity of the fluid and  $y$  is the distance to the wall. By calibrating with fully developed pipe flow (Equation (2-17)), the pressure measurements from the Preston tube and the Stanton tube can be related to WSS values [29].

The Preston tube and Stanton tube require a near-wall flow model (e.g., the law of the wall) and knowledge of the fluid properties (e.g., viscosity). In addition, physical obstacles in the pipes may interfere with the flow field [29], negatively affecting the accuracy of measurements. Last, but not least, these methods do not offer a temporal resolution for measuring the fluctuations in the flow.

#### *2.4.2.2 Methods based on Reynolds analogy*

The hot-film heat transfer sensor and the electrochemical mass transfer sensor have enjoyed popularity for WSS measurements [10,24,28,29]. Both methods rely on the Reynolds analogy between momentum transfer and heat/mass transfer. The principle of heat transfer and mass transfer WSS sensors is illustrated in Figure 2-11.

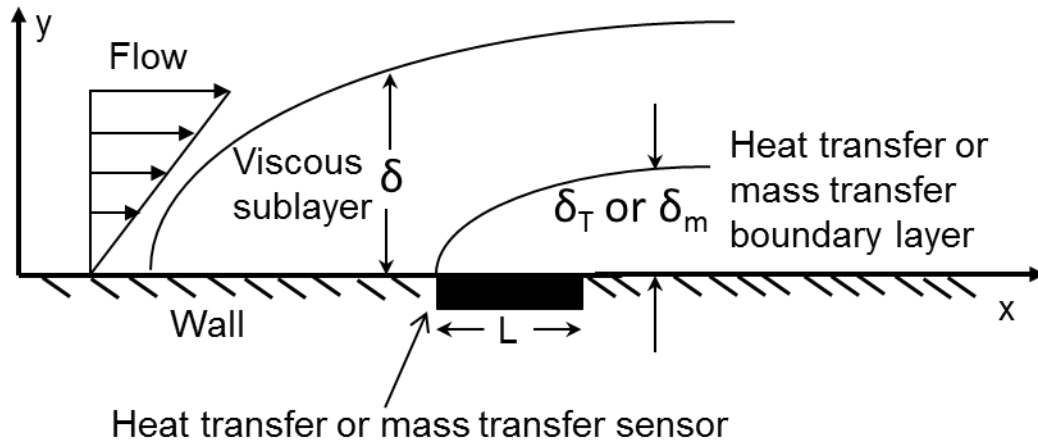


Figure 2-11: Schematic of heat or mass transfer WSS sensor (adapted from [28]).

In these methods, a small heat or mass transfer element is flush mounted on the wall. The fluid on the surface of the element maintains a constant mass concentration or temperature that is different from the bulk fluid, and the near-wall mass transfer or heat transfer rate is measured by the element [29]. If the streamwise length of the element ( $L$ ) is sufficiently small, its mass transfer or heat transfer boundary layer will be immersed within the momentum viscous sublayer of the flow field, where the velocity is linear to the distance  $y$  to the wall, as given by:

$$U = \frac{dU}{dy}y \quad (2-19)$$

For these sensors, a correlation between the measured mass or heat transfer rate and the  $y$ -direction velocity gradient ( $dU/dy$ ) is established [29]. With a given viscosity ( $\mu$ ), the WSS is then calculated as:

$$\tau = \mu \frac{dU}{dy} \quad (2-20)$$

Several assumptions need to be satisfied before a correlation can be established, as commented on by Hanratty and Campbell [29]. For example, the mass/thermal boundary layer over the sensor element lies within the viscous sub-layer; the diffusion in x direction can be neglected; and the width of the element is much larger than the mass transfer boundary layer thickness so that diffusion in the spanwise direction can be neglected.

The heat transfer sensor is essentially a temperature transducer measuring the heat transfer rate [28]. Ludwig and Tillmann [75] used the heat transfer method to measure the WSS; and they deduced that the heat flux was proportional to the WSS to the power of 1/3. The heat transfer sensor suffers from a coarse temporal resolution due to the limited thermal inertia of the element. In addition, an accurate calibration between the heat transfer rate and WSS is not easily obtained [28].

The electrochemical mass transfer sensor measures the mass transfer limiting current of an electrochemical reaction that occurs at the surface of the element. The limiting current is theoretically related to the mass transfer rate as given earlier in Equation (2-16). Therefore, calibration is not required for this method. By using the Reynolds analogy, the mass flux is proportional to the 1/3 power of the WSS [29]. The main disadvantage is that special chemical reagents with high electrochemical reactivity are needed in an aqueous flow, which is not suitable for studies of gas or pure water flow [70].

### 2.4.2.3 Methods based on optical techniques

Non-intrusive optical based measurements such as particle image velocimetry correlate the measured optical properties to the near-wall flow field and provide the WSS value from theoretical relationships. The principle of optical methods is illustrated in Figure 2-12.

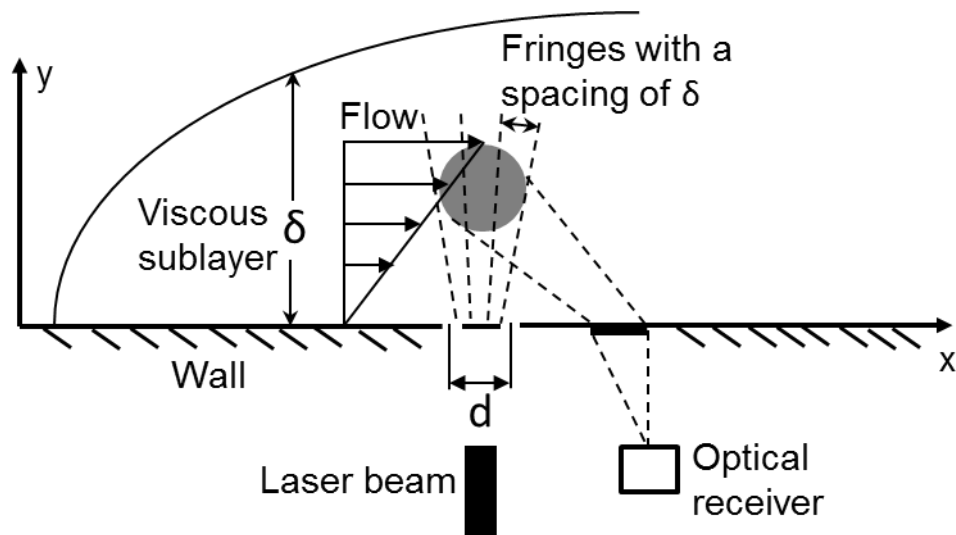


Figure 2-12: Schematic of laser-based WSS sensor (adapted from [70]).

A laser beam with a wavelength of  $\lambda$  passes through two closely spaced slits (a distance of  $d$ ). The diffracted light by the two slits generates interference fringes with a spacing of  $\delta$  [70]. The fringe spacing is a function of y-direction distance to the wall, as given by [70]:

$$\delta = \frac{\lambda}{d} y \quad (2-21)$$

When seeding particles are put in the flow, they will scatter light as they pass the fringes, resulting in Doppler shift of light at the Doppler frequency ( $f$ ) [70]:

$$f = \frac{U}{\delta} \quad (2-22)$$

where  $U$  is the particle velocity. The Doppler scattered light is then recorded by an optical receiver. If the particles are in the viscous sublayer, the velocity gradient  $dU/dy$  equals to  $U/y$  (see Equation (2-19)). Substitution of Equation (2-19), (2-21) and (2-22) into Equation (2-20) results in:

$$\tau = \frac{\mu f \lambda}{d} \quad (2-23)$$

Therefore, the WSS can be directly calculated from the measured Doppler frequency, without the need of calibration. This method allows for instantaneous WSS determination with a reported high accuracy [28,70]. On the other hand, several disadvantages are commonly associated with optical-based techniques. For instance, they require transparent fluids (e.g., air, water) and only work in single-phase flow. In addition, they are not suitable for measurements in pipes with curved walls.

### Chapter 3: Research Objectives

The primary objective of this research is to understand the mechanical effects of multiphase flow on CO<sub>2</sub> corrosion inhibition of carbon steel pipelines. The research focuses on answering the following question, can the hydrodynamic stresses produced by turbulent multiphase flow alone affect the protective corrosion product layers or corrosion inhibitor films?

Consequently, wall shear stress, one of the most important forms of mechanical stresses of flow, has been accurately measured for both single-phase flow and multiphase flow. In addition, the mechanical effect of extremely turbulent flow on adsorbed inhibitor films in a CO<sub>2</sub> corrosion environment has been investigated by laboratory experiments. Based on the literature review, research hypotheses were made and have been researched, as described below.

*Hypothesis:* Wall shear stress in multiphase flow is directly measurable with a floating element method. Instead of the more common indirect measurement of the wall shear stress, direct measurement does not rely on theoretical or empirical correlations between the WSS and the measured properties. Upon validation, this would be an effective means to study more complex multiphase flow environments.

*Hypothesis:* Corrosion product layers or inhibitor films are removed from the steel surface by high magnitude hydrodynamic stresses (e.g., wall shear stress). It was hypothesized that, turbulent flow, particularly multiphase flow, with high turbulence and fluid mixing, generates high mechanical stresses that exceed the adhesion strength of corrosion product layers or inhibitor films.

*Hypothesis:* Surface geometric irregularity affects local flow conditions, leading to high instantaneous hydrodynamic stresses, a failure of the corrosion inhibitor film and pitting corrosion. It was hypothesized that geometric irregularities on the surface of the pipe, e.g., misalignments, weld beads, bends, tees, etc., significantly alter the local hydrodynamic conditions and lead to, for example, severe WSS fluctuations. The high mechanical stresses and fluctuations cause the removal of corrosion product layers and inhibitor films.

In addition, a critical literature review on the following questions was deemed helpful for understanding the interaction between flow and corrosion inhibitors:

- What is the wall shear stress on an atomic level?
- How does flow interfere with the adsorption/desorption processes of inhibitor molecules?

Better understanding of these questions is important to link the flow (macroscopic) and the inhibitor molecule adsorption/desorption behavior at the metal surface (microscopic).

## Chapter 4: Experimental Methodology

In this chapter, the experimental details will be discussed, including the equipment, techniques and methods.

### 4.1 Physical Measurement of Wall Shear Stress

A floating element WSS probe manufactured by Lenterra, Inc.<sup>†</sup> was employed in this study [74] to directly measure the WSS. The top face of the floating element is flush mounted with the internal pipe wall and is sensitive to lateral displacement when there is fluid shearing over its surface. The schematic of the floating element WSS measurement system is shown in Figure 4-1, which comprises a probe, a controller and a computer. The probe consists of a floating element with a supporting cantilever, two optical strain gauges, and a probe enclosure. The circular-shaped floating element is set in a 1/4" (6.35 mm) cylindrical sensor enclosure with a fine external thread pitch of 1/80" (0.32 mm) to ensure a flush alignment with the pipe wall. The nominal gap between the edges of the floating element and the inner wall of the sensor enclosure is 100  $\mu\text{m}$ , which allows for the movement of the floating element. Two optical strain gauges, with fiber Bragg gratings (FBG), are attached to the cantilever. The FBGs are connected to the controller through optical fibers. The computer processes and stores the data. The floating element probe is made from stainless steel and glass fibers, and is therefore robust enabling it to work under fluid immersion conditions.

---

<sup>†</sup> Trade Name

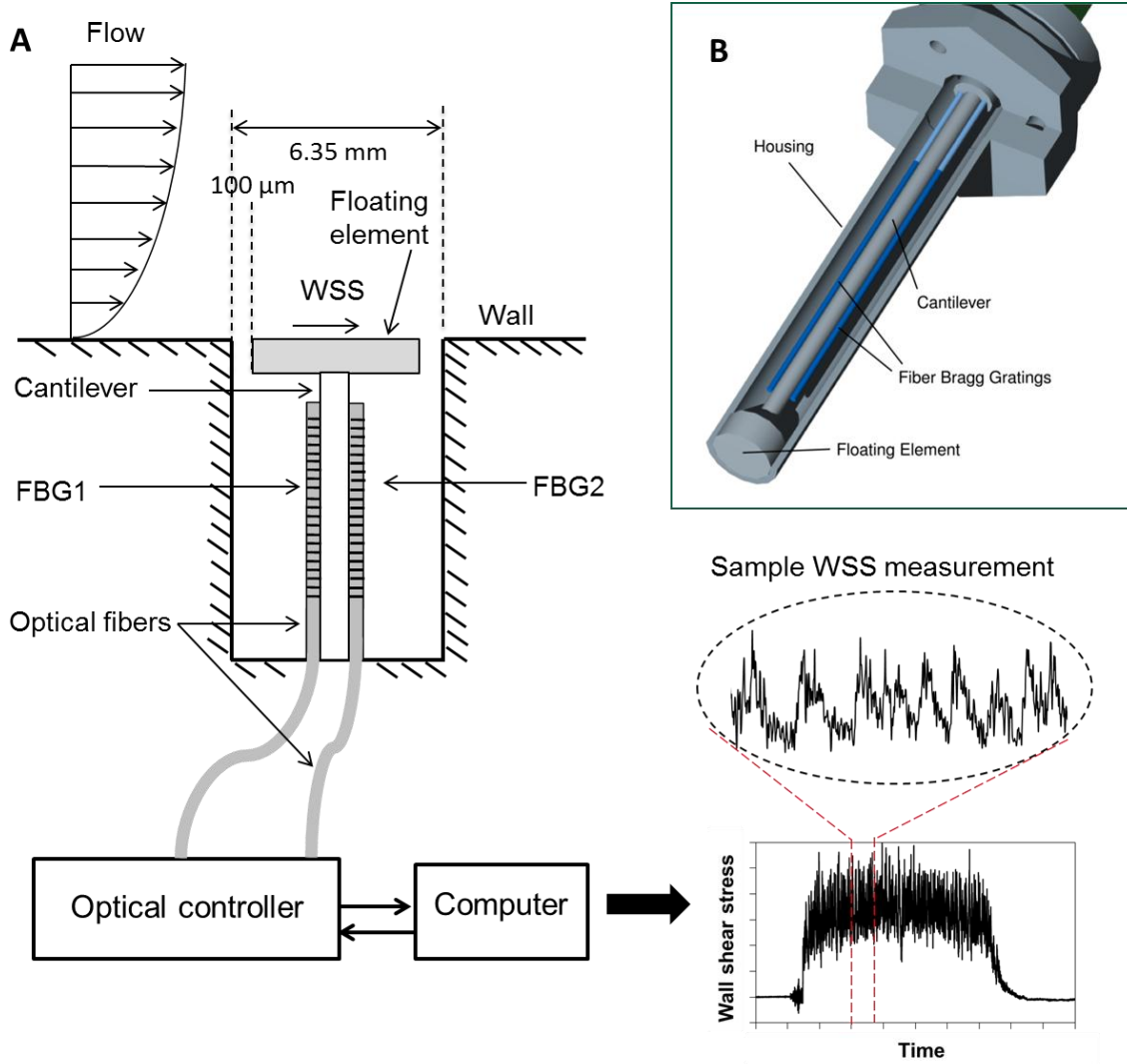


Figure 4-1: (A) Schematic of a floating element WSS measurement system showing sample measurement; (B) schematic diagram of WSS probe body (by Lenterra with permission).

In principle, direct measurements of WSS rely on accurately measuring the lateral displacement of the floating element. For this probe, the displacement of the floating element due to WSS is translated into the changes of optical signals transmitted by the FBG attached to the cantilever. Any small movement of the element and the consequent deformation of the cantilever will change the optical reflection spectra from the strain

gauges. The optical spectra are processed and provide a WSS value. During a measurement, the optical controller generates a monochromatic light beam from a laser diode. This light is directed to the FBG and the reflected light intensity is measured by a photodiode. The FBG only reflects light at its resonant wavelength and transmits all other wavelengths, which acts as an optical filter. While tuning the input laser wavelength, the reflection spectra (reflected light intensity versus laser wavelength) are recorded, from which the resonant wavelength is determined. The resonant wavelength shifts when the FBG is strained. Therefore, the WSS causing the displacement of the floating element and the deflection of the cantilever are represented by the resonant wavelength shift of the FBG. Temperature change also causes a shift of the resonant wavelength of the FBGs. Using two FBGs at opposite sides of the cantilever compensates for temperature sensitivity. When the cantilever is deflected by the flow, FBG1 is stretched and FBG2 is compressed (Figure 4-1). By subtracting their resonant wavelengths, the difference is independent of the temperature [74]. The difference between the resonant wavelengths of the two FBGs due to deflection of the cantilever provides the value of the exerted WSS on the floating element through the equation:

$$\tau = k\Delta\lambda \quad (4-1)$$

where  $\tau$  is the wall shear stress,  $k$  is a calibration coefficient, and  $\Delta\lambda$  is the difference between the resonant wavelengths of the two FBGs. The calibration coefficient is determined by applying a series of known shear forces to the floating element and measuring the corresponding values of  $\Delta\lambda$ . The WSS probe comes calibrated from the supplier.

In this study, two floating element WSS probes were used, one with a measurement range up to 100 Pa and the other with a measurement range up to 1000 Pa. Their nominal mechanical resonant frequencies are 105 Hz and 235 Hz, respectively. The typical data acquisition rate of the controller was set to 10k samples/s due to the limitations of the system hardware. The WSS data recording rate in the computer was set at either 100 Hz or 1000 Hz by averaging either 100 or 10 samples for each data point. The higher data recording rate of 1000 Hz provided finer temporal resolution, but also required more memory from the computer which limited the total recording time. For data recorded at 1000 Hz, a low-pass filter was applied to the raw data to remove the noise from the probe mechanical resonance. In the flow patterns studied here, no significant difference was observed when comparing data recorded at 100 Hz and 1000 Hz. Therefore, all the results reported below are based on data collected at 100 Hz, which allowed longer recording times.

## 4.2 Instrumentation and Methods for Flow Tests

In this study, a variety of flow equipment was employed to investigate both single-phase and multiphase flow patterns.

### *4.2.1 Equipment for single-phase flow*

Single-phase flow experiments were performed in two types of flow geometries: bounded channel flow and full pipe liquid flow. For channel flow, experiments were performed in a flow loop with a well-defined flow channel test section, which is referred

to as thin channel flow cell (TCFC). Visual representations for TCFC are shown in Figure 4-2. All wetted parts of the flow loop are made of 316 L stainless steel. A multistage centrifugal pump is employed to generate the flow. A liquid tank with a capacity of approximately 40 gallons (151 liters) is used to prepare and store test solution. The test section is a 600 mm long duct with a rectangular cross-section of 3 mm high and 89 mm wide. The small cross sectional area of the test section allows the mean flow velocity to reach up to 17 m/s. The mean volumetric flow is measured by a paddlewheel flow meter in a 2.54 cm ID (1 inch) pipe section downstream of the test section. The temperature of the test section and the liquid tank were constantly monitored by thermocouple probes. For high flow velocity tests, the heat generated in the pump was removed by a heat exchanger. In the TCFC test section, four ports spaced along the bottom of the channel are used to flush-mount plug-in probes such as a differential pressure transducer, wall shear stress measurement probe, electrochemical corrosion probe and weight loss corrosion specimens.

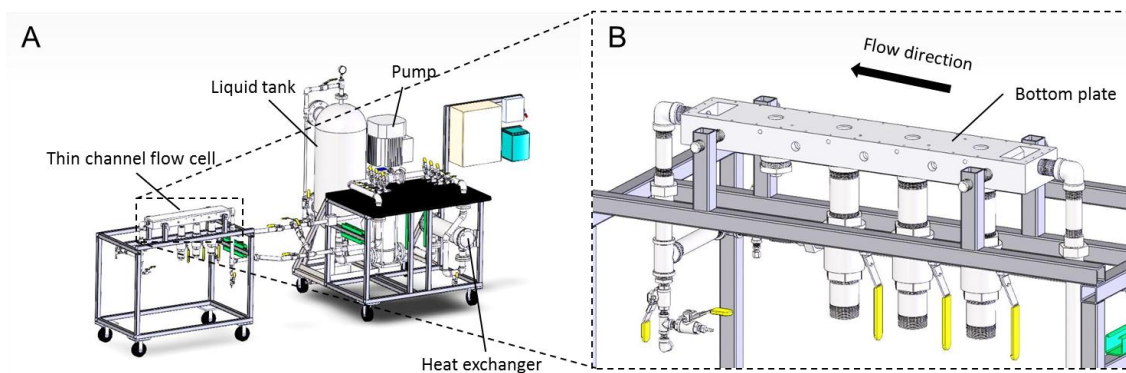


Figure 4-2: Visual representations of: (A) thin channel flow cell assembly and (B) zoomed-in view of the bottom plate of the test section (top lid not shown).

For single-phase pipe flow, a 1100 liter, 10.2 cm (4 inch) ID, 15 m long horizontal flow loop system was used (Figure 4-3). The test section is located about 11 m (109 pipe diameters) downstream of the inlet zone, which was deemed sufficiently long for the flow to fully develop. This flow loop was used for both single-phase and gas-liquid two-phase horizontal flow tests. The liquid velocity was measured by a paddlewheel flow meter for higher flow velocities ( $> 1$  m/s) and by an orifice plate flow meter for lower flow velocities ( $< 1$  m/s); and the gas velocity was measured by a hot wire anemometer. The hot wire anemometer came calibrated by the manufacturer. The liquid flow meters were calibrated using in-house procedures before the experiments, which are described in Appendix 2. Modifications to the WSS probe holder were made to ensure that the probe was truly flush with the circular cross section profile of the pipe, as shown in Figure 4-4.

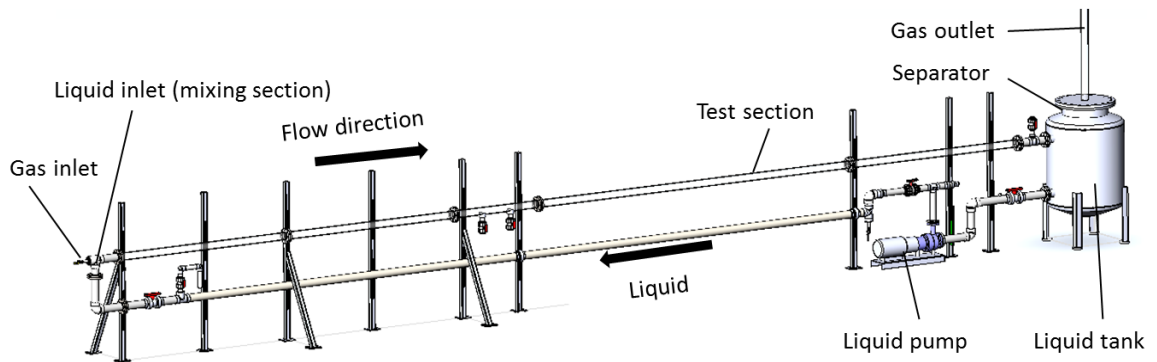


Figure 4-3: Representation of 10.2 cm ID (4 inch) pipe flow loop.

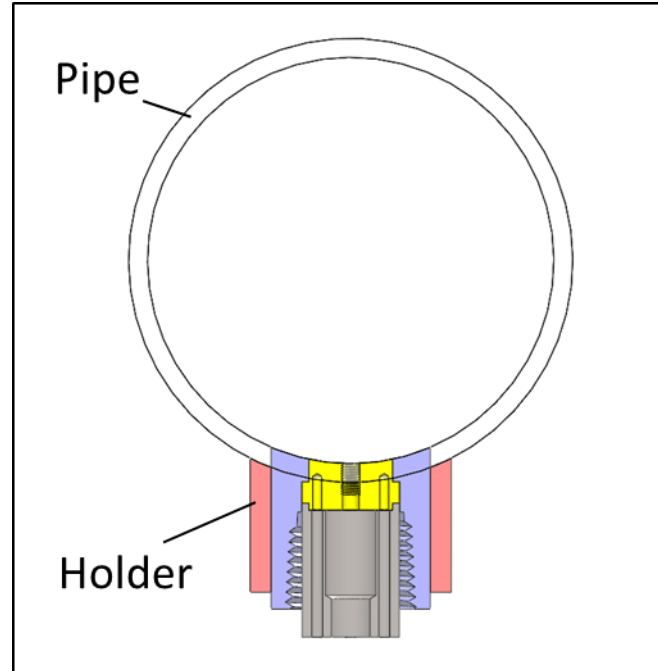


Figure 4-4: Schematic of the WSS probe holder flush-mounted to the pipe wall.

#### 4.2.2 Equipment for gas-liquid two-phase flow

Experiments of gas-liquid two-phase horizontal flow were performed in the earlier described 10.2 cm (4 inch) ID pipe flow loop and a 15.2 cm (6 inch) ID once-through flow system, as shown in Figure 4-5. The 15.2 cm ID once-through flow system is 37 m long. The test section is approximately 27.4 m (180 pipe diameters) downstream of the gas-liquid inlet mixing section. For both the 4 inch and 6 inch systems, transparent PVC pipe sections are used for flow visualization. The 4-inch flow loop has a broader superficial liquid velocity ( $V_{sl}$ ) range (up to 2.9 m/s) compared to the 6 inch system (up to 0.2 m/s). On the other hand, the 6-inch system has a ten times larger superficial gas velocity ( $V_{sg}$ ) range (up to 60 m/s). With these two systems, a wide range of horizontal

two-phase flow patterns was investigated. Stratified and slug flow were studied in the 4-inch flow loop, while annular (dispersed) flow was studied in the 6-inch flow system.

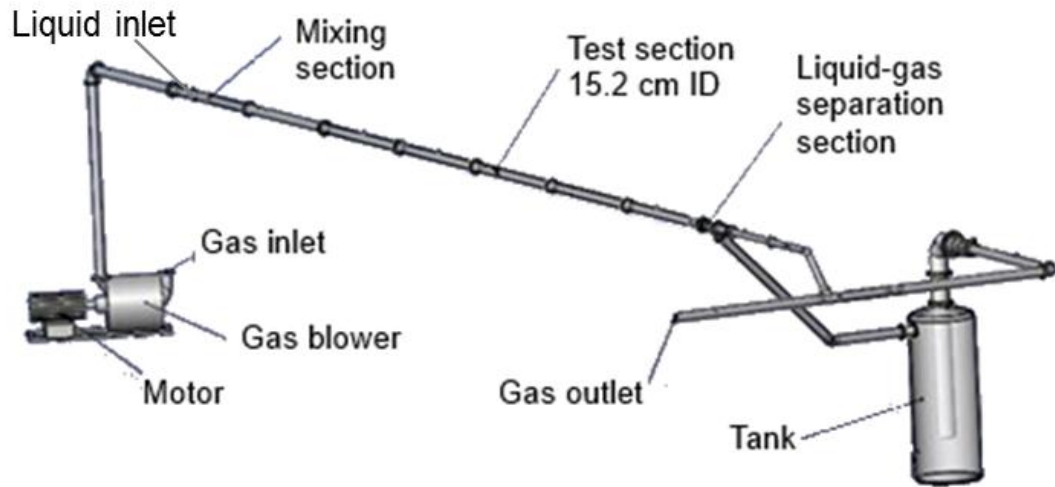


Figure 4-5: Representation of 15.2 cm ID (6 inch) once-through pipe system.

#### 4.2.3 Equipment for flow visualization

For two-phase flow, A Phantom V12.0\* digital high speed camera from Vision Research Inc. was employed for recording of the flow that was also synchronized with the WSS measurements. This allows for the observed and recorded flow events, such as a passage of slug, to be correlated with WSS data. In addition, the video data were also used to analyze hydrodynamic properties such as the flow velocity profile. Nikon† 50 mm and 105 mm lenses were used in this research. The former one provided a wide-angle view of the flow field, while the latter one focused on details. The typical video recording

---

\* Trade Name

† Trade Name

rate was 5000 fps (frames per second). A powerful light source (two 500 W lamps) was placed behind the pipe test section with a paper light diffuser to provide adequate and uniform illumination.

#### *4.2.4 Computational fluid dynamics (CFD)*

Computational fluid dynamics is a powerful tool for a wide range of physical modeling processes in fluid mechanics such as turbulence, multiphase flow, heat and mass transfer, and chemical reactions. In this research, ANSYS Academic Research<sup>‡</sup> R 14.0 and R 15.0 were employed for CFD simulations. The CFD results supplemented the experimental results of wall shear measurement in flow systems and allowed for estimations of local hydrodynamic properties, which are often not easy to obtain by experimental measurements.

### 4.3 Electrochemical Characterization Techniques for Corrosion Tests

Online corrosion measurements were conducted by using a Gamry Reference 600 Potentiostat/Galvanostat/ZRA<sup>†</sup>. Electrochemical techniques such as open circuit potential (OCP), linear polarization resistance (LPR), electrochemical impedance spectroscopy (EIS) and potentiodynamic polarization (PDP) were utilized. The typical parameter settings for these techniques are given in Table 4-1.

---

<sup>‡</sup> Trade Name

<sup>†</sup> Trade Name

Table 4-1: Typical parameter settings for electrochemical measurements

Techniques	Parameter Settings
LPR	Scan rate: 0.1 mV / s; Sample period: 1 s; Potential polarization range: -5 mV ~ +5 mV (vs. OCP).
EIS	Initial frequency: 100 kHz; Final frequency: 0.1 Hz. Points/decade: 5; AC voltage: 5 mV; DC voltage: 0 vs. OCP.
PDP	Scan Rate: 0.1667 mV / s; Sample period: 1 s; Anodic potential polarization range: 0 ~ +0.3 V (vs. OCP); Cathodic potential polarization range: 0 ~ -0.8 V (vs. OCP).

#### 4.4 Techniques for Surface Characterization

Multiple surface analysis techniques were employed to characterize the surface of corrosion specimens. A JEOL JSM-6390LV\* scanning electron microscope (SEM) coupled with energy-dispersive X-ray spectroscopy (EDS) was used to characterize the surface morphologies and to perform element analysis. In addition, an Alicona InfiniteFocus† 3D optical profilometer was utilized to measure the surface profiles of specimens, which allows for evaluation of the depth of pits in those cases with localized corrosion.

---

\* Trade Name

† Trade Name

## **Chapter 5: Direct Wall Shear Stress Measurements in Gas-Liquid Two-Phase Flow**

(Some contents in this chapter were presented in the paper no. 5922 at the NACE International CORROSION 2015 Conference [76], and have been accepted for publication in Corrosion Science (In Press) [77].)

### 5.1 Introduction

The adhesion strength of CO<sub>2</sub> corrosion inhibitor films or corrosion product layers to the steel surface is of the order 1 - 100 MPa, as discussed above. To answer the question as to whether turbulent flow could mechanically damage the protective inhibitor films or corrosion product layers, information regarding the magnitude of the hydrodynamic stresses produced by the flow, particularly wall shear stress (WSS), is required. In this chapter, single-phase liquid flow and selected, prevalent, gas-liquid two-phase flow patterns are studied by flow loop experiments; the WSS in these flow patterns are directly and accurately measured by employing a floating element method.

### 5.2 Experimental Methodology

In this research, WSS measurements were performed using the floating element WSS probes (described in Chapter 4) in both single-phase and multiphase flows. Baseline tests in single-phase flow were done to check the performance of the WSS probe and lay the groundwork for applications in more complicated flow environments, such as two-phase flow where accurate WSS predictions were expected to be more difficult.

Single-phase flow patterns were studied in the TCFC and the 4-inch pipe loop, while horizontal gas-liquid two-phase flow patterns were investigated in the 4-inch pipe loop and the 6-inch flow system (described in Chapter 4). For single-phase flow, WSS was measured in the bounded channel flow and pipe flow with the test matrix shown in Table 5-1. For two-phase flow patterns, since the phases are not homogeneously distributed over the pipe cross-section, it was necessary to measure the WSS circumferentially around the pipe. Consequently, WSS measurements were conducted at three locations on the pipe wall (bottom, top and side) with the test matrix given in Table 5-2. WSS measurements were taken with at least one repeat for each flow condition. The summary of all two-phase flow conditions, for which data were collected, is shown in the context of a two-phase flow pattern map generated by an in-house gas-liquid flow model [63] (Figure 5-1). The flow transition lines between stratified-wavy and annular-mist flow for the 4 inch and 6 inch ID lines, carrying CO<sub>2</sub> and air, respectively, are very similar; therefore, the annular-mist flow data obtained from the 6 inch line was plotted alongside the data collected in the 4 inch line in the same flow pattern map.

Recorded flow visualization was provided by the earlier described high speed video camera system in Chapter 4, aiming to contribute to better understanding of the complex hydrodynamic properties in two-phase flow.

Table 5-1: Test matrix for single-phase flow

<b>Parameter</b>	<b>Channel Flow</b>	<b>Pipe Flow</b>
Fluid	Deionized water	Deionized water
Flow cross section	3mm x 89mm	102 mm diameter
Flow velocity	2 m/s – 17 m/s	1 m/s – 2.9 m/s
Pipe material	Stainless steel	PVC pipe
Temperature/pressure	25°C / 1 atm	25°C / 1 atm

Table 5-2: Test matrix for gas-liquid two-phase flow

<b>Parameter</b>	<b>10.2 cm ID flow loop</b>	<b>15.2 cm ID once-through</b>
Liquid	Water	Water
Gas	CO <sub>2</sub>	Air
Superficial liquid velocity	0.1 m/s - 2.9 m/s	0.017 m/s - 0.17 m/s
Superficial gas velocity	0.2 m/s - 5 m/s	42 m/s
Pipe Material	PVC pipe	PVC pipe
Temperature/pressure	25°C / 1 atm	25°C / 1 atm
Studied flow patterns	Stratified flow, slug flow	Annular flow

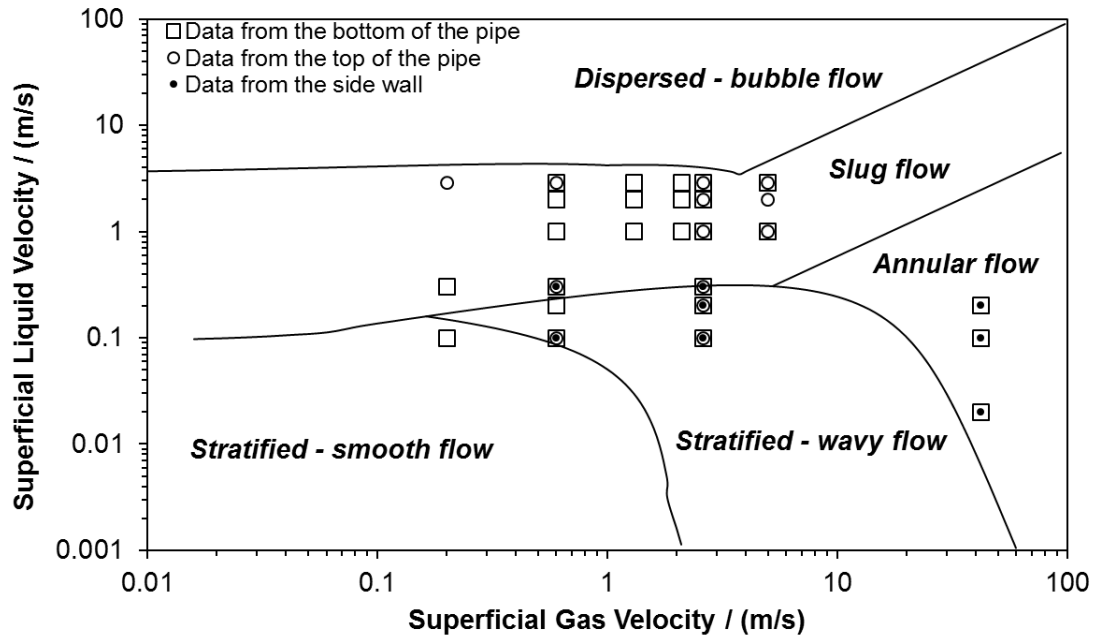


Figure 5-1: Tested flow conditions for WSS measurements in a horizontal two-phase flow pattern map [63] for 1 bar, 25°C, CO<sub>2</sub>-water, and 4-inch pipe loop.

### 5.3 Wall Shear Stress Measurements in Single-Phase Flow

To evaluate the validity of WSS measurements made by the floating element probes, the measured values were compared to empirical well known single-phase correlations and CFD simulations.

Correlations for calculating mean WSS in single-phase flow are well-established. The relationship between time-averaged WSS ( $\tau$ ) and mean flow velocity for single-phase flow can be expressed as:

$$\tau = \frac{1}{2} \rho C_f V^2 \quad (5-1)$$

where  $\rho$  is the fluid density ( $\text{kg/m}^3$ ),  $C_f$  is the Fanning friction factor, and  $V$  is the mean flow velocity (m/s). The Fanning friction factor is a function of the Reynolds number ( $Re$ ) and surface roughness. The Reynolds number is defined as:

$$Re = \frac{\rho V d}{\mu} \quad (5-2)$$

where  $\mu$  is the dynamic viscosity of the fluid (Pa·s) and  $d$  is the hydraulic diameter (m).

For channel flow, the Patel correlation for a smooth surface can be used to calculate the friction factor [78]:

$$C_f = 0.0376 Re^{-1/6} \quad (5-3)$$

The height of channel ( $h$ ), instead of  $2h$ , was used as the characteristic length to calculate the Reynolds number as discussed before by Patel et al. [78].

For pipe flow, the Blasius friction factor for a smooth pipe wall was used [78]:

$$C_f = 0.079 Re^{-1/4} \quad (5-4)$$

The WSS can be calculated by using the above equations as long as the flow velocity, pipe dimensions, and fluid properties are determined. The measured WSS from experiments was compared to the calculated values for both channel and pipe flow. The mean WSS measured in channel flow shows a reasonably good agreement with the Patel correlation over a wide range of flow velocities (Figure 5-2). The measurements from pipe flow are also consistent with the calculated values using the Blasius correlation, as shown in Figure 5-3. The error bars in the graphs represent the maximum and minimum values of the WSS measurements.

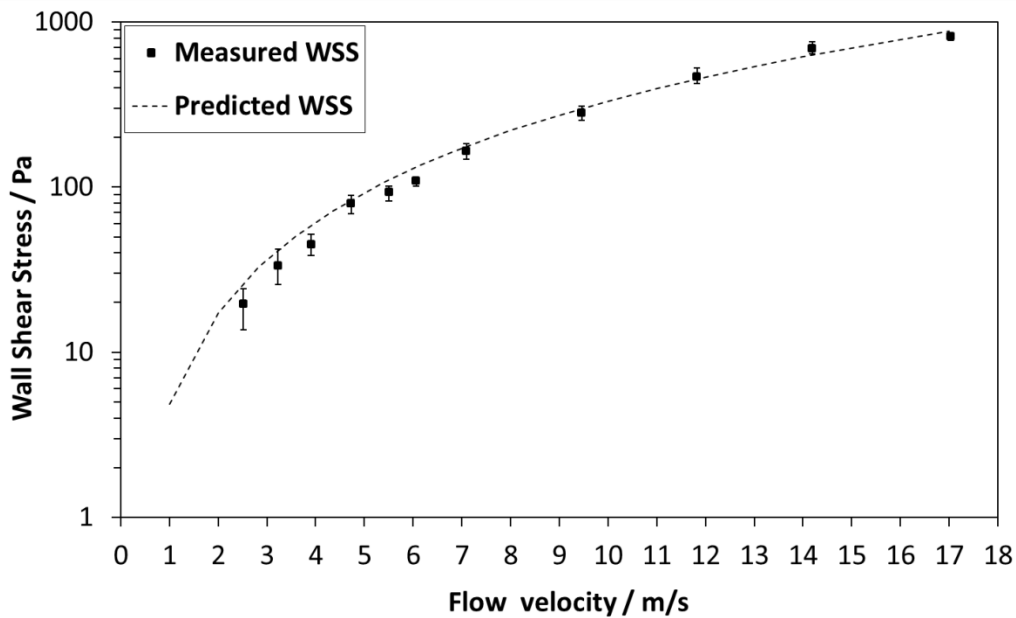


Figure 5-2: Comparison of measured WSS values with Patel calculations for channel flow ( $h=3$  mm).

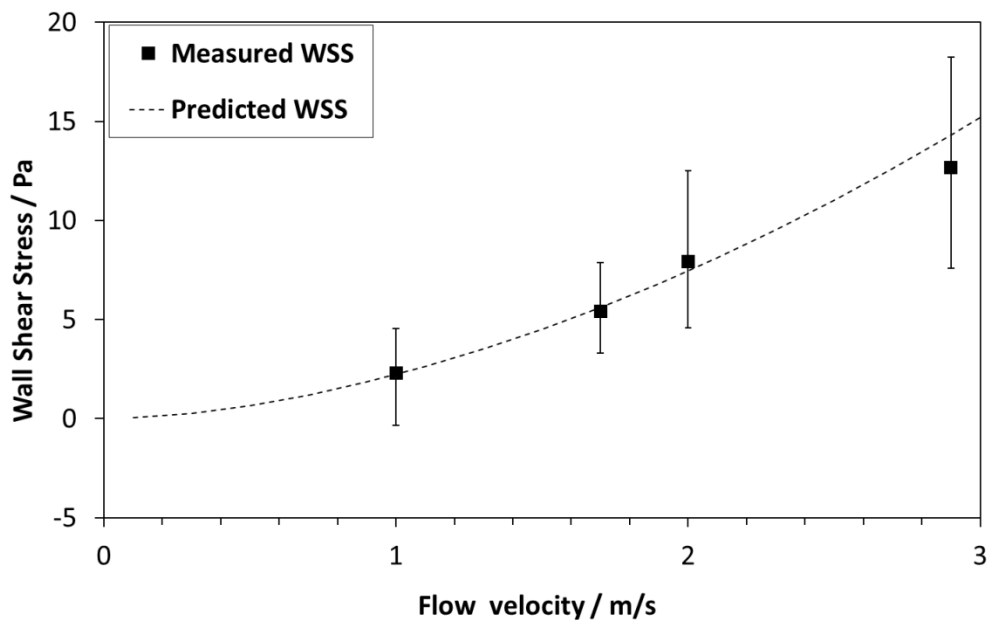


Figure 5-3: Comparison of measured WSS values with calculations for pipe flow ( $ID=0.102$  m).

In addition, CFD simulations of the thin channel flow cell were performed. The simulation geometry is shown in Figure 5-4. As the height of the thin channel (y direction) is only 3mm, several meshing parameters were adjusted in order to accommodate sufficient mesh layers in the y direction. Figure 5-5 shows the mesh structure on the x-y plane in the thin channel. Energy and viscous models were selected to conduct the single-phase turbulent flow simulations. In the viscous model (turbulent model), the standard k-epsilon model was selected. The Standard Wall Functions [79] were selected as the near-wall treatment. After setting up proper boundary conditions, simulations were performed until all momentum and energy equations converged. Since wall functions were used in the simulations, the results were checked to ensure that sufficient mesh cells were within the boundary layers. Simulations with various flow velocities were conducted and provided calculated WSS values. To illustrate the simulation results by an example, Figure 5-6 shows the WSS distribution of the four ports at the bottom plate of the TCFC when the flow velocity is 9.5 m/s. The similarity of the WSS values suggests that the flow around these port locations is fully developed.

The WSS values obtained from different methods were compared, as shown in Figure 5-7. The error bars in the graph represent the maximum and minimum values of the WSS using different methods. The agreement for single-phase flow results demonstrates that the WSS probe had been properly calibrated and was ready for application in two-phase flow situations.

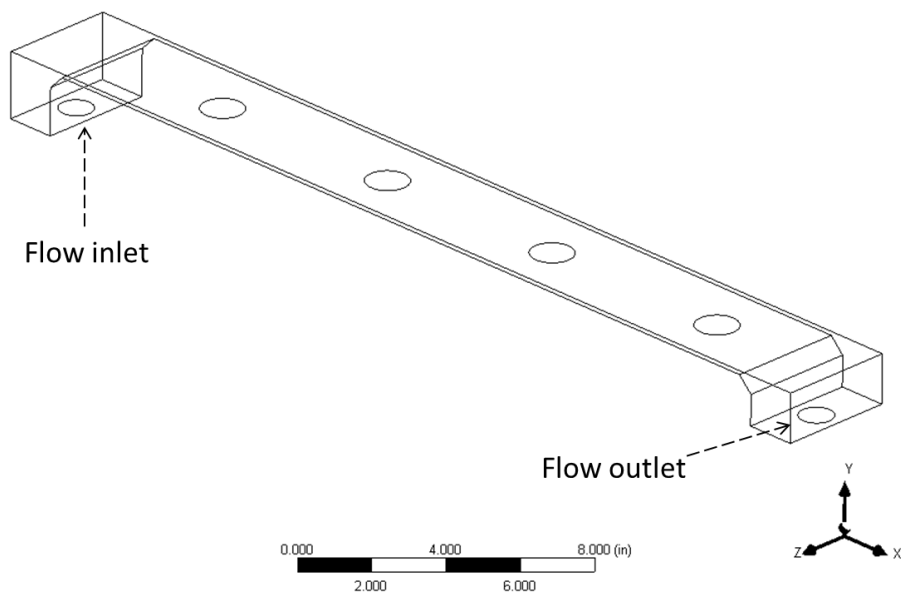


Figure 5-4: ANSYS geometry for the test section of the thin channel flow cell.

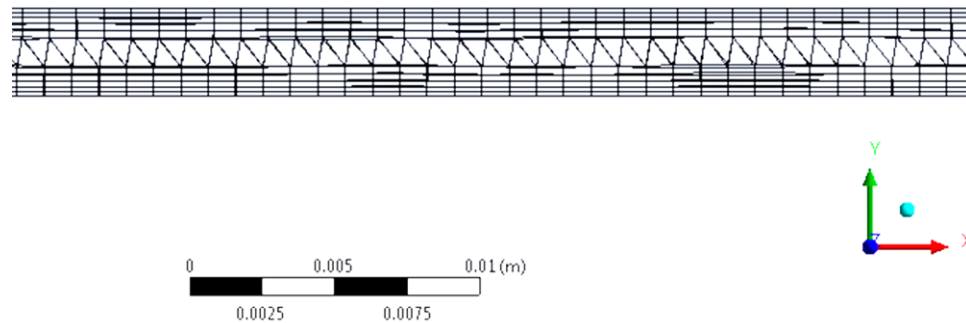


Figure 5-5: Mesh structure in the thin channel flow cell, a view from z-direction.

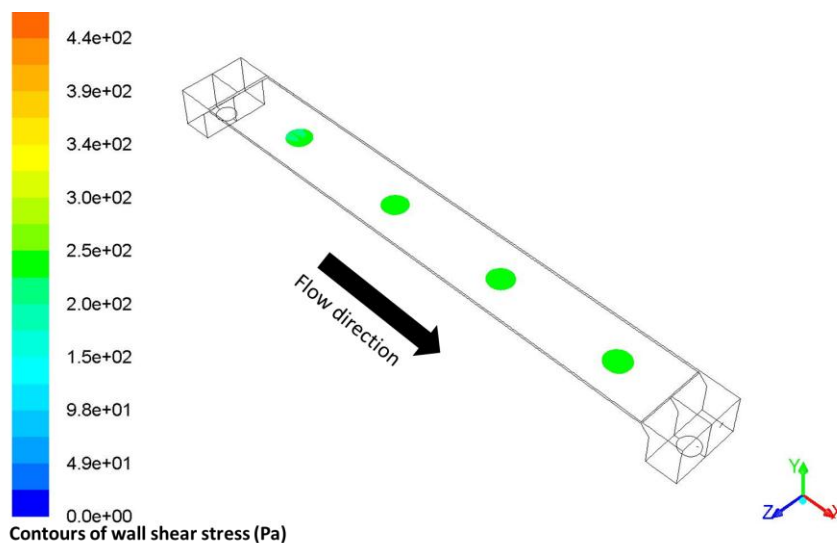


Figure 5-6: WSS distribution at the port locations by CFD simulation. 25°C, 9.5 m/s in the thin channel flow cell.

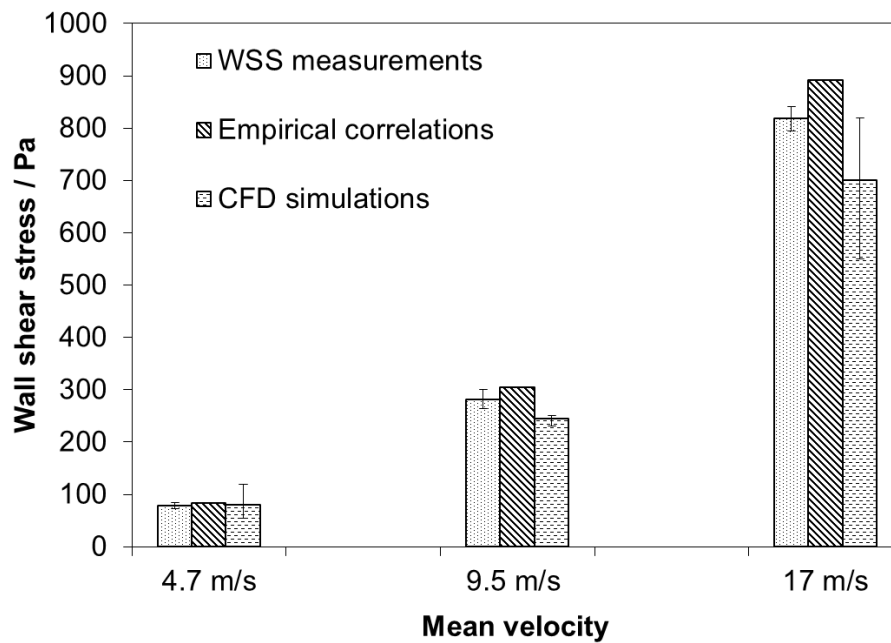


Figure 5-7: Comparison of WSS values obtained by different methods.

#### 5.4 Wall Shear Stress Measurements in Gas-Liquid Two-Phase Horizontal Pipe Flow

WSS in multiphase flow exhibits much more complicated behavior compared to single-phase flow, particularly due to the changes of the liquid phase distribution and velocity over time and in space. Since there are no well-established WSS correlations for multiphase flow, direct WSS measurements were seen as a means for contributing to a better understanding of observed flow-related phenomena.

##### *5.4.1 Wall shear stress measurements in slug flow*

Slug flow is considered to be one of the most turbulent multiphase flow patterns [10]. In addition, due to its frequent occurrences in pipelines over a wide range of gas and liquid flow velocities, understanding the hydrodynamics of slug flow was deemed an important objective in this study. The features of horizontal slug flow were described earlier in Figure 2-6. With high turbulence and gas/liquid mixing, the overall slug body moves at a mixture velocity averaged over the cross-section of the pipe, as given by:

$$V_m = V_{sl} + V_{sg} \quad (5-5)$$

In the stratified zone, a relatively slow liquid film is moving at the bottom, with faster moving gas above. Due to this inhomogeneous distribution of phases, the WSS values should be expected to be different around the pipe circumference.

WSS measurements were taken at three locations on the pipe wall (bottom, top and side). A repeatable procedure was used for measuring WSS at each of these locations. To illustrate this procedure with an example, Figure 5-8(A) shows the data from a test at  $V_{sl} = 2.0$  m/s and  $V_{sg} = 2.1$  m/s with the WSS probe flush mounted at the bottom of the

pipe. A full measurement sequence consists of several steps: (a) the WSS probe started recording data at 0 s with no flow; (b) the gas was introduced into the flow loop and reached the required superficial velocity gradually over 10 to 15 s; (c) the liquid was introduced into the flow loop and reached the specified superficial velocity (data between the 15 - 20 s markers in Figure 5-8(A)); (d) slug flow became fully developed between 20 - 70 s; (e) the liquid supply was shut off after 70 s; (f) the gas supply was shut off between 80 - 90 s; and (g) the WSS was recorded for another 10 s in order to confirm that there was no offset in the measurement from beginning to end. Although the specific times may vary from test to test, the measurement procedure was the same.

Figure 5-8(B) shows an expanded section of the WSS data taken at the bottom of the pipe for the fully developed slug flow, covering the time period between the dotted lines in Figure 5-8(A). The expanded graph shows a series of distinct wall shear stress peaks, which are presumably corresponding to the passage of slugs.

Figure 5-9 shows a typical WSS measurement at the top of the pipe, which presents a different pattern, compared to that at the pipe bottom. The WSS peaks are more pronounced than those seen at the bottom, with much smaller base WSS values in between. The video data confirmed that the shear stress peaks from both pipe bottom and top coincided with liquid slug body passages. Three peaks from both Figure 5-8(B) and Figure 5-9(B) are labeled with time stamps, which will be discussed in the next section. A number of WSS measurements were taken at the side wall of the pipe, which showed a similar measurement pattern as seen for the top (as exemplified in Figure 5-10).

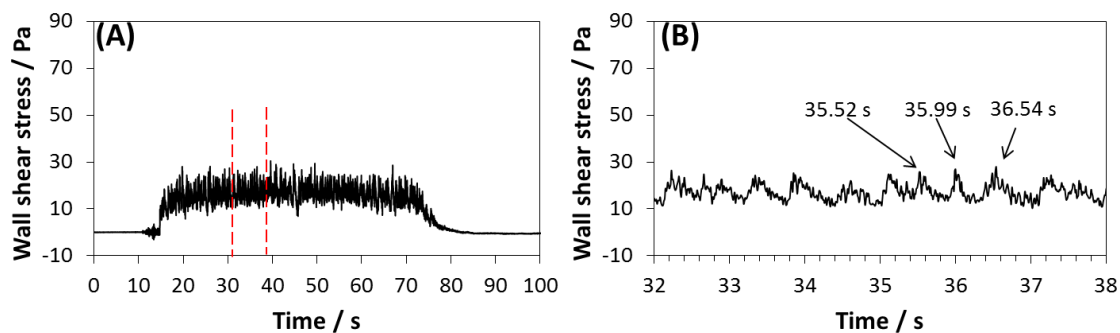


Figure 5-8: Wall shear stress measurement at the bottom of the 4 inch pipe for  $V_{sl} = 2.0$  m/s,  $V_{sg} = 2.1$  m/s: (A) the full recording sequence; (B) data between 32 and 38 seconds (See Figure 5-20 for the synchronized video frames of the labeled peaks).

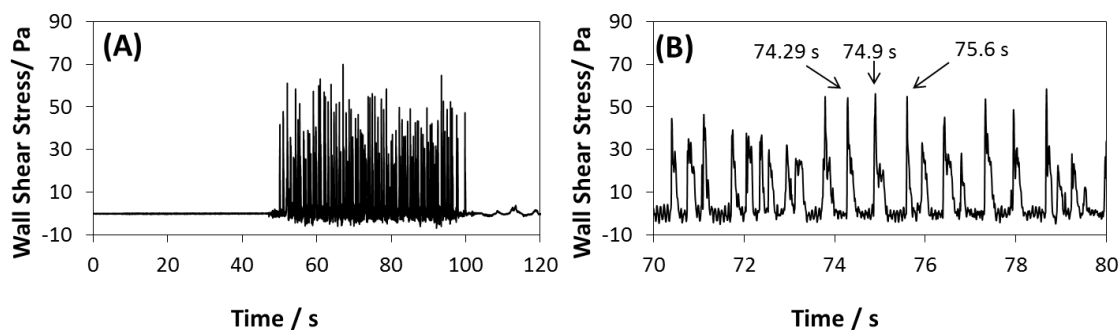


Figure 5-9: Wall shear stress measurement at the top of the 4 inch pipe loop for  $V_{sl} = 2.0$  m/s,  $V_{sg} = 2.6$  m/s: (A) the full recording sequence; (B) data between 70 and 80 seconds (See Figure 5-21 and Figure 5-22 for the synchronized video frames of the labeled peaks).

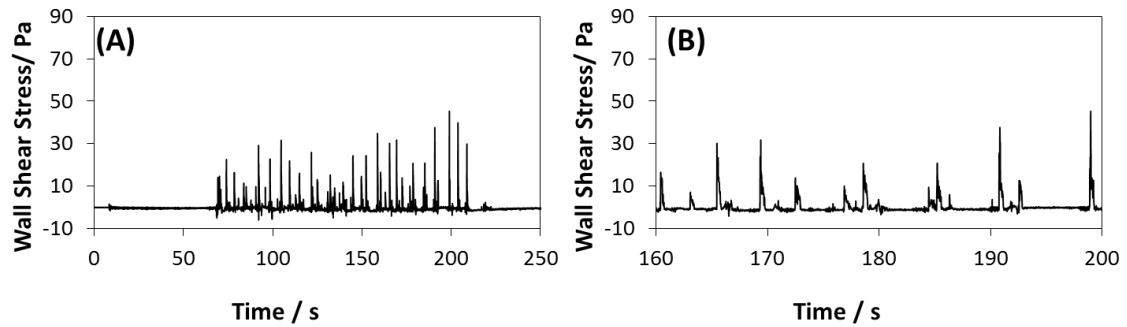


Figure 5-10: Wall shear stress measurement at the sidewall of the 4 inch pipe loop for  $V_{sl} = 0.3$  m/s,  $V_{sg} = 2.6$  m/s: (A) the full recording sequence; (B) data between 160 and 200 seconds.

The different patterns of the WSS data taken for different locations of the pipe circumference can be easily explained by the characteristics of horizontal slug flow. When the WSS probe was at the bottom, it was constantly immersed in a moving liquid phase, either in the form of a stratified film or a liquid slug body. As shown in Figure 5-8(B), the base WSS value of about 15 Pa was due to the movement of the stratified film between the slugs, which caused peak WSS up to 29 Pa. On the other hand, when the WSS probe was at the top, there was a measurable WSS only when the liquid slug body was bridging the entire pipe cross-section as it passed over the probe. Without the liquid slug, the gas phase exerted a negligible WSS on the probe, due to its low density as compared to the liquid phase. This is evident by the WSS data shown in Figure 5-9(B) where the measured WSS was almost zero between peaks, when no liquid slug body was present. The patterns of the WSS data at the sidewall suggest that the height of the liquid phase in the stratified film zone was much lower than the probe location, and WSS was recorded only when the liquid slug zone passed the probe. This is a reasonable

explanation as the liquid velocities were relatively low for WSS measurements at the sidewall of the pipe.

It was generally found that an increasing mixture velocity leads to an increasing WSS value at each of the probe locations. The maximum WSS values measured at the bottom, top, and side of the pipe for each condition are tabulated in Table 5-3. The maximum WSS value was determined by averaging the largest 20 values for each flow condition, in order to get a more representative value that can be used for modeling. To demonstrate this increase in WSS with increasing mixture velocity, Figure 5-11 to Figure 5-13 show the maximum WSS value measured for each condition around the pipe circumference, overlain with the corresponding two-phase flow pattern map. It should be noted that in some of the test conditions stratified flow was predicted by the flow pattern map, while it was actually slug flow (Figure 5-11) as confirmed by the video data. This is probably due to these conditions being close to the transition line between stratified flow and slug flow, and the inherent inaccuracy of the model used. Similarly, the maximum WSS values for tests at  $V_{sl} = 2.9$  m/s,  $V_{sg} = 0.2$  m/s and 0.6 m/s were unreported (Figure 5-12), as transitions between slug flow and dispersed-bubble flow were observed from the video data.

Table 5-3: Wall shear stress measurements for slug flow in the 4 inch pipe loop

Probe location	$V_{sl}$ / (m/s)	$V_{sg}$ / (m/s)	$V_m$ / (m/s)	Max WSS / (Pa)
Bottom	0.1	0.2	0.3	1
Bottom	0.1	0.6	0.7	2
Bottom	0.1	2.6	2.7	7
Bottom	0.2	0.6	0.8	2
Bottom	0.2	2.6	2.8	8
Bottom	0.3	0.2	0.5	1
Bottom	0.3	0.6	0.9	2
Bottom	0.3	2.6	2.9	10
Bottom	1.0	0.6	1.6	9
Bottom	1.0	1.3	2.3	12
Bottom	1.0	2.1	3.1	23
Bottom	1.0	2.6	3.6	22
Bottom	1.0	5.0	6	35
Bottom	2.0	0.6	2.6	24
Bottom	2.0	1.3	3.3	27
Bottom	2.0	2.1	4.1	28
Bottom	2.0	2.6	4.6	27
Bottom	2.9	1.3	4.2	29
Bottom	2.9	2.1	5.0	34
Bottom	2.9	2.6	5.5	38
Bottom	2.9	5.0	7.9	54
Top	0.1	0.6	0.7	18
Top	0.1	2.6	2.7	31
Top	0.2	2.6	2.8	41
Top	0.3	0.6	0.9	22
Top	0.3	2.6	2.9	36
Top	1.0	2.6	3.6	52
Top	1.0	5.0	6	75
Top	2.0	2.6	4.6	58
Top	2.0	5.0	7.0	79
Top	2.9	2.6	5.5	59
Top	2.9	5.0	7.9	80
Side	0.1	0.6	0.7	5
Side	0.1	2.6	2.7	17
Side	0.2	2.6	2.8	21
Side	0.3	0.6	0.9	10
Side	0.3	2.6	2.9	32

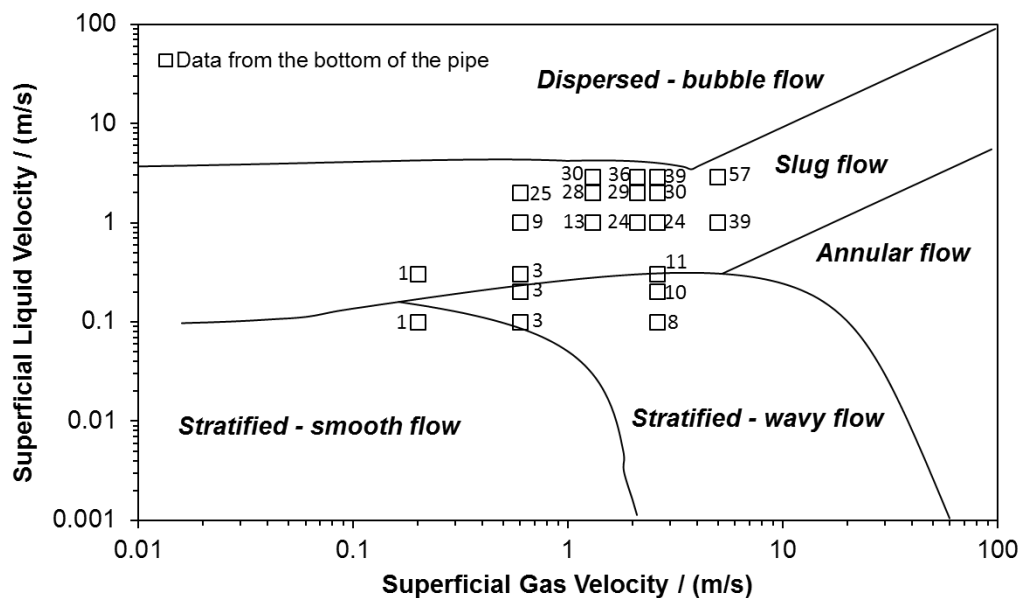


Figure 5-11:  $\tau_{\max}$  (Pa) shown next to markers for slug flow measured at the bottom of the pipe overlain with the flow pattern map [63], at 1 bar, 25°C, CO<sub>2</sub>-water, and in the 4-inch loop.

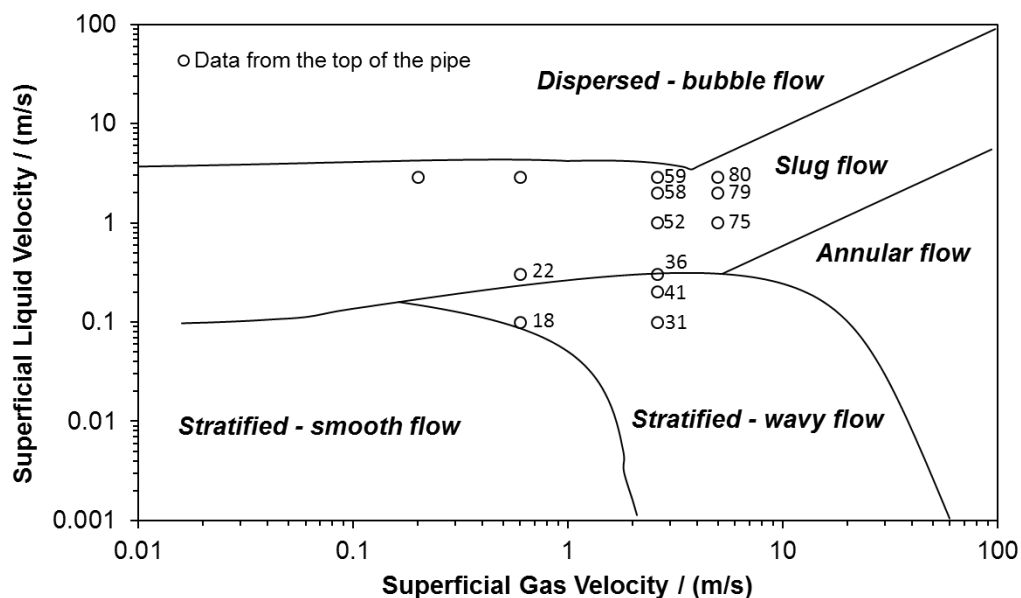


Figure 5-12:  $\tau_{\max}$  (Pa) shown next to markers for slug flow measured at the top of the pipe overlain with the flow pattern map [63], at 1 bar, 25°C, CO<sub>2</sub>-water, and in the 4-inch loop.

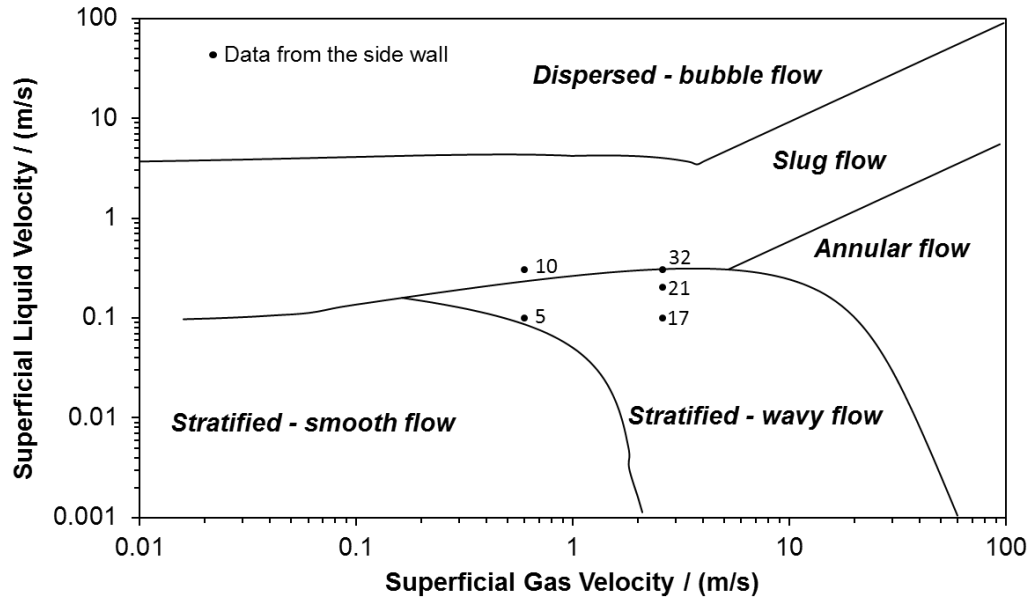


Figure 5-13:  $\tau_{\max}$  (Pa) shown next to markers for slug flow measured at the sidewall overlain with the flow pattern map [63], at 1 bar, 25°C, CO<sub>2</sub>-water, and in the 4-inch loop.

To interpret the measured maximum WSS in the slug body, stresses are compared with calculated values. Although there is no correlation for maximum WSS in slug flow, the mean WSS in the slug body ( $\tau_s$ ) has been calculated using an equation similar to that for single-phase flow [62], as given by:

$$\tau_s = \frac{1}{2} \rho_s C_{f,s} V_s^2 \quad (5-6)$$

where  $\rho_s$  is the average fluid density of the slug body (kg/m<sup>3</sup>),  $C_{f,s}$  is the Fanning friction factor of the slug body and  $V_s$  is the slug body velocity (m/s). The mixture velocity ( $V_m$ ) is usually used as the slug body velocity in Equation (5-6) to calculate the mean WSS, but the maximum local velocity is needed in order to calculate the maximum WSS. This local flow velocity is expected to be higher at the top of the pipe and lower at the bottom.

To calculate the friction factor in Equation (5-6), the Blasius-type correlation for smooth pipes was used:

$$C_{f,s} = 0.079Re_s^{-1/4} \quad (5-7)$$

where the Reynolds number of the slug body ( $Re_s$ ) using the pipe diameter ( $D$ ) was written as:

$$Re_s = \frac{\rho_s DV_s}{\mu_s} \quad (5-8)$$

The average slug body density ( $\rho_s$ ) and viscosity ( $\mu_s$ ) were calculated as:

$$\rho_s = \rho_L H_{ls} + \rho_G (1 - H_{ls}) \quad (5-9)$$

$$\mu_s = \mu_L H_{ls} + \mu_G (1 - H_{ls}) \quad (5-10)$$

where  $\rho_L$  and  $\mu_L$  are the liquid density and viscosity,  $\rho_G$  and  $\mu_G$  are the gas density and viscosity, and  $H_{ls}$  is the slug liquid holdup. A correlation for horizontal flow by Gregory et al. [80] was used to calculate the slug liquid holdup:

$$H_{ls} = \frac{1}{1 + \left(\frac{V_m}{8.66}\right)^{1.39}} \quad (5-11)$$

By using Equation (5-6) through Equation (5-11), the slug WSS can be calculated using the average slug body density and viscosity and a defined slug body velocity, as given by:

$$\tau_s = 0.0395 \cdot D^{-0.25} \rho_s^{0.75} \mu_s^{0.25} V_s^{1.75} \quad (5-12)$$

The mean WSS of the slug body is compared with the measured maximum WSS for each flow condition in Figure 5-14. Generally, the measured maximum WSS values for all probe locations are higher than the calculated values when using the mixture velocity. This finding is important as many slug flow models only calculate the mean shear stress of the slug body by using the mixture velocity, which can underestimate the maximum

WSS by a large margin (a factor of 2-4). The finding also indicates that the highest WSS value occurred when the liquid slug passed the probe with a local velocity being higher than the mixture velocity. In addition, it was found that at the same flow condition, the maximum WSS at the top of the pipe was higher than that measured at the bottom of the pipe, while the maximum WSS measured at the sidewall was an intermediate value. It was assumed that the difference among the maximum WSS values at these three probe locations was due to the variation of the local liquid flow velocity in the slug body. In other words, the top part of the slug body had a higher maximum flow velocity than the bottom part of the slug body.

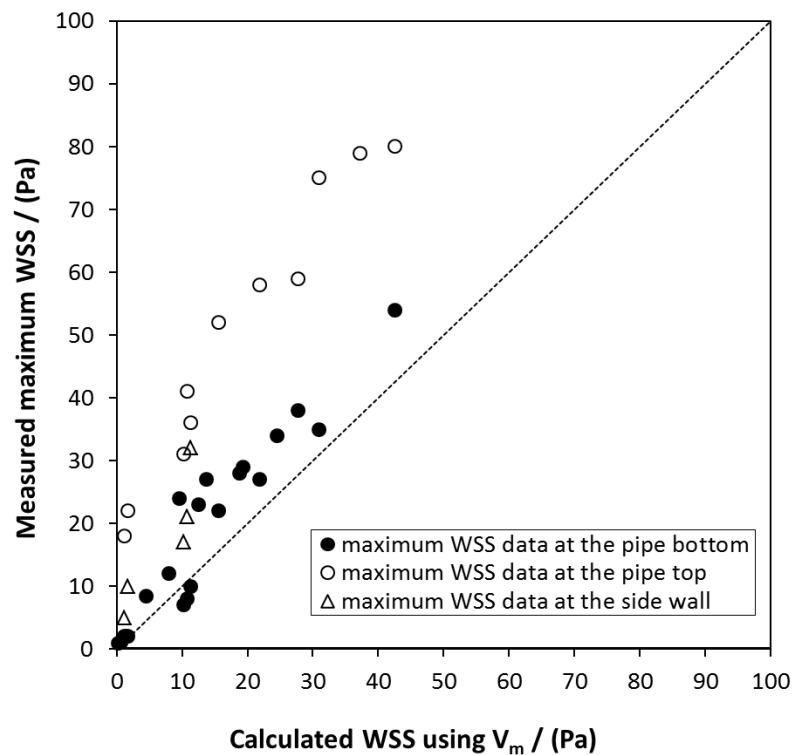


Figure 5-14: Comparison between measured maximum WSS values and calculated mean slug WSS values from Equation (5-12) by using mixture velocity ( $V_m$ ), for 4-inch loop.

To better predict the maximum WSS, the maximum local velocity in the slug body was required. The in situ local velocity of the liquid in the slug body was determined using video data, as illustrated in Figure 5-15. Two images of a liquid slug with a small time separation  $\Delta t$  (0.003 s) were compared. To determine actual liquid velocities, small gas bubbles, entrained by the liquid, were used as tracers to determine liquid velocities. For example, using Figure 5-15, the in situ liquid velocity at the pipe top near the slug front was calculated as  $\Delta x_1/\Delta t$ . For low-quality images, the slug nose interface near the top was used as a tracer to estimate the liquid velocity. It should be noted that this interface velocity, or slug translational velocity, is not an actual liquid velocity. Because of the scooping up of the liquid from the stratified film into the slug body, the translational velocity is higher than the mixture velocity. Nevertheless, the translational velocity was deemed the maximum possible local velocity in the slug body [62]. Similarly, by tracking the horizontal movement of a small gas bubble in the slug body near the pipe bottom ( $\Delta x_2$ ), the local liquid velocity at the pipe bottom was calculated as  $\Delta x_2/\Delta t$ .

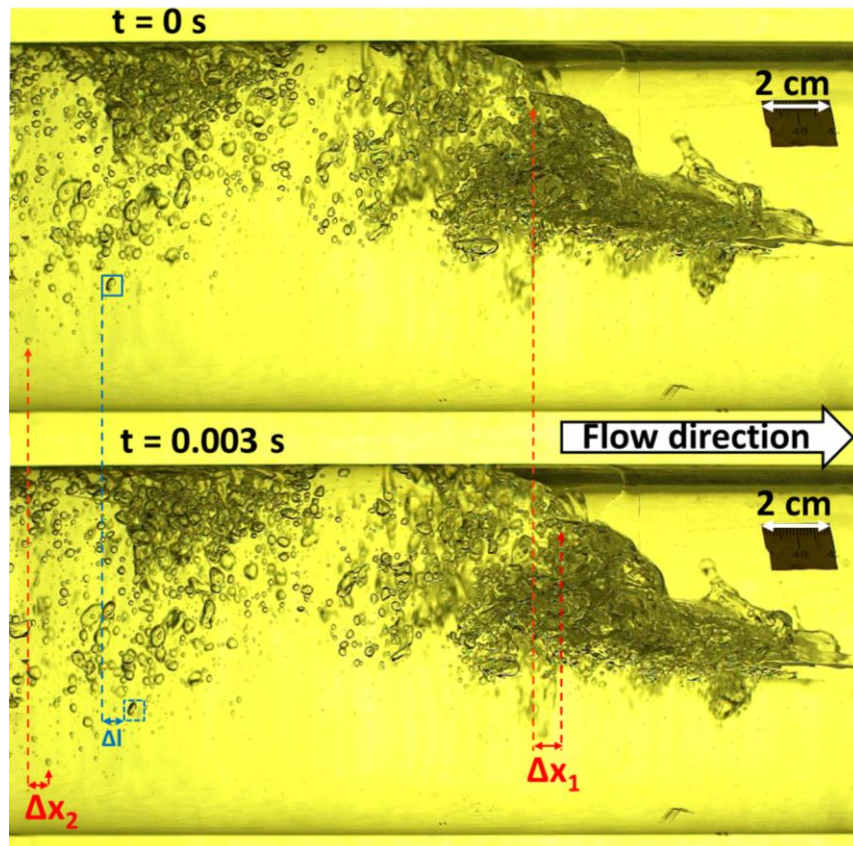


Figure 5-15: Illustration of calculating the in situ liquid velocities in a slug body. Time difference between frames  $\Delta t = 0.003$  s.  $V_{sl}=1.0$  m/s,  $V_{sg}=0.6$  m/s.

The horizontal movements of the tracers were measured automatically using a cross correlation method with an in-house computer program. The computer algorithm is illustrated in Figure 5-16. Two video frames with a small time separation ( $\Delta t$ ) are displayed. Each video frame is a two-dimensional (x-y) array of pixels, which can be quantitatively represented by grayscale values ranging from 0 to 255. A grayscale value of 0 represents most black while 255 represents most white. In the video frame at  $t = 0$  s, a tracer, where the velocity was to be calculated, was defined by the matrix **A** ( $i \times j$  pixels). The coordinates of matrix **A** in the frame is also calculated. Subsequently, a matrix **B**

( $i \times j$  pixels) with the original coordinates of matrix **A** was located in the succeeding frame ( $t = \Delta t$  s). To compare the strength of correlation between two data series of grayscale values in matrix **A** and matrix **B**, the Pearson product-moment correlation coefficient ( $r$ ) [81] was used:

$$r = \frac{\sum_i \sum_j (A_{i,j} - \bar{A})(B_{i,j} - \bar{B})}{\sqrt{\sum_i \sum_j (A_{i,j} - \bar{A})^2 \sum_i \sum_j (B_{i,j} - \bar{B})^2}} \quad (5-13)$$

where  $A_{i,j}$  and  $B_{i,j}$  are the grayscale values of the individual pixel in matrix **A** and **B**;  $\bar{A}$  and  $\bar{B}$  are the mean grayscale values of matrix **A** and **B**, respectively. The  $r$  value ranges from -1 to 1, where 1 is maximum positive correlation, -1 is maximum negative correlation, and 0 is no correlation.

The correlation coefficient ( $r$ ) value between **A** and **B** was calculated and recorded. The matrix **B** was then through an  $n$ -step horizontal movement to the right of the frame (flow direction). For each step, matrix **B** shifted its  $x$ -coordinate with one pixel unit to form a new pixel matrix of the same size, which was compared to the original matrix **A** to calculate the correlation coefficient. Assuming that there was no vertical drift or deformation of the tracer, the moving matrix **B** containing the same tracer should be captured at several steps downstream of the flow ( $x$  direction) in the succeeding frame, with the maximum correlation coefficient value. The horizontal movement ( $\Delta l$ ) of the matrix **B** during this time period ( $\Delta t$ ) was then calculated using the 2-cm scale reference as shown in the images (Figure 5-15), and the tracer velocity was then calculated as  $\Delta l / \Delta t$ . To illustrate this computational calculation by an example, a gas bubble within a pixel matrix marked by a blue rectangle in the frame at  $t = 0$  s was chosen as the tracer

(Figure 5-15). The grayscale representation of this matrix **A** ( $25 \times 25$  pixels) is shown in Figure 5-17A. The correlation coefficients between matrix **A** and the moving matrix **B** ( $25 \times 25$  pixels) in the succeeding frame were calculated (shown in Figure 5-17B). It can be seen that a maximum correlation coefficient of 0.68 was obtained when the matrix **B** horizontally moved 26 pixel units. The equivalent velocity of the tracer was calculated to be 2.1 m/s. The corresponding matrix **B** in grayscale with the maximum correlation to matrix **A** was extracted, as shown in Figure 5-17C. When comparing Figure 5-17A and Figure 5-17C, it demonstrates that the cross correlation method effectively captured the tracer and, therefore, the calculated velocities should be deemed valid.

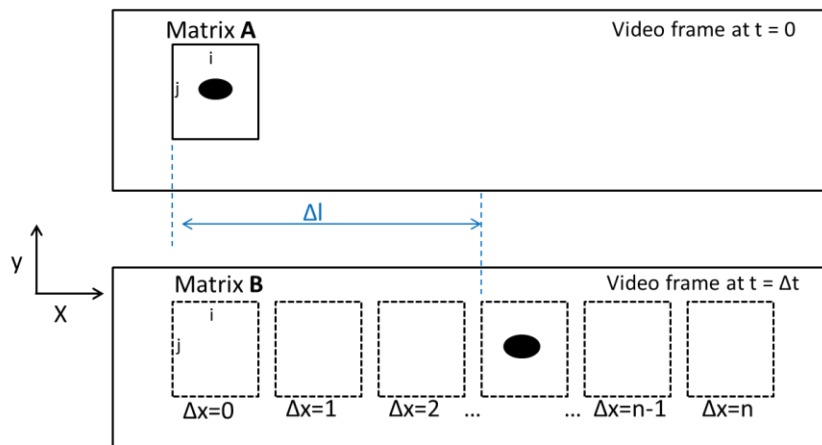


Figure 5-16: Illustration of tracking the tracer in the video frame at  $t = \Delta t$ .

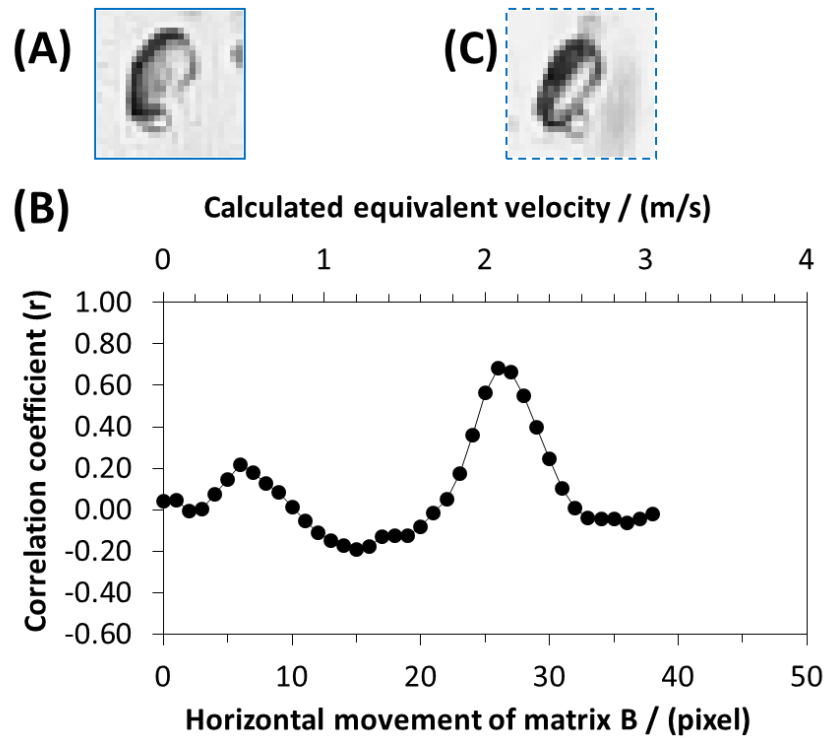


Figure 5-17: Illustration of tracking the tracer in two video frames using the cross correlation method. (A): the matrix **A** containing the tracer in grayscale at  $t = 0$  s (marked by blue rectangle in Figure 5-15); (B) the calculated correlation coefficients between the matrix **A** and the moving matrix **B**; (C) the moving matrix **B** with the maximum correlation to matrix **A** in grayscale at  $t = 0.003$  s.

Images of multiple slugs were analyzed for each flow condition and the maximum local velocities ( $V_{\max}$ ) at the top and bottom of the pipe were obtained (tabulated in Table 5-4), which are compared with the mixture velocity in Figure 5-18.

Table 5-4: Maximum local liquid velocity ( $V_{\max}$ ) calculated from the video data in the slug body, for 4 inch pipe loop

Location	$V_{sl}$ / (m/s)	$V_{sg}$ / (m/s)	$V_m$ / (m/s)	$V_{\max}$ / (m/s)
Bottom	0.1	0.2	0.3	0.7
Bottom	0.1	0.6	0.7	0.9
Bottom	0.1	2.6	2.7	3.3
Bottom	0.2	0.6	0.8	1.1
Bottom	0.2	2.6	2.8	3.0
Bottom	0.3	0.2	0.5	0.8
Bottom	0.3	0.6	0.9	1.1
Bottom	0.3	2.6	2.9	3.8
Bottom	1.0	0.6	1.6	1.8
Bottom	1.0	1.3	2.3	3.3
Bottom	1.0	2.1	3.1	3.7
Bottom	1.0	2.6	3.6	4.4
Bottom	1.0	5.0	6.0	5.2
Bottom	2.0	0.6	2.6	3.4
Bottom	2.0	1.3	3.3	4.4
Bottom	2.0	2.1	4.1	4.3
Bottom	2.0	2.6	4.6	4.7
Bottom	2.9	1.3	4.2	6.0
Bottom	2.9	2.1	5.0	5.9
Bottom	2.9	2.6	5.5	6.0
Bottom	2.9	5.0	7.9	8.9
Top	0.1	0.6	0.7	2.8
Top	0.1	2.6	2.7	5.5
Top	0.2	2.6	2.8	5.5
Top	0.3	0.6	0.9	2.7
Top	0.3	2.6	2.9	6.7
Top	1.0	2.6	3.6	7.6
Top	1.0	5.0	6.0	10.5
Top	2.0	2.6	4.6	8.6
Top	2.0	5.0	7.0	11.1
Top	2.9	2.6	5.5	9.3
Top	2.9	5.0	7.9	12.3

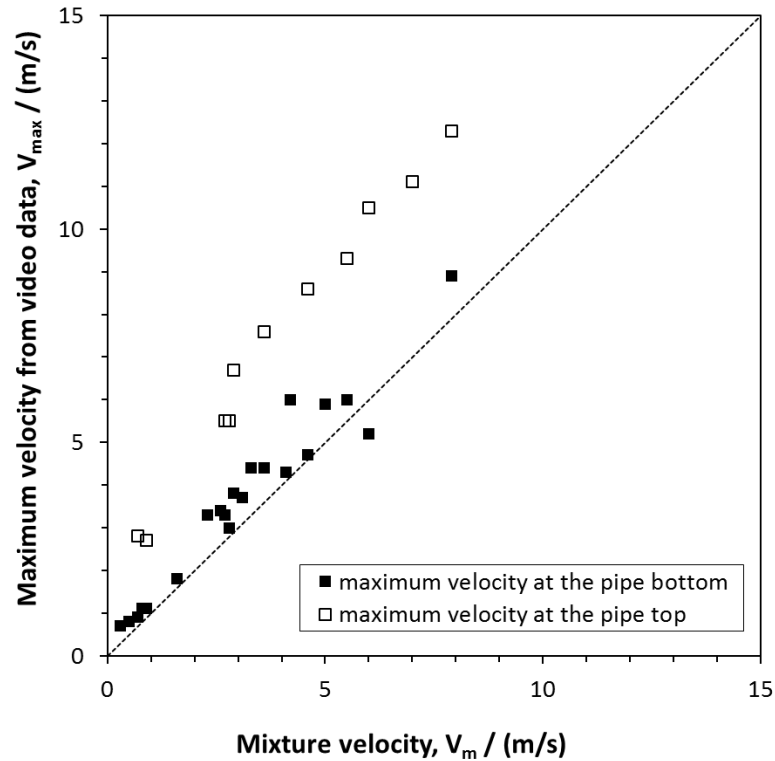


Figure 5-18: Comparison between maximum local liquid velocity ( $V_{max}$ ) in the slug body calculated from the video data and the mixture velocity ( $V_m$ ) at each flow condition, for 4 inch pipe loop.

The comparison in Figure 5-18 shows that the measured maximum liquid velocity at the bottom of the pipe is similar or slightly higher than the mixture velocity (by approximately 10%) while this maximum velocity at the top is significantly higher than the mixture velocity (by approximately 70%). As the cross-sectional average velocity in the slug body must be equal to the mixture velocity, this implies that sections of the fluid in the slug must be moving slower than the mixture velocity. Unfortunately, it was impossible to obtain the complete velocity profile from the existing video data due to the difficulties of tracking small individual gas bubbles.

Using the local maximum flow velocities ( $V_{\max}$ ) instead of the mixture velocities ( $V_m$ ) as the slug body velocity ( $V_s$ ), the maximum WSS was calculated from Equation (5-12) and compared to the measured maximum WSS value (Figure 5-19). The agreement between them demonstrates that the local wall shear stress along the pipe periphery in the slug body can be calculated with a reasonable accuracy from Equation (5-12) using the true local flow velocity.

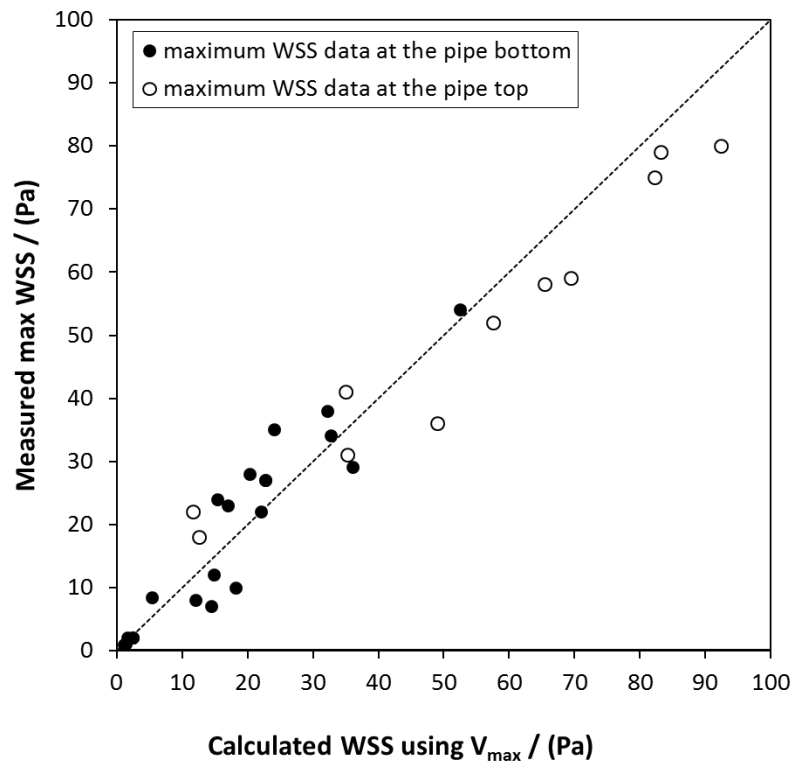


Figure 5-19: Comparison between measured maximum WSS values and calculated maximum slug WSS values from Equation (5-12) by using  $V_{\max}$  from the video data, for 4 inch pipe loop.

The WSS measurements in slug flow indicated that the flow velocity profile in the liquid slug body was highly non-uniform. The highest WSS occurred on the top of the

pipe when the slug front passed with the maximum in situ flow velocity. The maximum WSS value was about 2 to 4 times higher than the calculated mean WSS value from empirical correlations when using the mixture velocity; this may serve as a guideline for operations involving slug flow and for slug modeling with applications to other areas, such as removal of corrosion inhibitor films and corrosion product layers.

#### *5.4.2 Assessment of the location with the highest wall shear stress in a slug*

In order to investigate the relationship between WSS measurements and flow patterns, a synchronized high speed camera was used in tandem with the shear stress probe. This was to assess which part of the liquid slug body would generate the highest WSS. Figure 5-20 shows flow visualization frames of passing slug bodies corresponding to the WSS peak values that occur at 35.52 s, 35.99 s, and 36.54 s, as marked in Figure 5-8(B), respectively. In the images the WSS probe was masked by the black opaque probe holder and was flush mounted to the bottom pipe wall (at location “1” in Figure 5-20; also see Figure 4-4). A 2 cm tape was attached to the front pipe wall as a length scale reference (marked as “2” in Figure 5-20). In this specific flow condition, for the peaks at 35.52 s and 35.99 s, the highest bottom WSS value was recorded at exactly the same time when the slug front passed the WSS probe. However, for the peak at 36.54 s, the highest WSS was measured in the middle of the slug body. Considering all flow conditions documented by direct WSS measurement and high speed video recordings, no clear correlation was observed between the maximum WSS and a specific location in the slug body when the probe was at the bottom of the pipe. This can be explained by the

difference between individual slugs in the 4-inch loop having different characteristics for the bottom.

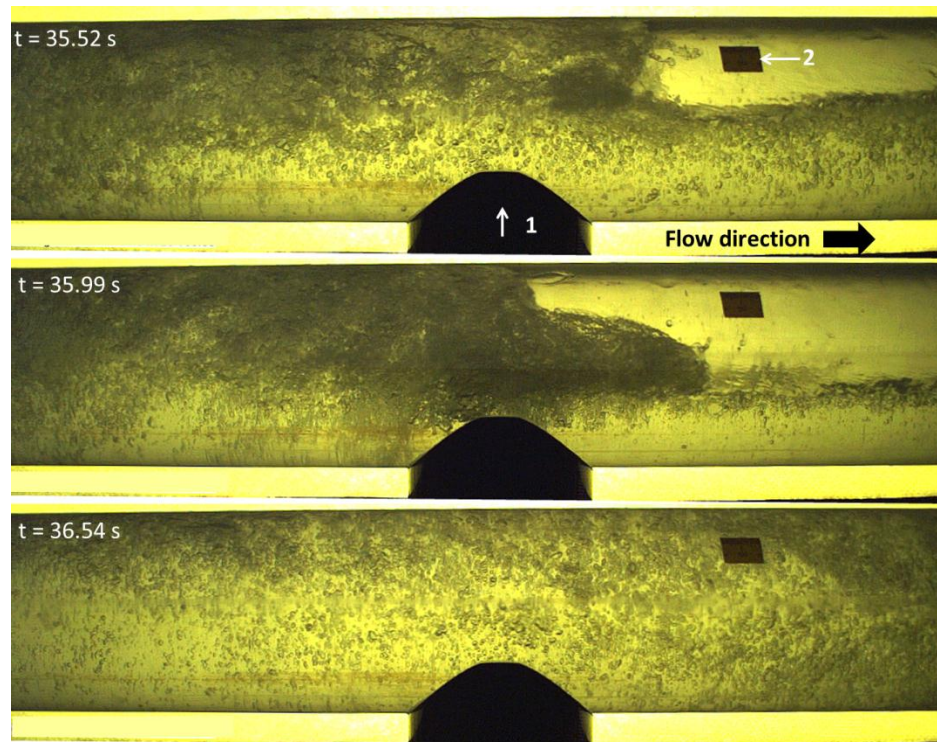


Figure 5-20: Video frames of slug passages corresponding to the three WSS measurement peaks marked in Figure 5-8(B),  $V_{sl} = 2.0$  m/s,  $V_{sg} = 2.1$  m/s: 1. the WSS probe is at the pipe bottom; 2. a scale tape of 2 cm long.

When the probe was at the top of the pipe, a clear correlation between the highest WSS and the passage of the slug front was observed. To demonstrate the WSS fluctuations during a slug passage, Figure 5-21 shows the WSS evolution with synchronized video frames of the slug at 74.29 s as marked in Figure 5-9(B). The passage of this slug was clearly recorded by the WSS fluctuations. The highest WSS occurred when the slug front passed the probe.

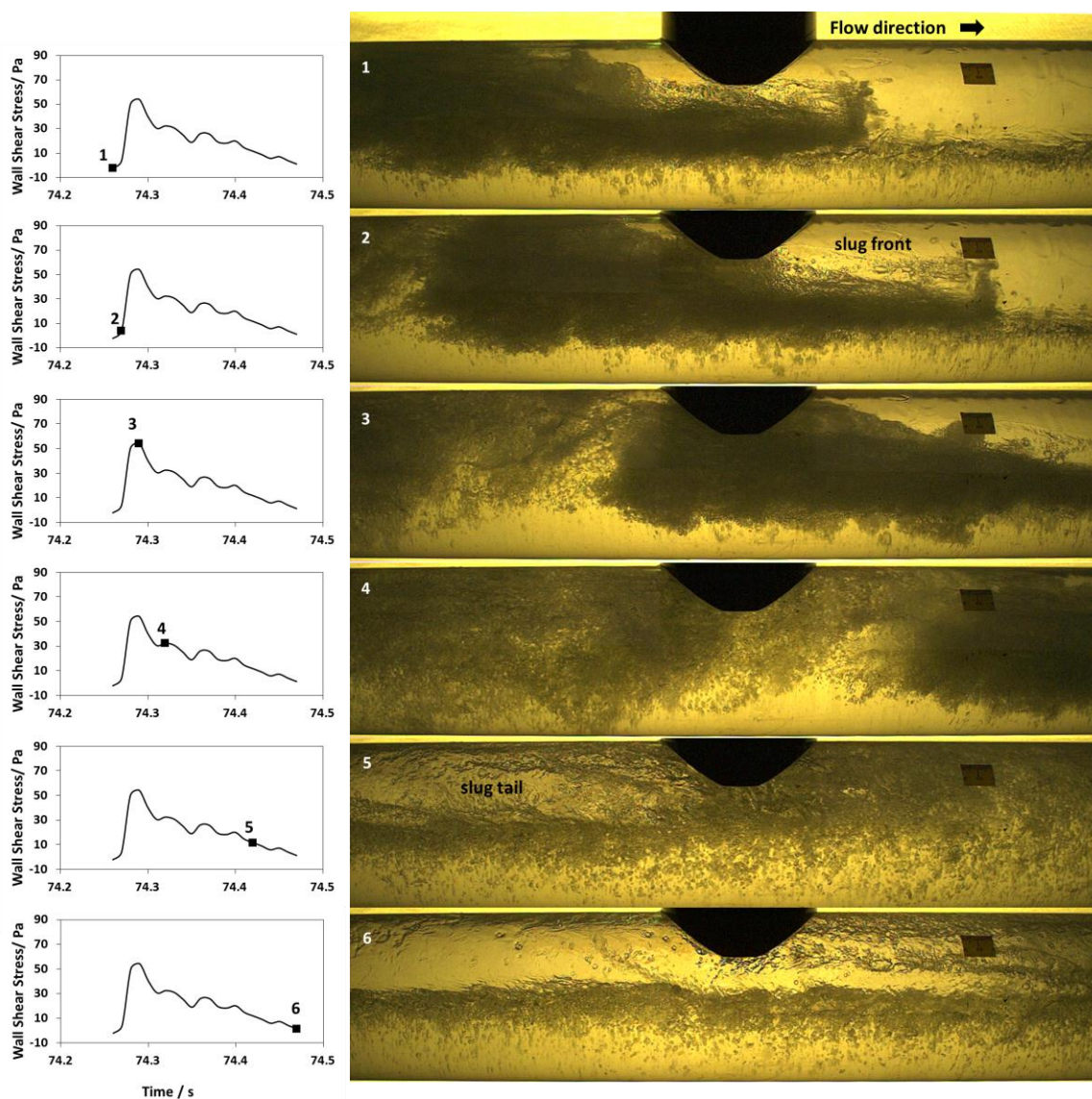


Figure 5-21: Evolution of the WSS fluctuations with synchronized video frames of the slug around 74.29 s marked in Figure 5-9(B),  $V_{sl} = 2.0$  m/s,  $V_{sg} = 2.6$  m/s, 4 inch pipe.

Figure 5-22 shows flow image frames corresponding to the three consecutive WSS peaks shown in Figure 5-9(B). In this condition, the WSS peak values were always recorded at a time shortly after the slug fronts passed the WSS probe. This observation was repeatable and consistent for all slugs. This finding confirms that the slug front generates the highest WSS at the top of the pipe irrespective of flow condition.

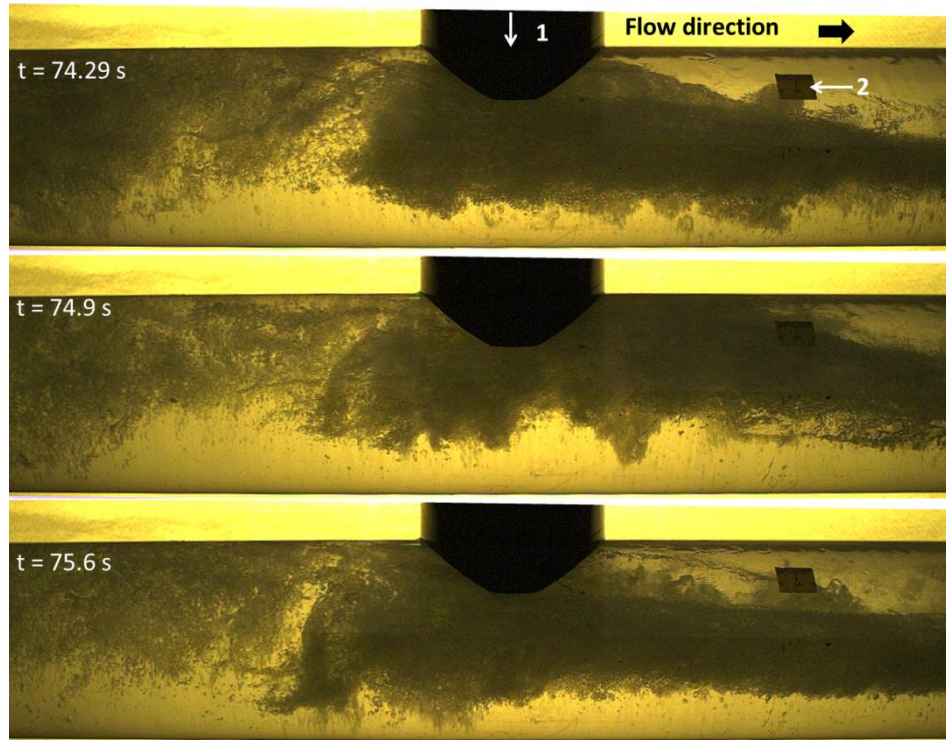


Figure 5-22: Video frames of slug passages corresponding to the three WSS measurement peaks marked in Figure 5-9(B),  $V_{sl} = 2.0$  m/s,  $V_{sg} = 2.6$  m/s: 1. the WSS probe is at the pipe top; 2. a scale tape of 2 cm long.

#### 5.4.3 Determination of slug frequency

Slug frequency (slugs/second) is an important parameter as it is one of the required closure relationships in many slug flow models [62]. In this research, the slug frequency was determined from two sources, from analyzing the high speed video recordings and the WSS data. From the video data, the slug frequency was obtained by visually counting the number of slugs per unit of time. From the WSS data taken at the top of the pipe, the slug frequency was determined by counting the WSS peaks per unit of time. For example, in Figure 5-9(B), there are approximately 22 peaks within a 10 s period, which results in a slug frequency of 2.2 Hz. The measured slug frequencies are plotted in Figure 5-23.

Both methods should and did give almost the same results. The slug frequency increases with increasing superficial liquid velocity, and slightly decreases with increasing superficial gas velocity. The measured slug frequencies were compared with the data of Heywood and Richardson at similar flow conditions in a 42 mm ID (1.65 inch) pipe [82], as shown in Figure 5-23. The results are coherent for these two sets of data despite the fact they were obtained in different pipe diameter systems. Existing literature reports that a minimum slug frequency exists as a function of  $V_{sg}$  for a given  $V_{sl}$  [82–84]. Gregory and Scott reported slug frequency data with a  $V_{sl}$  up to 1.3 m/s, and found the minima occurred at a slug translational velocity of approximately 6 m/s for each  $V_{sl}$  [84]. Woods et al. [83] found the minimum slug frequency to be at approximately  $V_{sg} = 4$  m/s in a 0.095 m ID pipe for data with  $V_{sl}$  up to 1.2 m/s. In the present study no clear minimum was observed, which may be due to the narrow gas velocity range (up to 5 m/s).

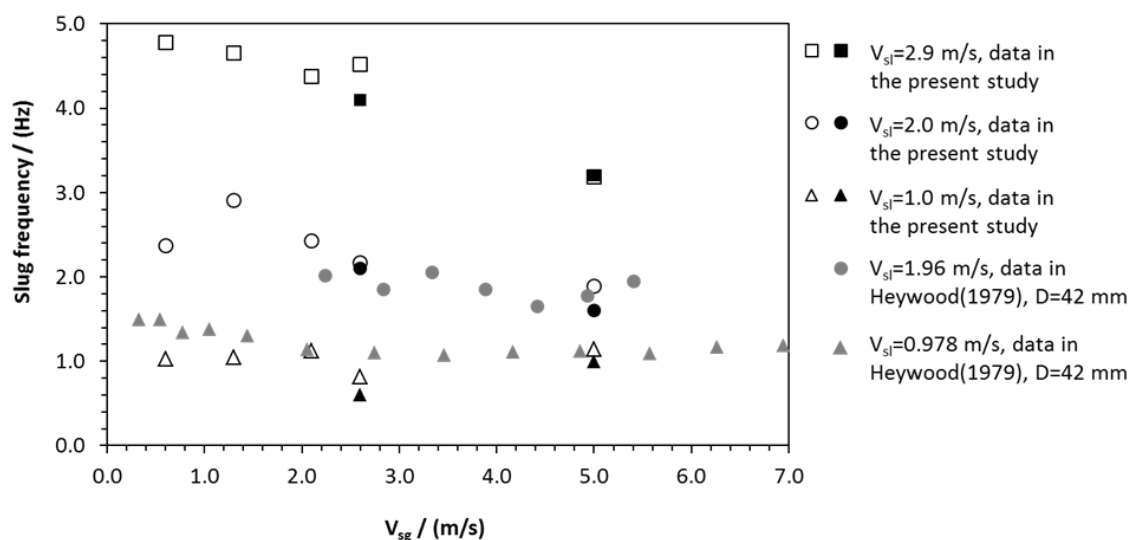


Figure 5-23: Comparison of measured slug frequencies by different methods (video data: hollow markers; WSS data: solid black markers) with the data of Heywood and Richardson (1979) [82] (solid gray markers).

Slug frequency is often calculated using empirical correlations [82,84,85]. Although mechanistic models have been developed [86], they are not widely used in practice due to their complexity and numerical challenges, e.g., lack of computational power [85]. The experimental data in this study were compared with several published empirical correlations as given in Table 5-5.

Table 5-5: Selected empirical correlations for slug frequency determination [82,84,85]

---


$$\text{Heywood et al. (1979)} \quad f_s = 0.0434 \left[ \frac{V_{sl}}{V_m} \left( \frac{2.02}{D} + \frac{V_m^2}{gD} \right) \right]^{1.02} \quad (5-14)$$

$$\text{Gregory et al. (1969)} \quad f_s = 0.0226 \left[ \frac{V_{sl}}{gD} \left( \frac{19.75}{V_m} + V_m \right) \right]^{1.2} \quad (5-15)$$

$$\text{Zabaras (2000)} \quad f_s = 0.0226 \left( \frac{V_{sl}}{gD} \right)^{1.2} \left[ \frac{212.6}{V_m} + V_m \right]^{1.2} [0.836 + 2.75 \sin^{0.25}(\alpha)] \quad (5-16)$$


---

where  $f_s$  is the slug frequency (Hz),  $V_{sl}$  is the superficial liquid velocity,  $V_m$  is the mixture velocity,  $D$  is pipe diameter,  $g$  is gravitational acceleration and  $\alpha$  is pipe inclination angle; it should be noted that the Heywood correlation (1979) and the Gregory correlation (1969) are given in SI units, while the Zabaras correlation (2000) is written in English units with  $f_s$  in Hz,  $V_m$  and  $V_{sl}$  in ft/s,  $D$  in ft,  $\alpha$  in degree and  $g$  in ft/s<sup>2</sup>.

The statistics related to the differences between the measured values and those predicted by the correlations are listed in Table 5-6. As it turns out, none of the predictions was satisfactory. The slug frequencies predicted by all correlations were significantly lower than the measured values. Figure 5-24(A) shows the comparison between the measured data and the Heywood correlation, where a significant discrepancy is found. When examining Equation (5-14), it shows that the slug frequency is dependent on the pipe diameter. However, it is noted that the Heywood correlation was originally derived from the data collected only in a 42 mm pipe, and the effect of pipe diameter on slug frequency was not studied. Therefore, the extension to different pipe diameters is not easily justified. When using a diameter of 42 mm in Equation (5-14) instead of 102 mm, better predictions were obtained, as shown in Figure 5-24(B). It can be seen that the predictions for data at  $V_{sl} = 2.9$  m/s remain unsatisfactory. This may be explained by the fact that this superficial liquid velocity was considerably higher than the ones originally used to derive the correlation [82].

Table 5-6: Error statistics for slug frequency: (predicted – measured)/measured,  
for the data produced by using different empirical correlations

Correlations	Heywood et al. (1979)	Gregory et al. (1969)	Zabaras (2000)
Average error (%)	-59.3	-64.9	-70.7
Standard deviation (%)	12.0	9.2	7.7
Average absolute error (%)	59.3	64.9	70.7
Standard deviation of absolute error (%)	12.0	9.2	7.7

Overall, the results suggest that empirical correlations derived from a limited number of data in a specific test setup may not be reliable when applying them to systems where flow conditions (e.g., velocities, pipe diameters) are outside the original data set range. In addition, all existing empirical correlations may suffer to some degree from laboratory loop artefacts as the slug frequency in many laboratory facilities may be influenced by factors such as the inlet geometry, upstream details (e.g., presence of a gas buffer) and the length of the loop. Mechanistic approaches such as that given by, for example, the Taitel and Dukler model [86] are therefore recommended for accurate slug frequency predictions, even if these are much more complicated to implement [85].

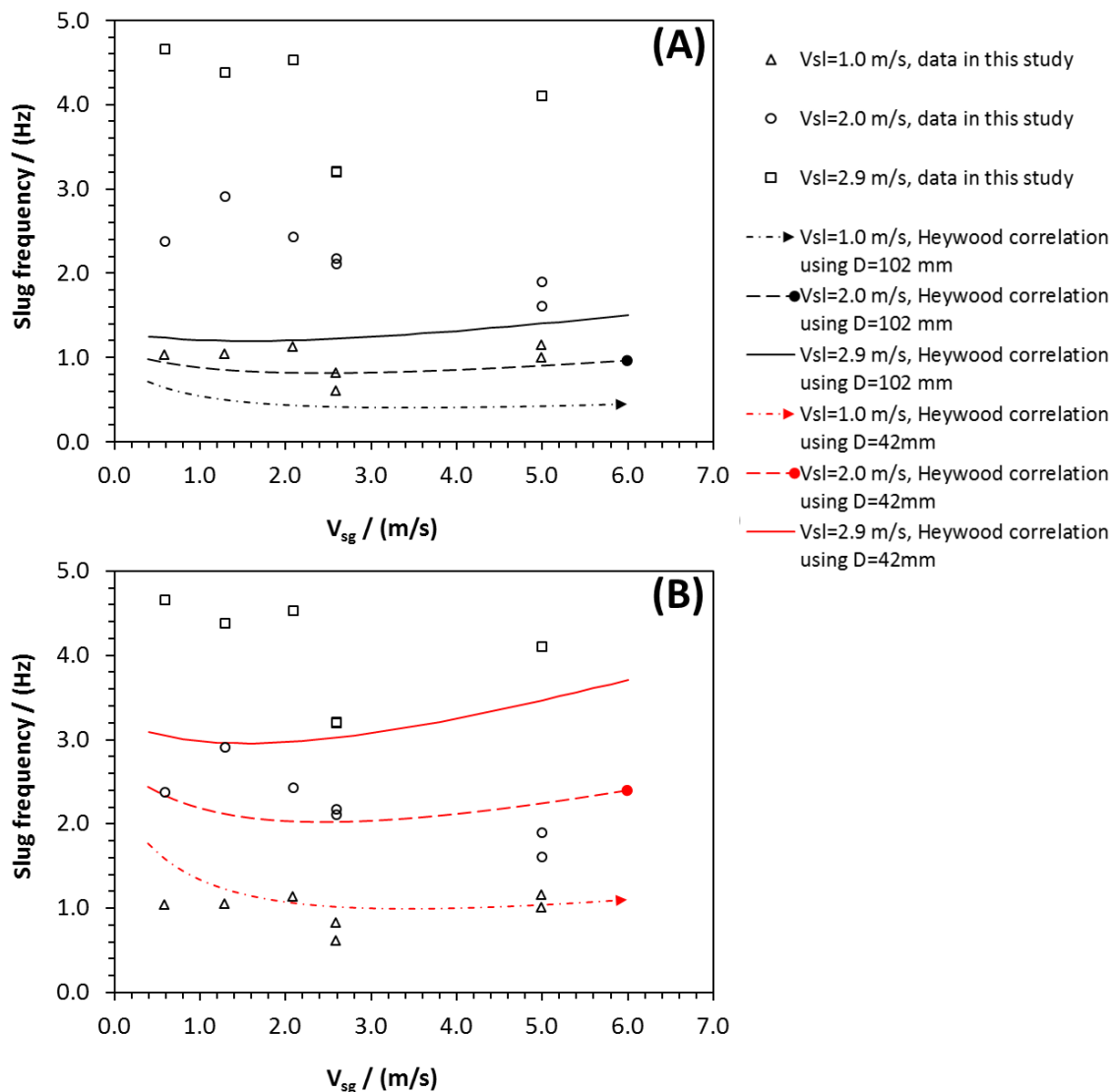


Figure 5-24: Comparison of measured slug frequencies with the Heywood correlation: (A) using the pipe diameter of this study; (B) using the pipe diameter of 42 mm.

#### 5.4.4 Wall shear stress measurements in stratified flow and annular flow

A limited number of WSS measurements were taken for stratified flow and annular-dispersed flow. The characteristics of stratified flow were described in Figure 2-6. As the liquid and gas velocities are relatively low in this flow pattern, a low WSS is expected.

The WSS values measured for stratified flow in the 4-inch loop were only up to 3 Pa at the tested flow conditions. Figure 5-25 shows an example of the WSS pattern for stratified flow. The average value and fluctuations of the WSS were much smaller as compared to slug flow.

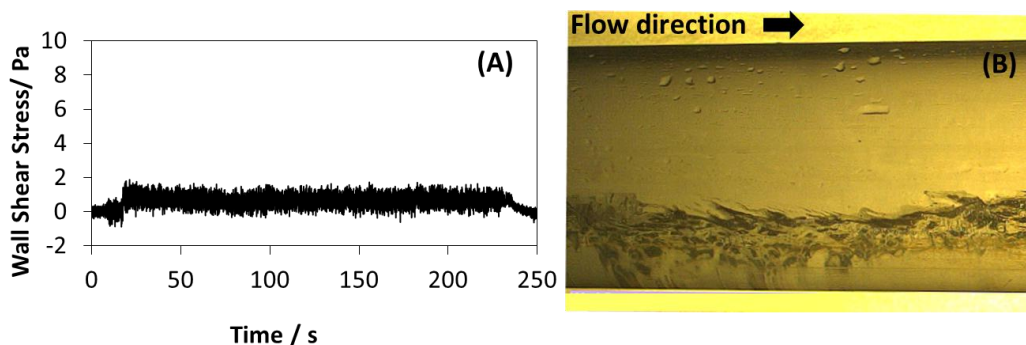


Figure 5-25: Wall shear stress measurement at the bottom of the 4 inch pipe for stratified flow at  $V_{sl} = 0.1$  m/s,  $V_{sg} = 6.1$  m/s: (A) the full recording sequence; (B) a typical video frame at this condition.

Hydrodynamic features of annular flow are displayed in Figure 2-6. WSS measurements for annular flow were conducted in the 6 inch ID pipe system (Figure 4-5). Figure 5-26(A) shows a typical WSS measurement for annular flow. A significant fluctuation of the WSS measurement can be seen at the beginning of the test (0 – 150 s), which was due to the fact that the superficial gas velocity slowly reached the designated 42.2 m/s by the gas blower. The steady annular flow measurement data (170 – 270 s) shows a similar pattern as that of stratified flow. A typical video image of annular flow is shown in Figure 5-26(B). It can be seen that a water layer is still present at the bottom of the pipe; a very thin water film is observed around the pipe periphery (the water wave patterns). The water droplets impacting the side of the pipe wall are also present.

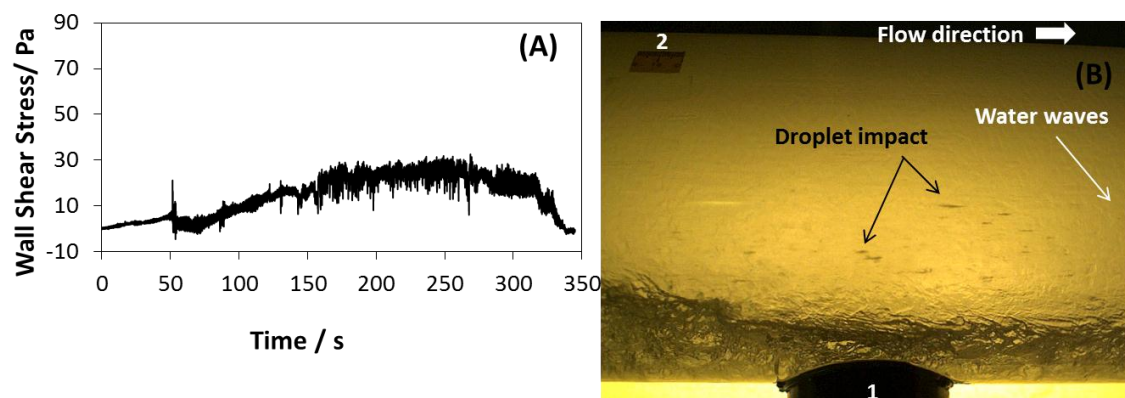


Figure 5-26: Wall shear stress measurement at the bottom of the 6 inch pipe for annular flow at  $V_{sl} = 0.2$  m/s,  $V_{sg} = 42.2$  m/s: (A) the full recording sequence; (B) a typical video frame at this condition (1: the WSS probe location; 2: a scale tape of 2 cm long).

The WSS was measured at the bottom and side of the 6 inch pipe at various flow conditions (see Figure 5-1), with the values given in Table 5-7. There was no measurable WSS at the top of the pipe at the tested conditions. The WSS values for the bottom and the side increased with increasing liquid superficial velocity. The WSS at the side wall was smaller than at the bottom of the pipe. This was mainly due to the much smaller thickness of the moving liquid film, and presumably smaller liquid velocities, for the side and top as compared to the bottom of the pipe.

Table 5-7: WSS data measured for annular flow at the bottom and  
on the side wall of the 6 inch pipe

Probe location	$V_{sl}$ / (m/s)	$V_{sg}$ / (m/s)	$V_m$ / (m/s)	Mean WSS / (Pa)	Max WSS / (Pa)
bottom	0.02	42.2	42.22	8	14
bottom	0.1	42.2	42.3	13	19
bottom	0.2	42.2	42.4	25	32
side	0.02	42.2	42.22	0.5	4
side	0.1	42.2	42.3	2	9
side	0.2	42.2	42.4	3	9

### 5.5 Discussion

In this research project, two-phase flow patterns such as slug flow, stratified flow and annular flow were investigated, and the highest WSS recorded was approximately 100 Pa. These high values were recorded for slug flow at the top of the pipe when each slug front passed. Measured WSS values were in agreement with empirical WSS correlations when using the correct local velocities in the two-phase flow field. This suggests that proper resolution of the flow field, obtained either from computational fluid dynamics or by experimentation, would allow for better evaluation of WSS.

In laboratory environments, inhibitors are often subjected to high flow velocity tests with calculated shear stresses of the order of  $10^3$  Pa [17,87] to assess their performance in extreme flow conditions. In the present research conducted in single-phase channel flow, the measured shear stresses reached the same magnitude of  $10^3$  Pa when the liquid velocity was extremely high (17 m/s), but for the measured two-phase slug flow with the mixture velocity up to 7.9 m/s, the highest WSS values were one order of magnitude lower. When using Equation (5-12) as a reference to calculate the WSS of slug flow under possible flow conditions, it was found that the maximum value did not exceed

1000 Pa with mixture velocities up to 30 m/s and gas densities up to  $100 \text{ kg/m}^3$  in a 4-inch-ID pipe. This suggests that the maximum WSS in realistic multiphase pipe flow under most extreme conditions would be of the order of  $10^3$  Pa.

Recalling the fact that the stresses required to remove inhibitor films and/or  $\text{FeCO}_3$  layers are at least  $10^6$  Pa in magnitude [9,11,19,22], there is a large gap between the required stresses to remove these films/layers and flow shear stresses measured or expected in practice. It may therefore be concluded that the high values of WSS found in multiphase flow cannot lead to purely mechanical removal of inhibitor films and protective corrosion product layers.

Although the floating element probe was used to successfully measure the WSS in the multiphase flow, some possible shortcomings in the present research program have been identified and are discussed below. The spatial and temporal resolutions of the WSS probe do not allow measurement of very short-lived WSS values (fluctuations) occurring over very small length scales.

The floating element on the WSS probe has a diameter of 6 mm, which still can be much larger than the scale of some turbulent eddies. The smallest hydrodynamic scale in turbulent flow can be estimated by the Kolmogorov length scale ( $\eta$ ), which is approximately of the order of 10 - 100  $\mu\text{m}$  in laboratory environments such as the one used here [88,89]. Therefore, to accurately measure local WSS from small turbulent eddies, a floating element with spatial dimensions of the order of 10-100  $\mu\text{m}$  may be necessary. The time scales associated with the smallest of eddies are of the order of ms, or even less, putting an additional requirement on the temporal resolution of the

measurements. On the other hand, the energy levels associated with the smallest eddies are also very low and it is not expected that they can contribute to a significant increase of the time/space averaged WSS, such as the one measured here.

Using the highest recording rate of 1000 Hz, the WSS probe provided reasonable measurements when it comes to the large time scale transients found in multiphase flows, such as, for example, during slugging. For instance, the slug frequency was only a few hertz, and any WSS fluctuations due to the passage of slugs would have been accurately recorded by the floating element probe.

While a number of different multiphase flow patterns were investigated in the present work, it is believed that some specific flow conditions found in the field, involving a discrete phase, were not covered by our testing. A good example is liquid droplet impingement found in annular-mist flow which may lead to much larger fluctuations of the WSS magnitude than recorded in the present study. Annular-mist flow with entrained liquid droplets, traveling at the gas velocity, can lead to high energy wall impacts particularly at locations of disturbed flow, such as bends, valves, tees, weld beads, etc. Very high local WSS and normal stresses could be found at impact locations [90], particularly when there is little “cushioning” by an existing liquid film. Laboratory tests have shown droplets having sizes of the order of 100  $\mu\text{m}$  [91], which would produce very short lived, high energy fluctuations at impact time. Therefore, a WSS probe would be required to have both high temporal and spatial resolutions in order to capture this behavior. This is an area that needs to be covered by future research.

## 5.6 Summary

The summary of the key findings of the research described in this chapter is given below:

- The floating element method was successful in directly measuring wall shear stress in the studied multiphase flow, which provides valuable data for mechanistic modeling.
- The highest wall shear stress in horizontal slug flow occurred on the top section of the pipe when the slug front passed. The higher wall shear stress as compared to the bottom was because of the higher local in situ liquid flow velocity. The maximum shear stress value was about 2 to 4 times higher than the calculated mean shear stress of the slug body using mixture velocity, which can serve as a guideline for improving slug flow modeling. When the correct local velocity is used, the calculations of the wall shear stress were in good agreement with the measured values.
- In multiphase flow, studied here at ambient conditions, the maximum wall shear stress was of an order of  $10^2$  Pa, obtained in slug flow. Using a model it was estimated that the highest practical wall shear stress that could be expected in the field is of the order of  $10^3$  Pa.
- This suggests that purely mechanical removal of inhibitor films or  $\text{FeCO}_3$  layers solely by wall shear stress, typically seen in multiphase flow pipelines, is very unlikely. As failures of these protective films/layers in multiphase flow are

observed in laboratory and field studies, other factors associated with multiphase flow must be considered.

## Chapter 6: Mechanical Effects of Flow on CO<sub>2</sub> Corrosion Inhibition

### 6.1 Introduction

In the previous chapter, it is found that the measured WSS in typical multiphase flow pipelines is several orders of magnitude lower than the required stresses to remove inhibitor films or corrosion product layers from the steel surface. Purely mechanical removal of these films/layers solely by WSS is therefore very unlikely. In this chapter, the hypothesis that surface geometric irregularity can locally lead to high instantaneous hydrodynamic stresses and interfere with the corrosion inhibitor adsorption/desorption processes is examined. In addition, other factors that may affect corrosion inhibitor films, e.g., oxygen ingress, are studied. Last but not least, the mechanisms of how flow mechanically affects the corrosion inhibitors are discussed.

### 6.2 Experimental

#### *6.2.1 Flow system for corrosion tests*

Experiments were performed in the earlier described thin channel flow cell system (Figure 4-2). Due to the high flow velocity in the thin channel, a high wall shear stress environment was expected. The flow generated by this system is considered to be the most turbulent that can be simulated in our laboratory and was used to investigate the mechanical integrity of TOFA/DETA imidazolinium inhibitor films in the presence of high mechanical stresses.

### 6.2.2 Corrosion specimens

Electrochemical measurements, weight loss, and surface analysis methods were used to determine the amount and type of corrosion that occurred during each experiment. Three different weight loss corrosion specimens and an electrochemical corrosion probe were used to measure corrosion. For the weight loss specimens, two cylindrical specimens and a cylindrical specimen with a protrusion on its top surface were used to study the surface roughness and the surface geometry effects. These specimens were all made of API\* 5L X65 carbon steel with the chemical composition given in Table 6-1, and were numbered as Specimen 1, Specimen 2 and Specimen 3 with respect to flow direction. Specimen 1 and Specimen 2 were of cylindrical shape with a diameter of 1.25 inch (3.18 cm) and 0.25 inch (0.64 cm) in height (as shown in Figure 6-1). Specimen 1 was sequentially polished with 400 and 600 grit sand papers, while Specimen 2 was sequentially polished with 400 and 150 grit sand papers. Except for the top surface, which was flush to the bottom plate of the flow cell and exposed to the corrosion environment, all other surfaces of the specimens were coated with corrosion resistant paint. Specimen 3 with a protrusion was sequentially polished with 400 and 600 grit sand paper. The specification and orientation of Specimen 3 with respect to the flow direction are shown in Figure 6-2. This specimen had a trapezoidal-prism-shaped protrusion on top of the cylindrical base. While the cylindrical base was flush to the bottom plate of the flow cell, the trapezoidal prism protruded out of the bottom plate into the flow cell, similar as a weld bead may do in a real pipeline. Similar to cylindrical specimens, all

---

\* American Petroleum Institute

other surfaces of the specimen below the bottom plate of the flow cell were coated with corrosion resistant paint. The top surface of the protrusion specimen exposed to the corrosion environment was defined by 5 individual regions as shown in Figure 6-2 for surface analysis.

Table 6-1: Chemical analysis [wt.%] of API 5L X65 carbon steel

C	Mn	Nb	P	S	Ti	V	Fe
0.05	1.51	0.03	0.004	0.001	0.01	0.04	balance

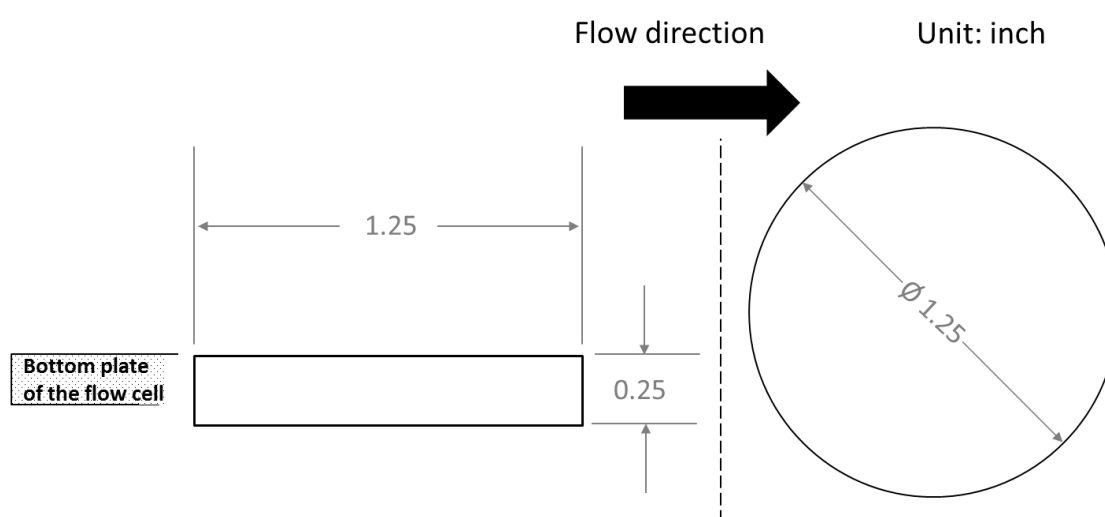


Figure 6-1: Specification and flow orientation for flat weight loss specimens. Left: side view; right: top view.

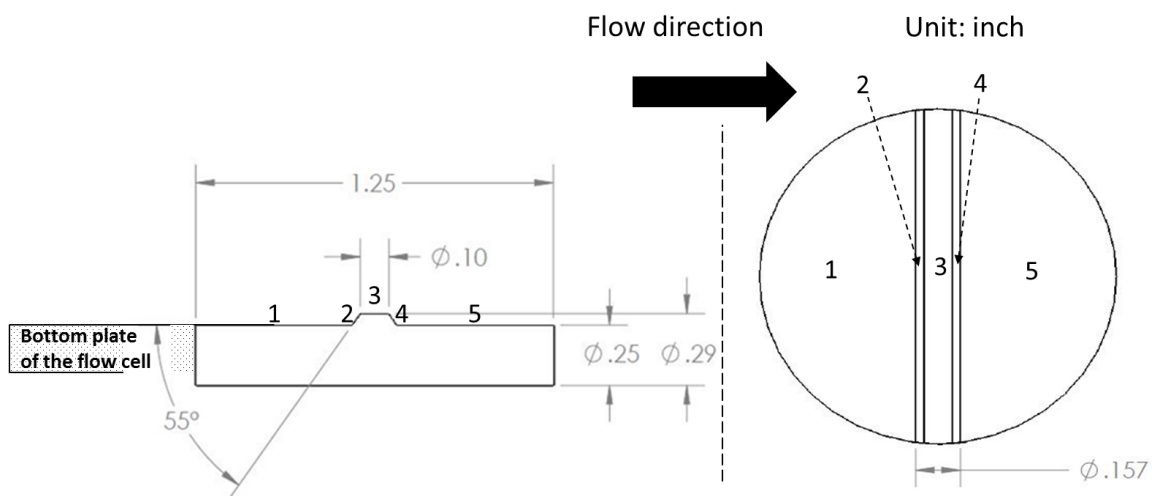


Figure 6-2: Specification and flow orientation of Specimen 3, protrusion weight loss specimen: left: side view; right: top view.

A three-electrode cylindrical electrochemical probe was employed for online electrochemical measurements during the test. As shown in Figure 6-3, the ring shaped working electrode (WE) was made of the same API 5L X65 carbon steel with a surface area of  $0.85 \text{ cm}^2$ . The outer body of the electrochemical probe, which is made of AISI<sup>†</sup> 316L stainless steel, was used as the counter electrode (CE). The surface of the electrochemical probe was sequentially polished by 400 grit and 600 grit sand papers prior to tests. An Ag/AgCl reference electrode (RE) was installed in the pipeline downstream of the test section to provide a stable and accurate potential for electrochemical measurements. Before each test, the reference electrode was calibrated with a standard saturated calomel electrode to ensure a correct potential reading.

---

<sup>†</sup> American Iron and Steel Institute

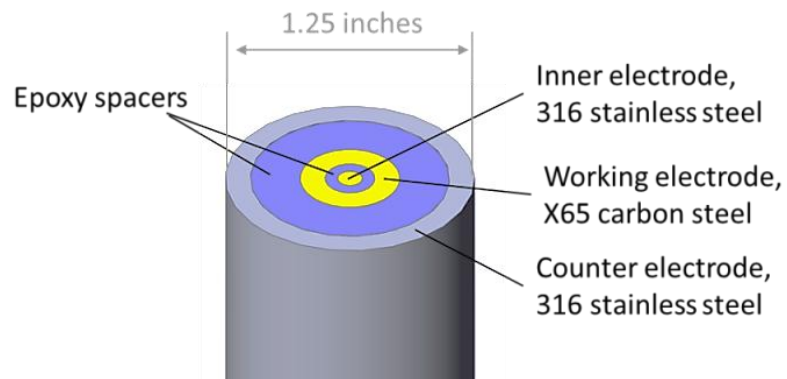


Figure 6-3: Configuration of the electrochemical probe.

The three weight loss specimens and the electrochemical probe were flush-mounted to the bottom plate in the TCFC test section in a sequence as shown in Figure 6-4. All weight loss specimens were fixed in position by using a mechanical specimen holder underneath (as shown in Figure 6-4). The protrusion specimen (Specimen 3) was placed furthest downstream (port 4) to minimize the flow disturbance to other specimens.

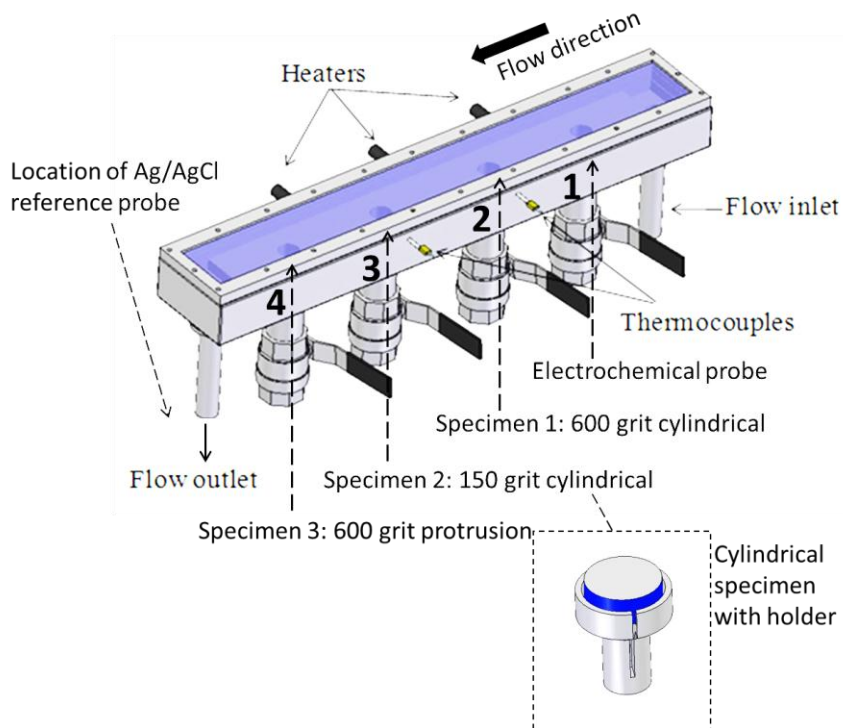


Figure 6-4: Location arrangement of the specimens in the TCFC.

### 6.2.3 Experimental procedures

The test matrix for this work is shown in Table 6-2. The tests were maintained at 25°C, 0.97 bar CO<sub>2</sub> partial pressure and a pH value of 5.0 to achieve a low FeCO<sub>3</sub> saturation value ( $S_{\text{FeCO}_3} \ll 1$ ) [6]. Accordingly, no FeCO<sub>3</sub> was expected or observed on the specimen surfaces in any of the following experiments, which was confirmed by SEM analysis. The inhibitor used was TOFA/DETA imidazolinium (K1).

Table 6-2: Test matrix for corrosion inhibition test with high flow velocity

Corrosion specimen material	X65 carbon steel
Temperature	25 ± 2°C
Total pressure	1 bar
Liquid phase	1 wt.% NaCl
Gas phase	0.97 bar CO <sub>2</sub>
Test pH	5.0 ± 0.2
Flow velocity	16 m/s
Test duration	4 days
Inhibitor concentration	0, 72, 720 ppm <sub>v</sub>
O <sub>2</sub> concentration	4 ppb <O <sub>2</sub> < 30 ppb, O <sub>2</sub> < 2 ppb

Preparation for each experiment was done using the following procedure. A 1 wt.% sodium chloride (NaCl) solution of 35 gallons (132 L) in volume was prepared with deionized (DI) water in the liquid tank of the TCFC, purged with a continuous CO<sub>2</sub> gas flow, and maintained at the test temperature of 25°C. The O<sub>2</sub> level of the system was monitored by an electrochemical O<sub>2</sub> sensor located at the purging outlet of the tank. The pressure in the tank for all tests was maintained at atmospheric pressure; and the CO<sub>2</sub> partial pressure was 0.97 bar due to the water vapor pressure of 0.03 bar at this temperature. The solution pH was adjusted to the required value by addition of sodium bicarbonate (NaHCO<sub>3</sub>), and was constantly monitored by a pH probe. After polishing, all specimens were cleaned in an ultrasonic bath with isopropanol ([CH<sub>3</sub>]<sub>2</sub>CHOH), dried by nitrogen gas and weighed to the nearest milligram. Surface analysis was conducted on each of the specimens prior to corrosion tests. The surface morphologies were

characterized by scanning electron microscopy (SEM) and profilometry. After surface analysis, all specimens were rinsed with isopropanol and flush-mounted to the bottom plate of the TCFC test section. The test section was then deaerated with dry CO<sub>2</sub> gas. Finally, the prepared test solution in the liquid tank was diverted to the test section at the designated flow velocity, pH, O<sub>2</sub> concentration and temperature.

During each experiment, a potentiostat connected with the electrochemical corrosion probe was used for performing electrochemical measurements. The open-circuit potential (OCP) was continuously monitored and linear polarization resistance (LPR) measurements were conducted systematically to provide in situ corrosion rate measurements. The potential polarization range was  $\pm 5$  mV versus OCP with a scanning rate of 0.1 mV/s. The solution resistance was measured with electrochemical impedance spectroscopy (EIS) to ensure satisfactory solution conductivity. Deaerated corrosion inhibitor was added to the system typically 10 – 12 hours after the beginning of the experiment when the corrosion rate was stable. Each experiment typically lasted another 4 days after the addition of inhibitor. In this work, a surfactant-type inhibitor, TOFA/DETA imidazolinium salt, was used. The molecular structure of this inhibitor is well understood, as depicted in Figure 2-5. A typical inhibitor concentration of 72 ppm<sub>v</sub> was used in the tests, which exceeded the reported CMC value for this inhibitor [22,92] and should effectively mitigate the corrosion at the tested temperature and pH [93,94].

After the corrosion test, all weight loss specimens were carefully taken out of the TCFC, immediately immersed into deaerated deionized water to remove soluble salts and impurities on the specimen surface. Sequentially, the specimens were cleaned in an

ultrasonic bath with isopropanol, dried by nitrogen gas, weighed to the nearest milligram, and stored in a vacuum desiccator for further after-test surface analyses.

### 6.3 Experimental Results

The focus of this work is to determine how mechanical stresses produced by turbulent flow affect corrosion inhibitor films. Wall shear stress (WSS) is one of the most important forms of hydrodynamic stresses to characterize flow conditions. In this study, the flow velocity in the TCFC test section was 16 m/s. The average WSS at the bottom plate of the TCFC was corroborated by measurements using a floating element WSS sensor (see Figure 5-2) to be approximately 700 - 800 Pa when the flow velocity was 16 m/s. But a special protrusion specimen was also used in this research, which was expected to significantly change the local hydrodynamic conditions, lead to a higher local WSS, and affect inhibitor films on the metal surface.

#### *6.3.1 Corrosion tests without inhibitor*

A blank test without addition of corrosion inhibitor was conducted, and the corrosion rates were measured by weight loss and LPR. The details of corrosion rate calculation by these two methods are described in Appendix 3. The weight losses from all three corrosion specimens were measured and the average corrosion rate was calculated to be  $5.7 \pm 0.4$  mm/yr.

The corrosion rate was also determined by the LPR technique, which measures the polarization resistance of the working electrode and calculates the corrosion current ( $I_{corr}$ ) by the Stern-Geary equation [57]:

$$I_{corr} = \frac{B}{R_p} \quad (6-1)$$

where  $R_p$  is the polarization resistance (ohm) and  $B$  is the proportionality constant, or  $B$  value (V). For corrosion of steel (iron), the calculated corrosion current is related to the corrosion rate, as given by:

$$CR = 1.16 \cdot \frac{I_{corr}}{S} \quad (6-2)$$

where  $CR$  is the corrosion rate (mm/yr);  $I_{corr}$  is the corrosion current (A); and  $S$  is the surface area of the electrode ( $m^2$ ). The overall formula of corrosion rate calculation can be written as:

$$CR = \frac{1.16B}{SR_p} \quad (6-3)$$

It should be noted that the  $B$  value is required to calculate the corrosion rate for the LPR technique, and quite often it is not known a priori.

The measured average corrosion rate from weight loss and polarization resistance from LPR were substituted in Equation (6-3) to determine the  $B$  value for the corrosion experiments in this study. Since the average corrosion rate from weight loss measurement was 5.7 mm/yr, the surface area of the electrode was  $0.85 \times 10^{-4} m^2$ , and the time-averaged polarization resistance from the LPR measurements was calculated to be 156 ohms, an averaged  $B$  value of 65 mV was obtained. This  $B$  value was used throughout the entire

series of experiments, which will be discussed later. The corrosion rate evolution over time for the blank test from LPR measurements is shown in Figure 6-5.

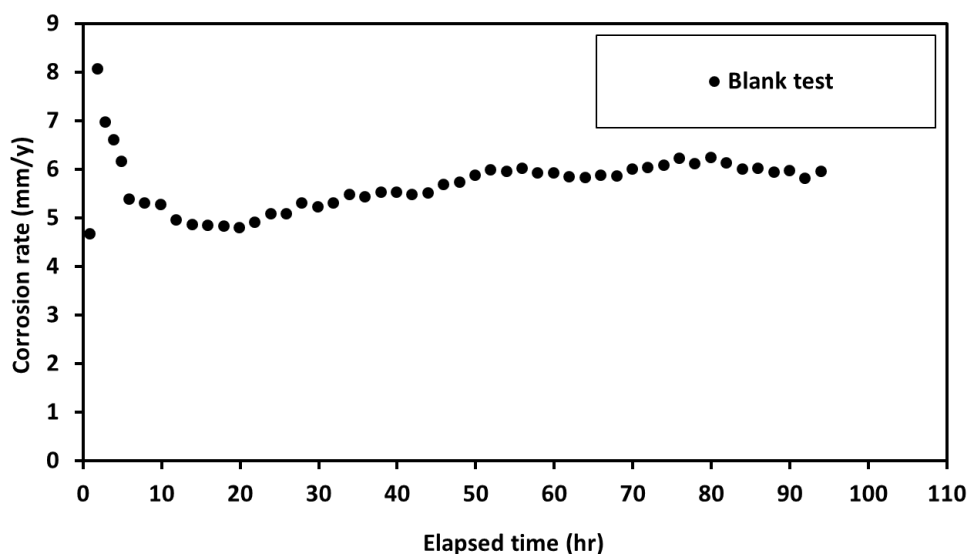


Figure 6-5: LPR corrosion rate for blank test,  $B = 65$  mV. 1 wt.% NaCl, pH 5, 0.97 bar  $\text{CO}_2$ , 25°C, 16 m/s, API 5L X65 carbon steel, 4 ppb to 30 ppb  $\text{O}_2$ .

The surface morphologies of all weight loss specimens were examined after the tests by SEM and profilometry. Figure 6-6 shows the gross morphology of the protrusion specimen examined by the profilometry after the experiment. Figure 6-7 shows the detailed surface morphologies of the protrusion specimen by SEM. Analysis of the protrusion specimen was defined using 5 numbered individual regions on the surface: 1 = upstream flat, 2 = upstream slope, 3 = top of protrusion, 4 = downstream slope, 5 = downstream flat. The surface analysis indicates a uniform corrosion occurred on the protrusion specimen. The surface morphologies for flat specimens showed a similar pattern as that seen for the protrusion specimen and are therefore not shown here.

The chemical composition of the specimens after the experiment was analyzed by EDS. The results for the three specimens were similar, which all suggested a uniformly corroded surface without formation of a protective CO<sub>2</sub> corrosion product layer (i.e., FeCO<sub>3</sub>), as demonstrated in Figure 6-8.

Generally, the observed high corrosion rate made the surface features of all specimens similar and no localized corrosion was observed.

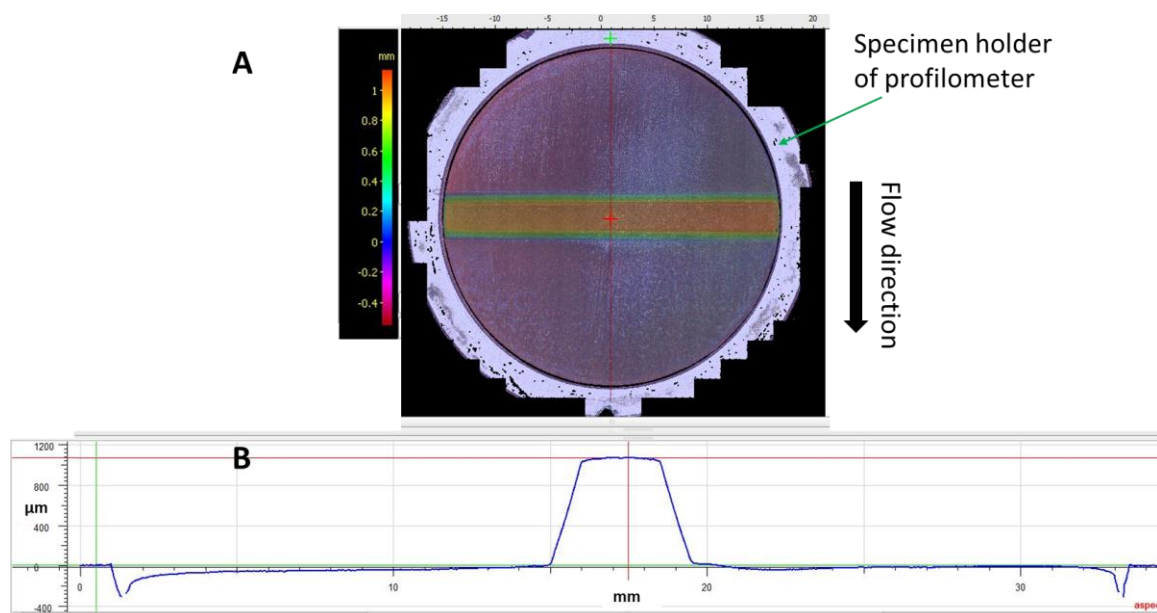


Figure 6-6: Profilometry results of protrusion Specimen 3 after the blank test. A: contour of the surface depth; B: line pattern depth scan of the surface marked by the red straight line in A. 1 wt.% NaCl, pH 5, 0.97 bar CO<sub>2</sub>, 25°C, 16 m/s, 4 day, X65, 4 ppb to 30 ppb O<sub>2</sub>.

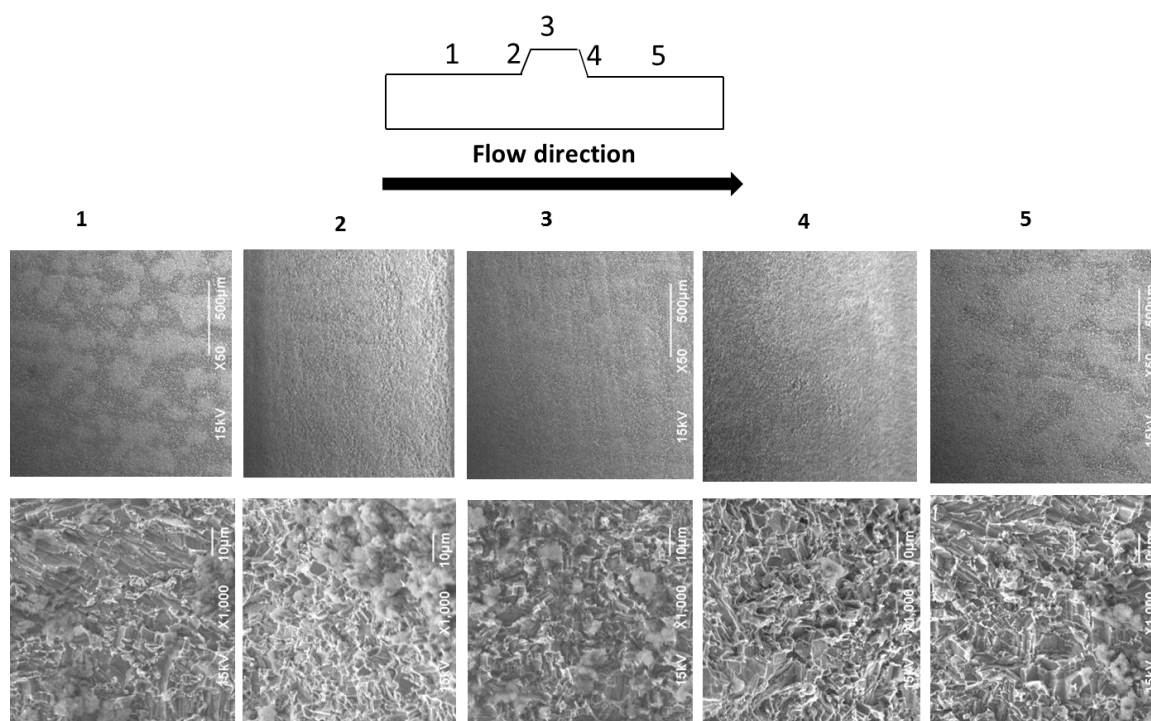


Figure 6-7: SEM images of protrusion Specimen 3 after the blank test. First row: 50X magnification; second row: 1000X magnification. Physical locations are defined by using 5 numbered individual regions in Figure 6-2. 1 wt.% NaCl, pH 5, 0.97 bar CO<sub>2</sub>, 25°C, 16 m/s, 4 day test duration, X65, 4 ppb to 30 ppb O<sub>2</sub>.

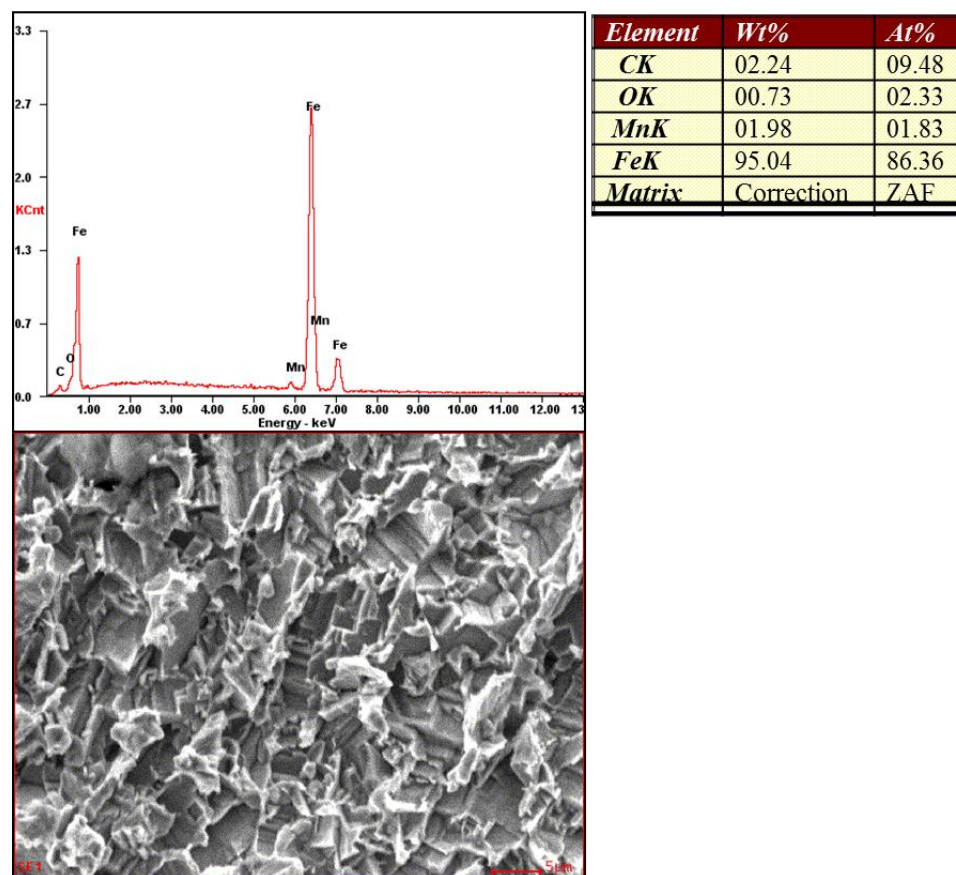


Figure 6-8: EDS analysis of flat Specimen 2 (150 grit) after the blank test. 1 wt.% NaCl, pH 5, 0.97 bar CO<sub>2</sub>, 25°C, 16 m/s, 4 day, X65, 4 ppb to 30 ppb O<sub>2</sub>.

### 6.3.2 Corrosion tests with inhibitor

To test the effect of mechanical stress on an inhibitor, a generic imidazoline-type inhibitor (TOFA imidazolinium chloride) was used at a concentration of 72 ppm<sub>v</sub> while other test parameters were unchanged. The specimens were pre-corroded for approximately 10 - 12 hours at the operating test conditions before the addition of inhibitor. Figure 6-9 shows the corrosion rate during the test with comparison to the blank test. It clearly shows that, after the addition of inhibitor, the general corrosion rate immediately decreases by more than 50% and then gradually decreases to 0.4 mm/yr. The

corrosion inhibitor effectively retarded the general corrosion rate by almost 95%, even in the presence of high flow velocity. A comparison of the surface morphologies of the specimens after the experiments shows a distinct difference between the blank test and the 72 ppm<sub>v</sub> inhibitor test.

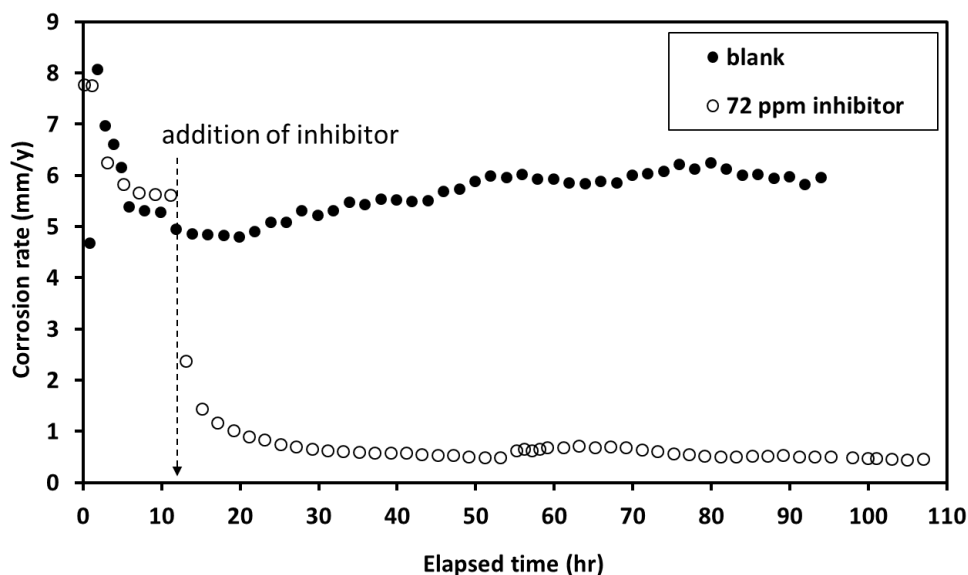


Figure 6-9: LPR corrosion rate for blank and 72 ppm<sub>v</sub> TOFA imidazoline inhibitor tests, B = 65 mV, 1wt.% NaCl, pH 5, 0.97 bar CO<sub>2</sub>, 25°C, 16 m/s, 4 day test duration, X65, 4 ppb to 30 ppb O<sub>2</sub>.

The surface morphologies of all weight loss specimens for the inhibition test are shown in from Figure 6-10 to Figure 6-15. For flat specimens with a varied initial surface polish, the final surfaces are quite similar with and without inhibitor due to the pre-corrosion step and a uniformly corroded surface can be observed (Figure 6-10 to Figure 6-12). Severe pitting corrosion was found on the region 3 (upper surface) of the protrusion specimen after the experiment, as shown in Figure 6-13.

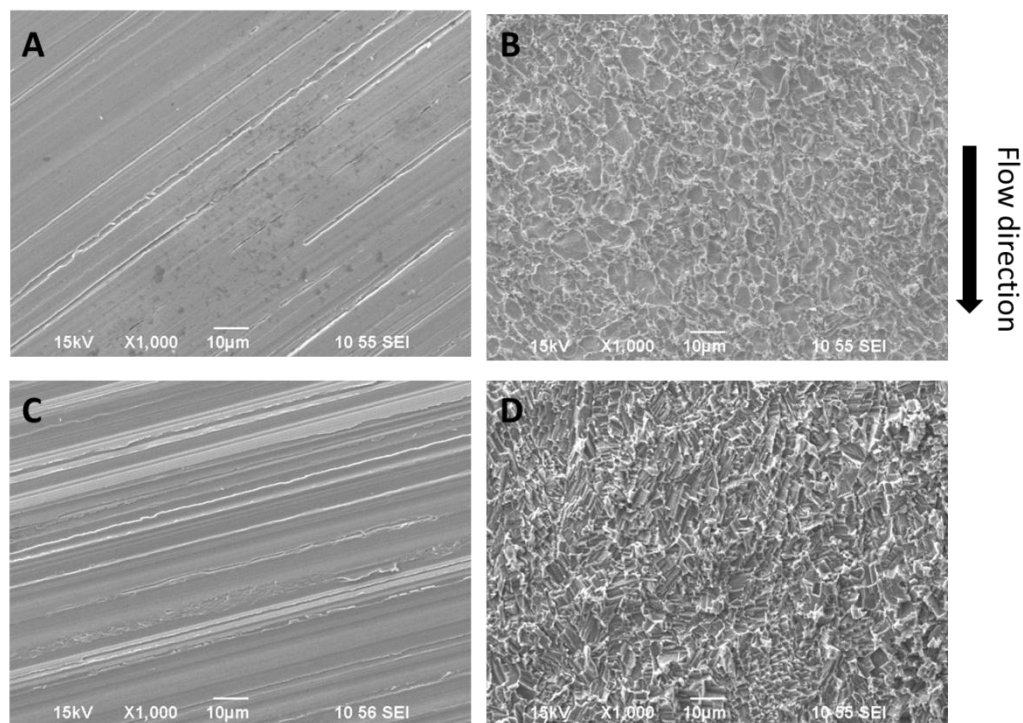


Figure 6-10: SEM images of flat Specimen 1 (600 grit finish) and Specimen 2 (150 grit finish) at 1000X magnification. 1 wt.% NaCl, pH 5, 0.97 bar CO<sub>2</sub>, 25°C, 72 ppm<sub>v</sub> inhibitor, 16 m/s, 4 day test duration, X65, 4 ppb to 30 ppb O<sub>2</sub>: A. Specimen 1 before test; B. Specimen 1 after test; C. Specimen 2 before test; D. Specimen 2 after test.

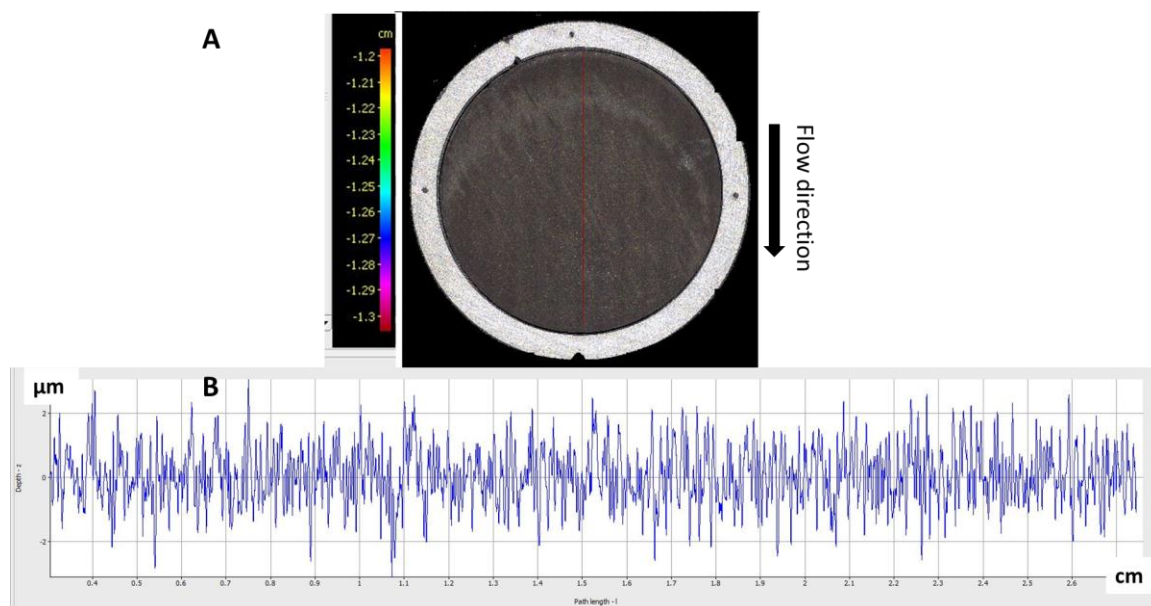


Figure 6-11: Profilometry results of flat Specimen 1 (600 grit finish) after the test. A: contour of the surface depth; B: line pattern depth scan of the surface marked by the red straight line in A.

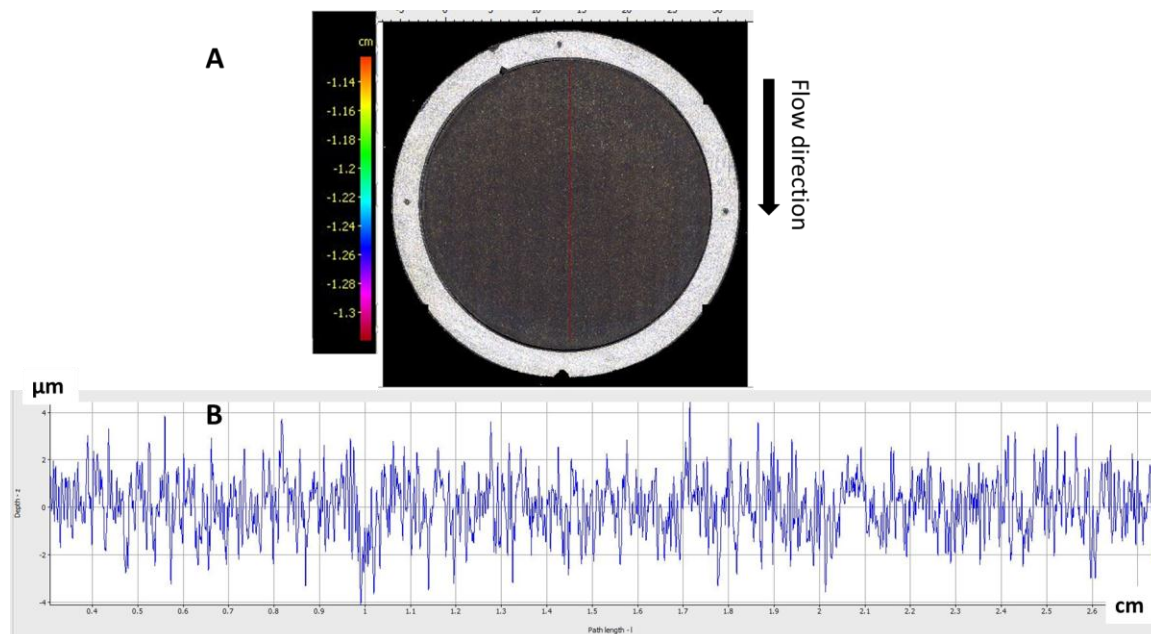


Figure 6-12: Profilometry results of flat Specimen 2 (150 grit finish) after the test. A: contour of the surface depth; B: line pattern depth scan of the surface marked by the red straight line in A.

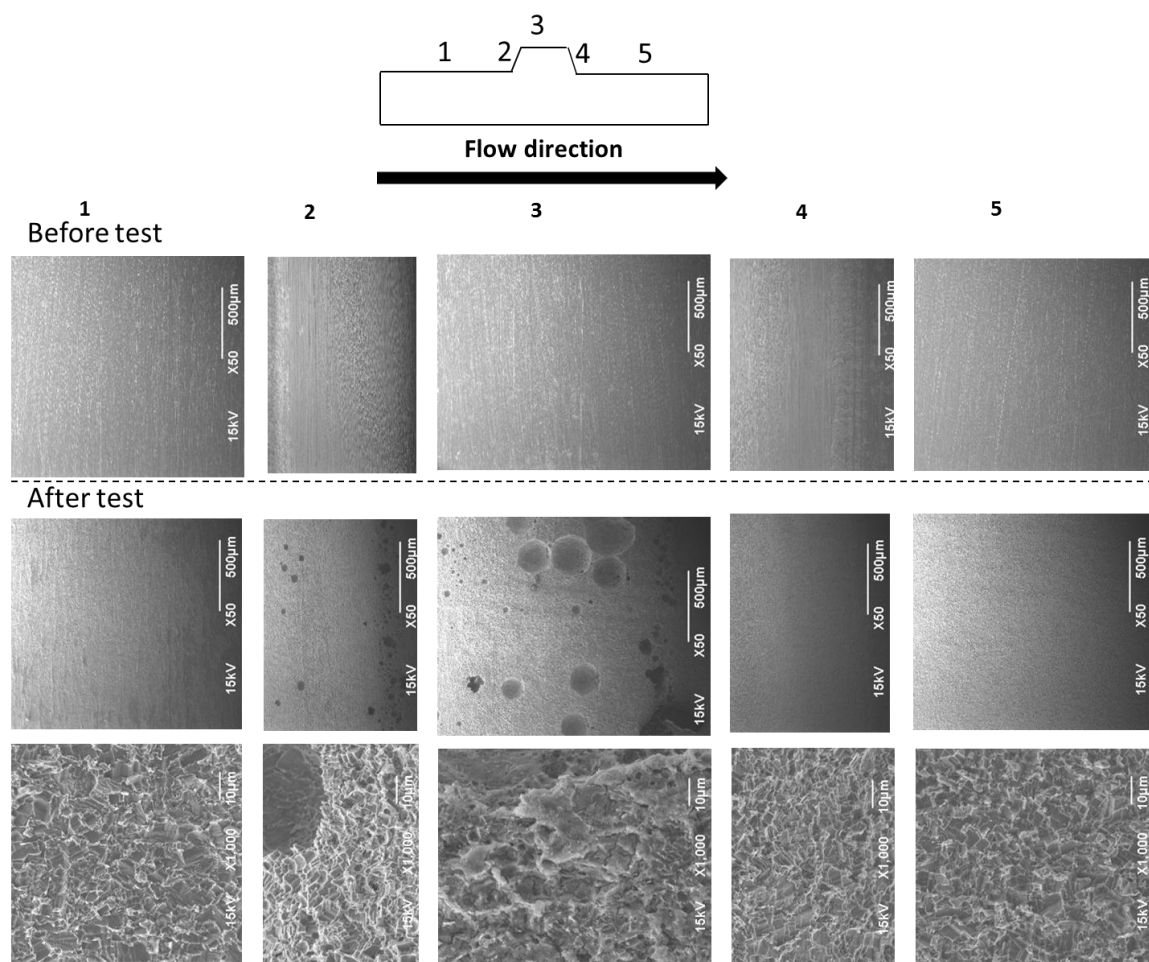


Figure 6-13: SEM images of protrusion Specimen 3. Before test: 1st row at 50X magnification. After test: 2nd row at 50X magnification; 3rd row at 1000X magnification. Physical locations are defined by using 5 numbered individual regions in Figure 6-2. 1 wt.% NaCl, pH 5, 0.97 bar CO<sub>2</sub>, 25°C, 72 ppm<sub>v</sub> inhibitor, 16 m/s, 4 day test duration, X65, 4 ppb to 30 ppb O<sub>2</sub>.

The surface morphologies of the protrusion specimen with respect to flow direction show a series of small pits at the leading edge between region 2 and 3. In addition, several major pits were found in the middle of region 3, the top of the protrusion. The depths of the observed pits were evaluated by profilometry. Figure 6-14A shows the surface profile for the region on the top of the protrusion. The pattern of pit distribution is

consistent with the observations from SEM. One of the deepest pits was found to be 140  $\mu\text{m}$  deeper than the surrounding area (Figure 6-14B), which is equivalent to a pit penetration rate (pit depth over a unit time) of 11.4 mm/yr. Nonetheless, no pitting was observed on regions 1, 4 and 5, which generally showed a uniformly corroded surface similar to the flat specimens.

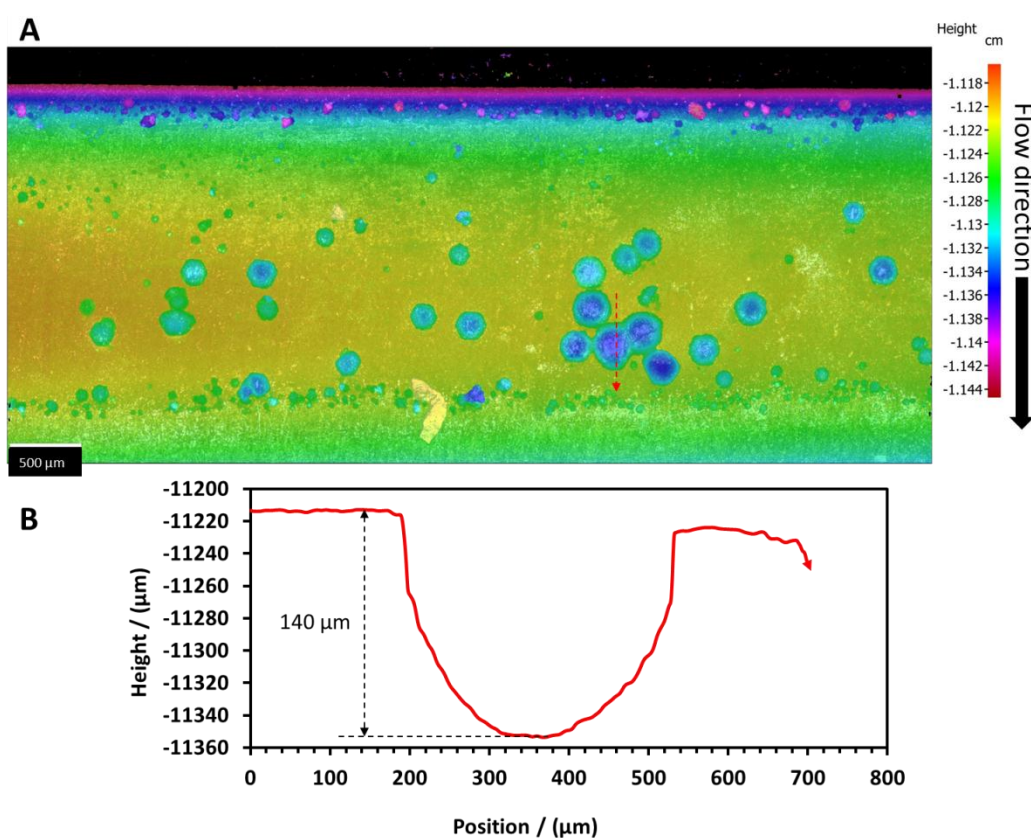


Figure 6-14: (A): Profilometry image of protrusion Specimen 3 after experiment on the top of protrusion, region 3 in Figure 6-2; (B): line pattern depth scan of the dotted red line marked in (A). 1 wt.% NaCl, pH 5, 0.97 bar  $\text{CO}_2$ , 25°C, 72 ppm<sub>v</sub> inhibitor, 16 m/s, 4 day test duration, X65, 4 ppb to 30 ppb  $\text{O}_2$ .

The chemical composition at the top of the protrusion was analyzed by EDS (region 3). Figure 6-15 shows the composition inside a pit and the surrounding uniformly

corroded area. Both of them indicate iron dissolution without the formation of  $\text{FeCO}_3$  layers. EDS was performed on all specimens after the test, which showed similar results.

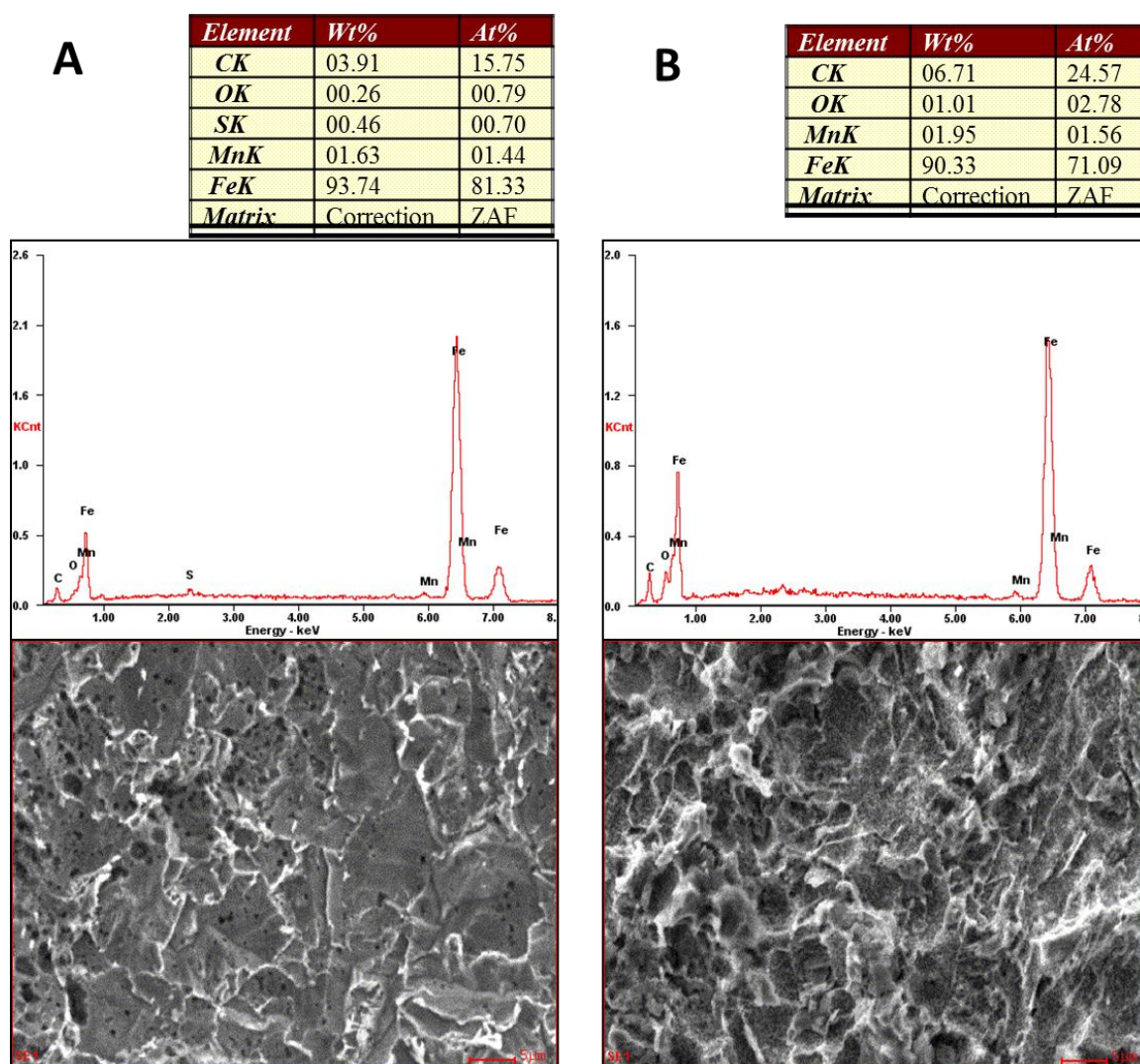


Figure 6-15: EDS analysis of protrusion Specimen 3 after test on the top of protrusion, region 3 in Figure 6-2. A: inside a pit; B: the surrounding flat area above the pit.

The 72 ppm<sub>v</sub> inhibitor test demonstrates that this TOFA imidazolium chloride inhibitor effectively retarded the general corrosion rate even in this high flow velocity

environment. However, for areas of a sudden surface geometrical change, *e.g.*, protrusion, severe localized corrosion occurred. Moreover, it was unclear as to why localized corrosion was most severe at the top of the protrusion region. Further analysis is needed as introduced in the following sections.

### *6.3.3 Effect of oxygen ingress on corrosion inhibition*

It has been reported that O<sub>2</sub> ingress can increase corrosion rate significantly in a corrosion inhibition system. Gulbrandsen et al. concluded that the corrosion inhibition was not affected by WSS in a high flow velocity system (up to 20 m/s) as long as the O<sub>2</sub> level was low [17]. They suggested that O<sub>2</sub> may penetrate corrosion inhibitor films to reach the steel surface and this process may be accelerated by increased flow velocities due to the enhanced mass transfer effect. However, the effect of O<sub>2</sub> ingress on localized corrosion in the presence of inhibitor was not studied. It was first suspected that the localized corrosion observed on the protrusion specimen in this research was related to O<sub>2</sub> contamination during the experiment since the system was not continuously monitored for oxygen concentration. For the limited number of oxygen concentration readings, the highest value recorded was 30 ppb while the lowest value was 4 ppb. Because of this, the concentration of O<sub>2</sub> in the experiment was considered to be between 4 ppb and 30 ppb.

Consequently, the experiment was repeated with 72 ppm<sub>v</sub> inhibitor and continuous O<sub>2</sub> concentration measurements were conducted. The O<sub>2</sub> level in this experiment was maintained lower than 2 ppb during the entire test by continuously purging the system

with an ultra-high purity CO<sub>2</sub> gas (99.999%). Figure 6-16 shows the comparison of corrosion rate between tests with different levels of O<sub>2</sub>. It shows that the general corrosion was well inhibited in the presence of 72 ppm<sub>v</sub> inhibitor for both tests. The test with strict O<sub>2</sub> control had a slightly lower corrosion rate after the addition of inhibitor, which was consistent with the observations by Gulbrandsen et al. [17].

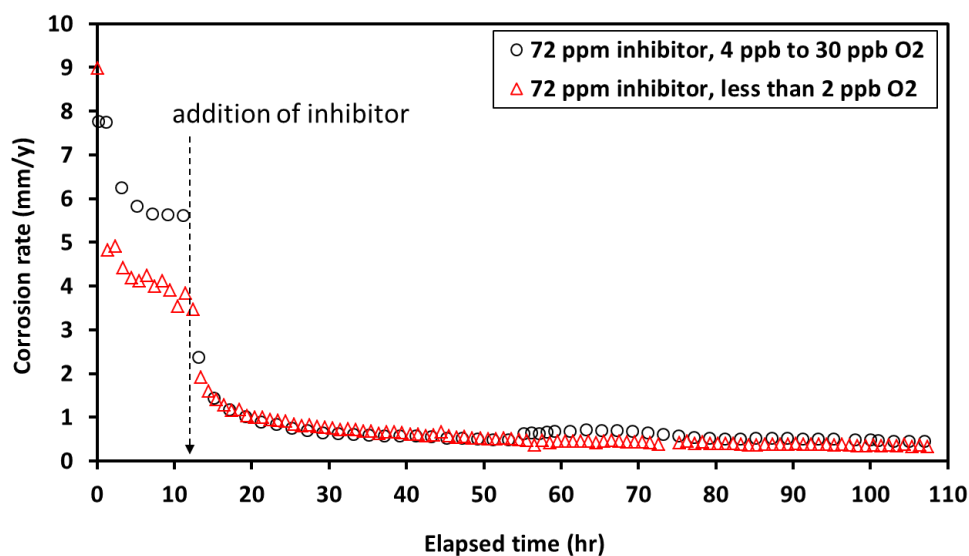


Figure 6-16: LPR corrosion rate for 72 ppm<sub>v</sub> inhibitor tests with varied levels of O<sub>2</sub> concentration, B = 65 mV, 1 wt.% NaCl, pH 5, 0.97 bar CO<sub>2</sub>, 25°C, 16 m/s, 4 day test duration, X65.

Similarly, the surface analysis revealed that only uniform corrosion occurred for flat specimens, as shown in Figure 6-17.

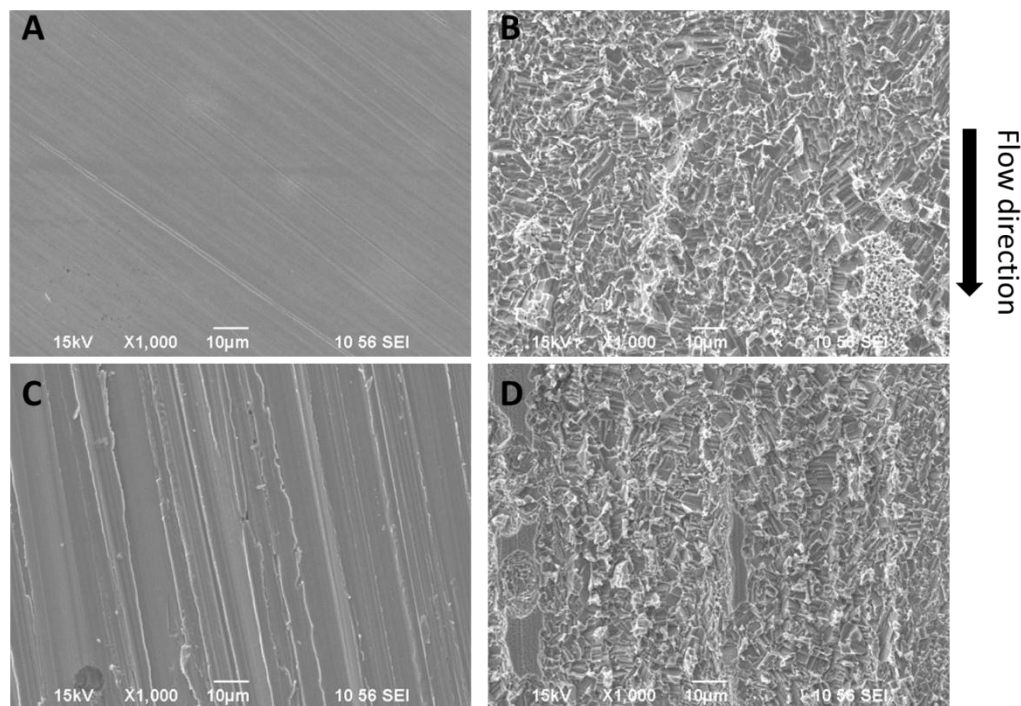


Figure 6-17: SEM images of flat Specimen 1 (600 grit finish) and Specimen 2 (150 grit finish) at 1000X magnification. 1 wt.% NaCl, pH 5, 0.97 bar CO<sub>2</sub>, 25°C, 72 ppm<sub>v</sub> inhibitor, 16 m/s, 4 day test duration, X65, O<sub>2</sub> < 2 ppb: A. Specimen 1 before test; B. Specimen 1 after test; C. Specimen 2 before test; D. Specimen 2 after test.

The surface morphology of the protrusion specimen before and after this experiment is shown in Figure 6-18. Once again, pitting corrosion was found on the upstream slope and top of the protrusion regions. Figure 6-19A shows the surface depth profile at the top of the protrusion region obtained by profilometry. One of the deepest pits was found to be 154 µm below the surrounding area, which is equivalent to a pit penetration rate (PR) of 12.5 mm/yr.

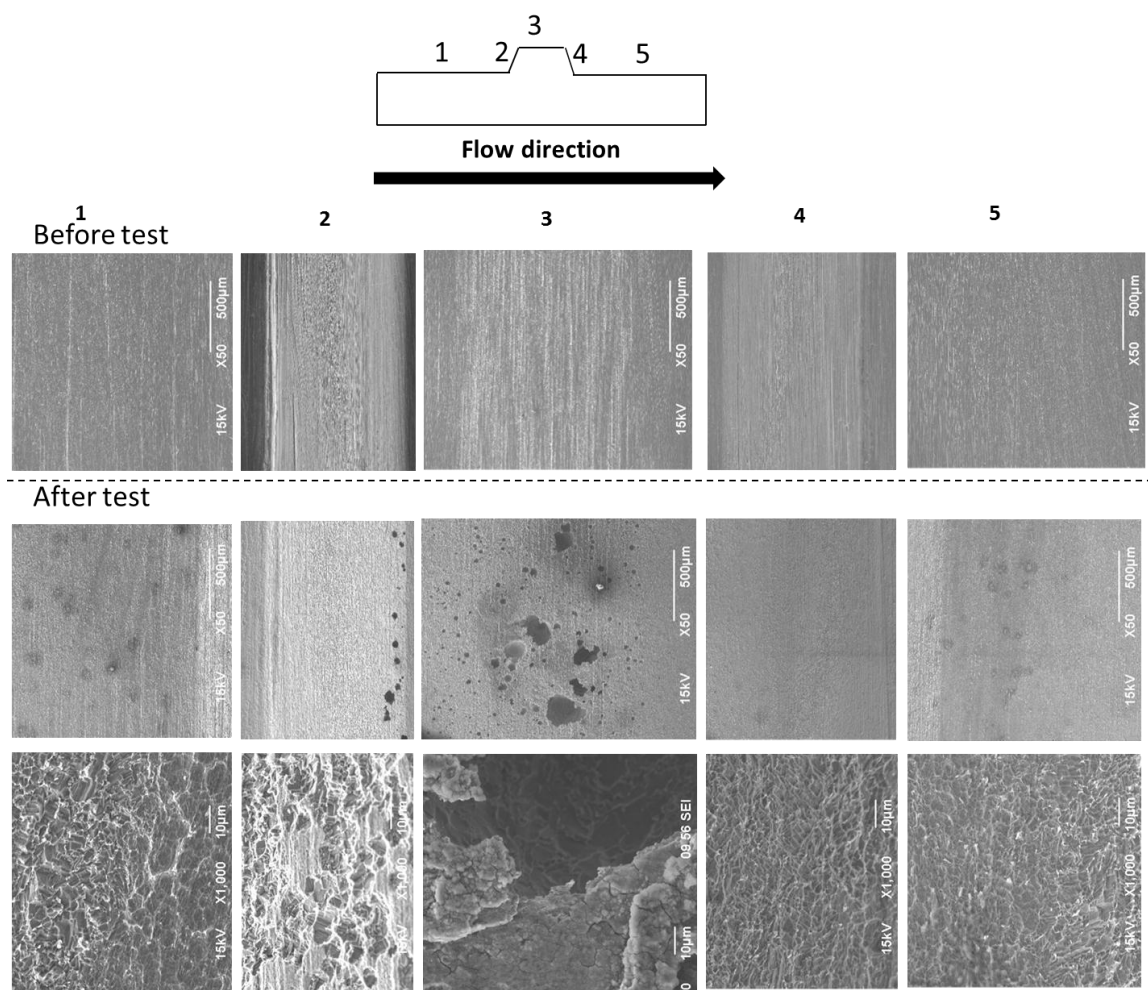


Figure 6-18: SEM images of protrusion Specimen 3. Before test: 1st row at 50X magnification. After test: 2nd row at 50X magnification; 3rd row at 1000X magnification. Physical locations are defined by using 5 numbered individual regions in Figure 6-2. 1 wt.% NaCl, pH 5, 0.97 bar CO<sub>2</sub>, 25°C, 72 ppm<sub>v</sub> inhibitor, 16 m/s, 4 day test duration, X65, O<sub>2</sub> < 2 ppb.

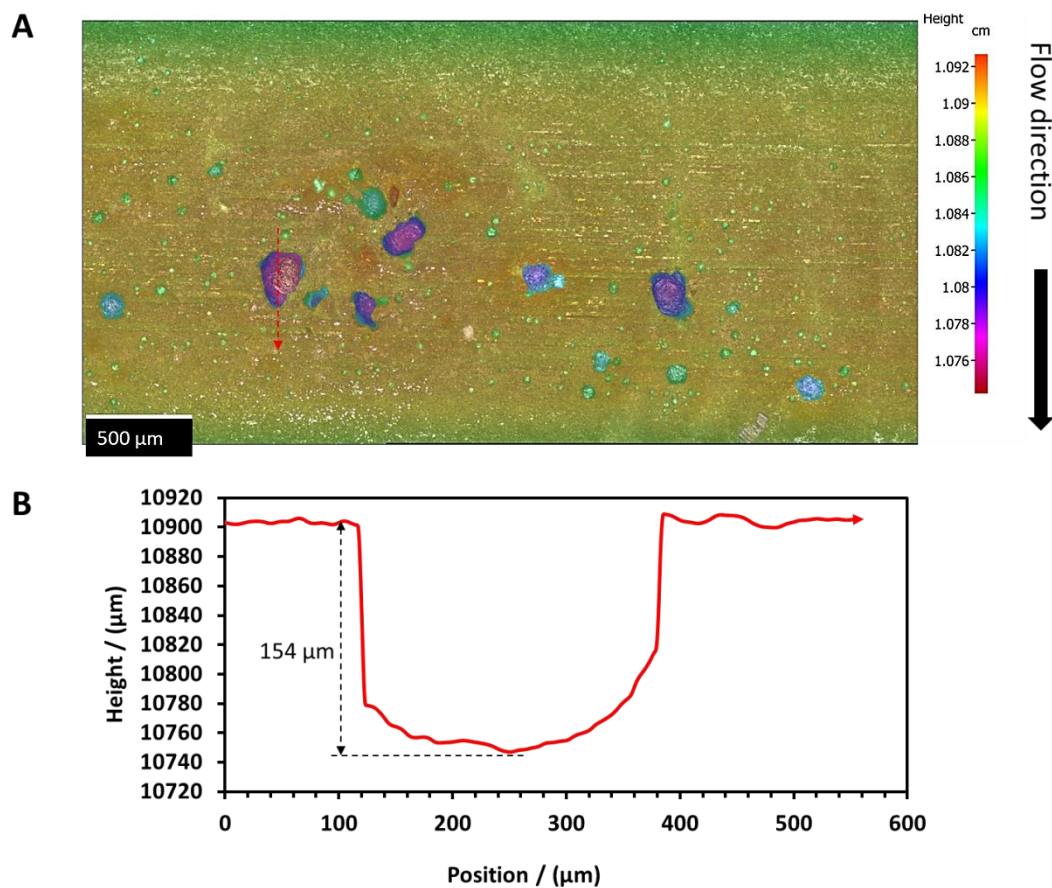


Figure 6-19: (A): Profilometry image of protrusion Specimen 3 after experiment on top of protrusion, region 3 in Figure 6-2; (B): line pattern depth scan marked by the dotted red line in (A). 1 wt.% NaCl, pH 5, 0.97 bar CO<sub>2</sub>, 25°C, 72 ppm<sub>v</sub> inhibitor, 16 m/s, 4 day test duration, X65, O<sub>2</sub> < 2 ppb.

The chemical composition of all specimens before and after the test was analyzed by EDS, as shown in Figure 6-20, Figure 6-21 and Figure 6-22. In the low O<sub>2</sub> environment, all specimens showed similar results in that the steel surface was corroded with no FeCO<sub>3</sub> layer formation.

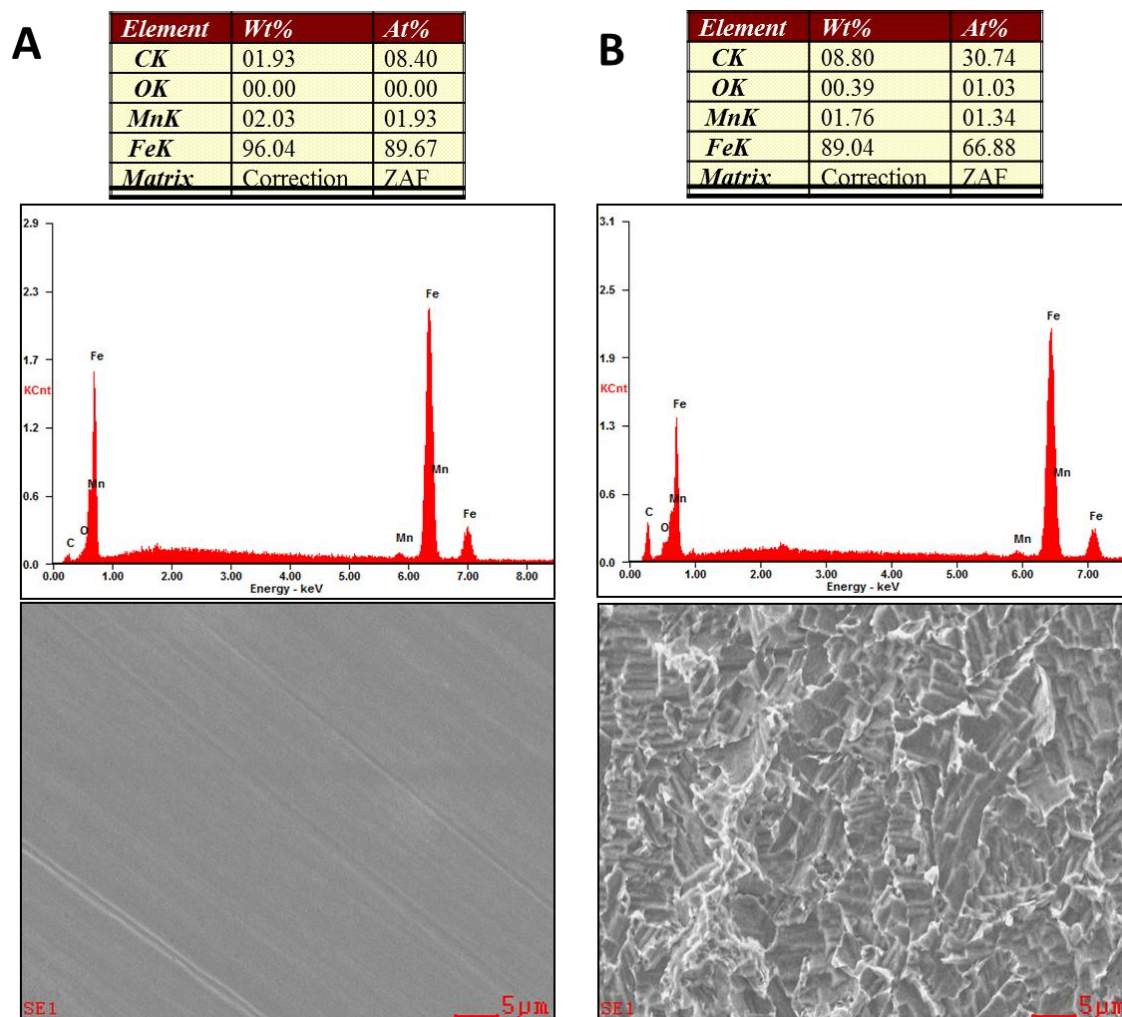
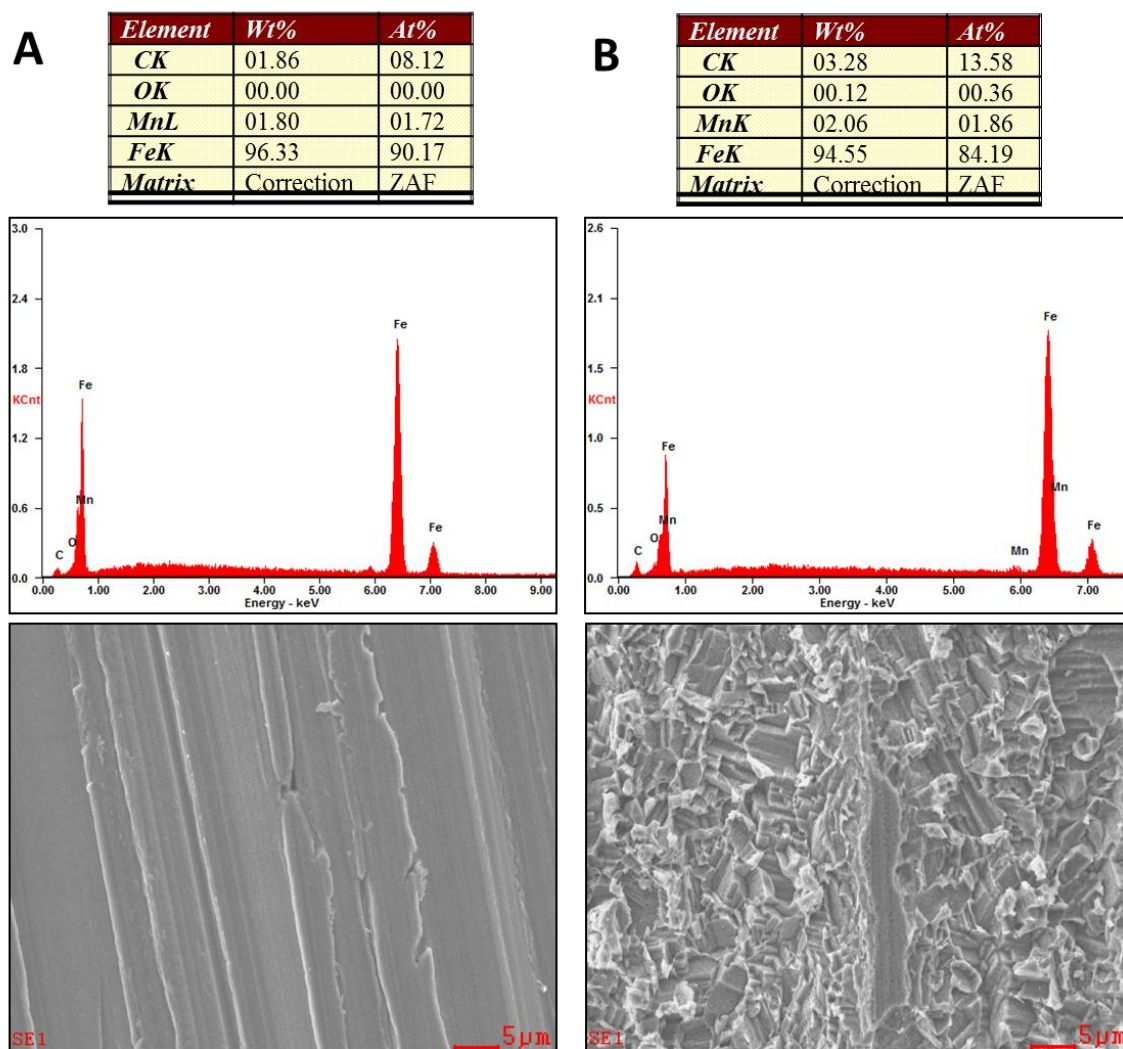


Figure 6-20: EDS analysis of flat Specimen 1 (600 grit finish). A: before experiment; B: after experiment. 1 wt.% NaCl, pH 5, 0.97 bar CO<sub>2</sub>, 25°C, 72 ppm<sub>v</sub> inhibitor, 16 m/s, 4 day test duration, X65, O<sub>2</sub> < 2 ppb.



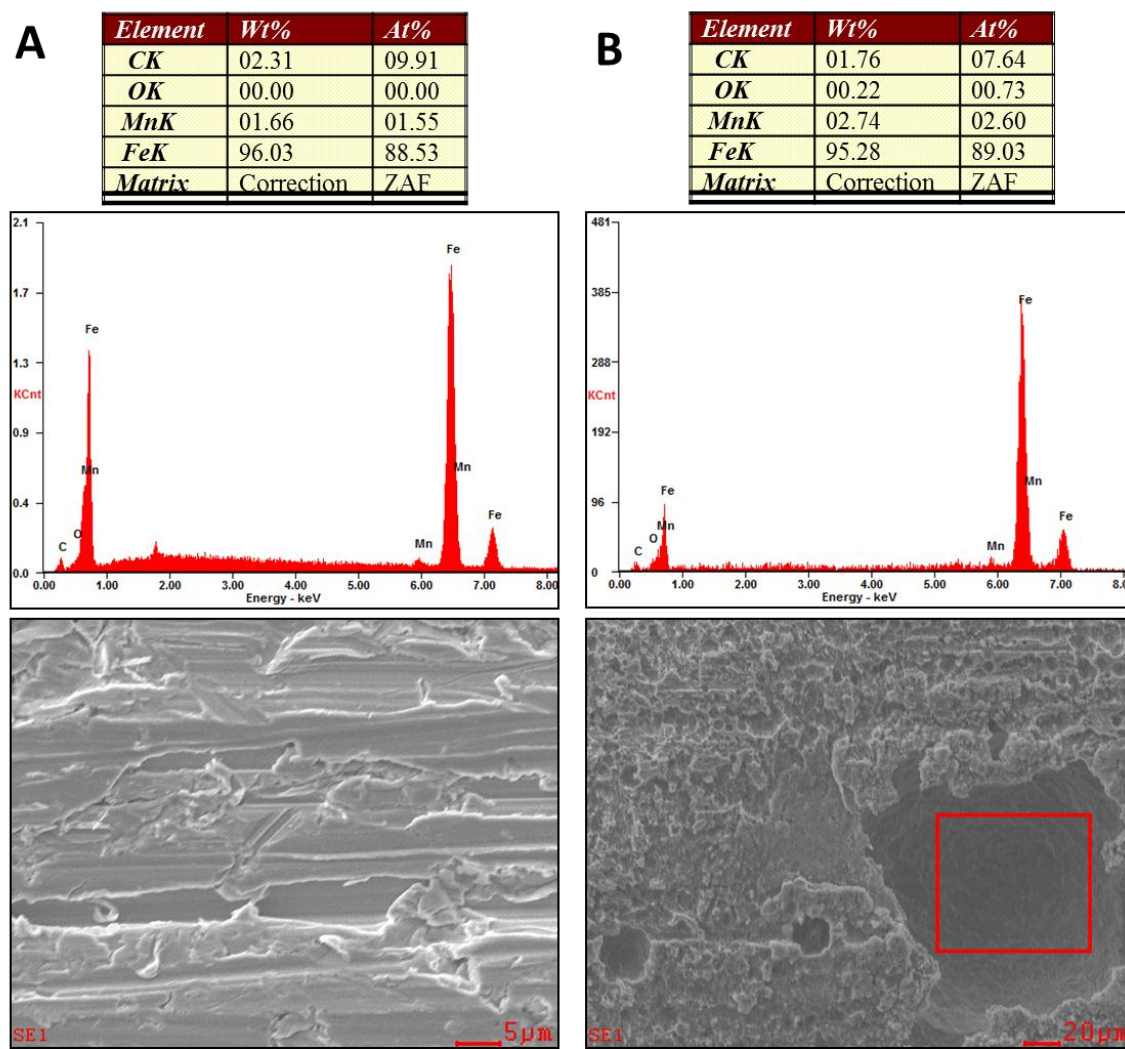


Figure 6-22: EDS analysis of protrusion Specimen 3. A: before experiment; B: after experiment, in a pit at the top of protrusion, region 3 in Figure 6-2. 1 wt.% NaCl, pH 5, 0.97 bar CO<sub>2</sub>, 25°C, 72 ppm<sub>v</sub> inhibitor, 16 m/s, 4 day test duration, X65, O<sub>2</sub> < 2 ppb.

Compared to the results of the test with 4 ppb to 30 ppb O<sub>2</sub>, the locations of the pits were similar. Through these two experiments, it can be concluded that this severe localized corrosion on the protrusion specimen was not caused by O<sub>2</sub> ingress. Other possible causes must be sought to explain the experimental results.

### 6.3.4 Effect of wall shear stress on corrosion inhibition

Besides the effect of O<sub>2</sub> ingress, it is possible that the surface geometrical change near the protrusion regions significantly altered the local hydrodynamic conditions, leading to a higher magnitude of local mechanical stresses and causing local removal of inhibitor from the steel surface. CFD simulation was deemed a suitable diagnostic tool to analyze the hydrodynamic conditions around the protrusion specimen. The actual geometry in the TCFC surrounding the protrusion specimen was constructed in a computer simulation (as seen in Figure 6-23). The symmetric plane is outlined by red lines, which is perpendicular to the bottom plate of the TCFC and parallel to the flow direction.

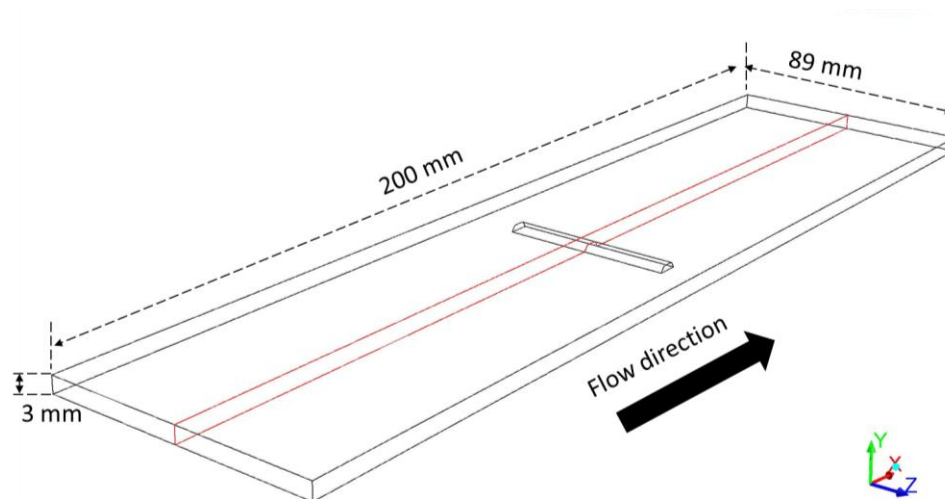


Figure 6-23: Schematic of the CFD simulation geometry with the symmetric plane outlined (red lines).

Hydrodynamic properties such as flow velocity, WSS and static pressure were calculated. Figure 6-24 shows the flow velocity profile on the symmetric plane. It clearly demonstrates that the protrusion significantly changes the local flow velocity profile. The

highest flow velocity (28 m/s) occurred at the leading edge between the upstream slope and the top of protrusion regions. An overview of the WSS distribution surrounding the protrusion specimen is shown in Figure 6-25. In addition, the local WSS distribution on the symmetric plane is shown in Figure 6-26A, while the WSS at the bottom of the symmetric plane along the flow direction is plotted in Figure 6-26B. It can be seen that the upstream region of the protrusion specimen had an average WSS of 600 - 800 Pa, which was consistent with the bulk WSS measurements by floating element sensor at the same flow conditions (see Figure 5-2). However, on the leading edge of the protrusion specimen a sudden increase of WSS occurred. A WSS value of approximately 4600 - 4800 Pa was calculated, while the WSS value was 1900 - 2300 Pa in the middle of the top protrusion region. If WSS was the cause for the localized inhibitor removal, these values are inconsistent with the findings by surface analysis that more severe pits were found at the top of the protrusion region instead of the leading edge. In addition, the WSS required to remove this imidazolinium chloride inhibitor from a steel surface is expected to be on the order of 50 MPa to 100 MPa as measured by atomic force microscopy (AFM) [22], which is several orders of magnitude larger than the calculated WSS values on the protrusion of this specimen. Therefore, it is unlikely that local WSS fluctuations were the major cause of the pitting corrosion.

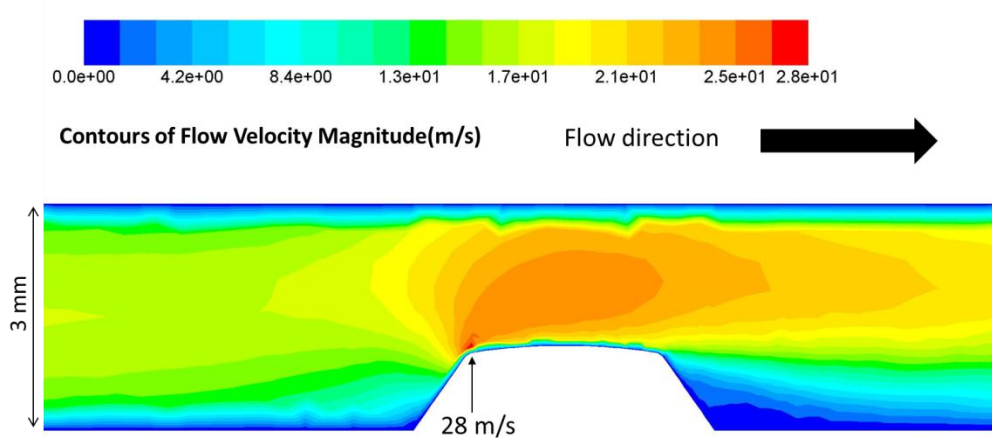


Figure 6-24: Flow velocity magnitude distribution on the symmetric plane.

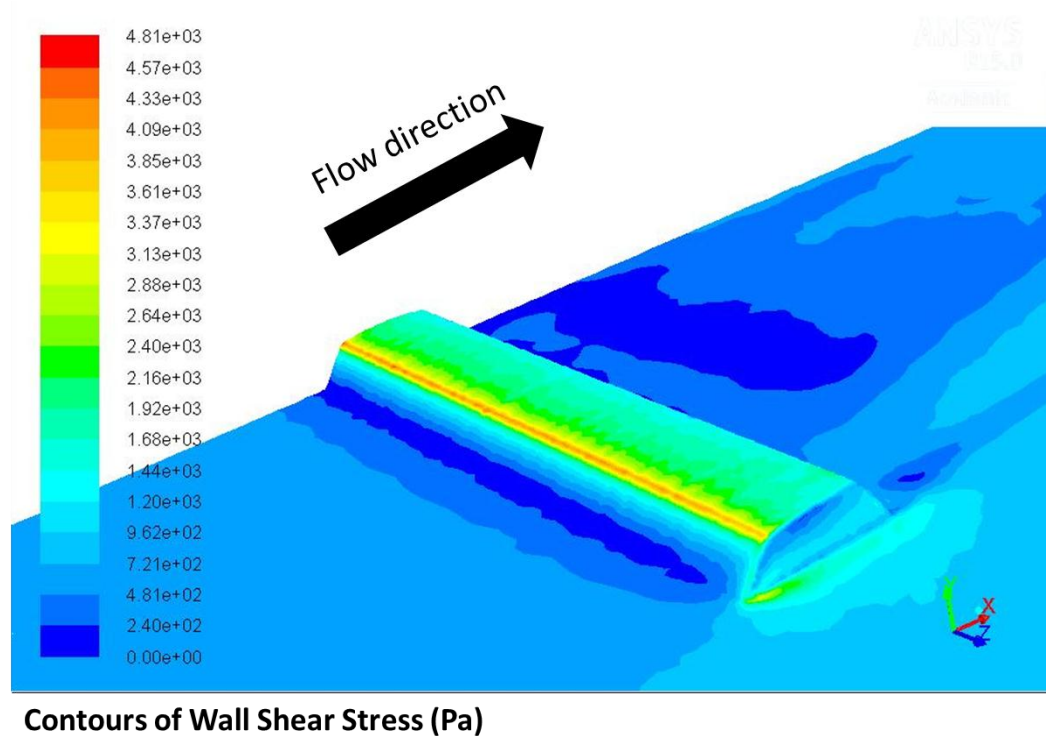


Figure 6-25: Wall shear stress distribution at the bottom plate of the TCFC near the specimen protrusion.

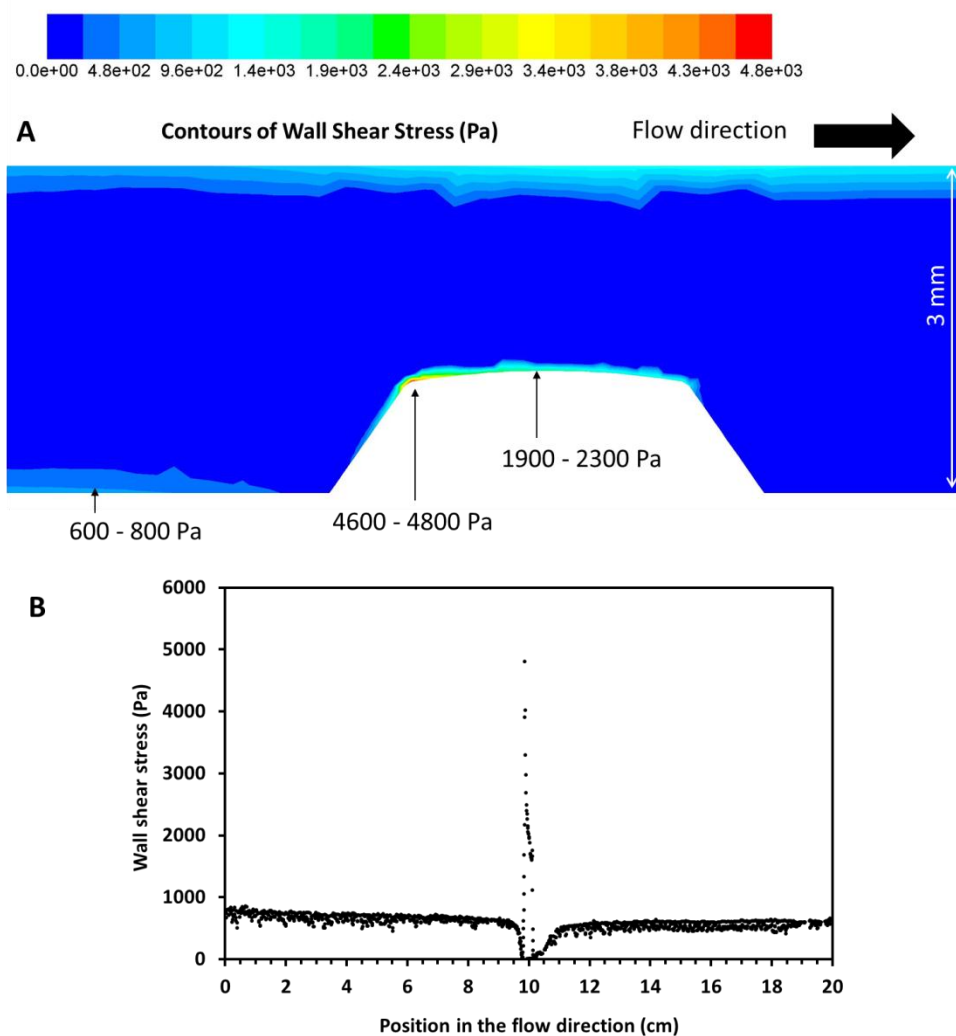


Figure 6-26: Wall shear stress distribution: A. on the symmetric plane; B. on the bottom wall of the symmetric plane.

### 6.3.5 Effect of cavitation on corrosion inhibition

Because of the drastic increase of flow velocity at the leading edge of the protrusion, the pressure at the same location was greatly reduced according to Bernoulli's principle [95]. The pressure distribution on the symmetric plane along the flow direction is shown in Figure 6-27A, which clearly illustrates such pressure fluctuations. From this graph, a low pressure zone approximately -5.1 bar compared to the simulation inlet, is found at the

leading edge of the protrusion specimen. The pressure in the middle of the top protrusion region then quickly recovers to -2.4 bar as compared to the simulation inlet. It should be noted that the gauge pressure at the simulation outlet was set to be 0 bar as a reference pressure.

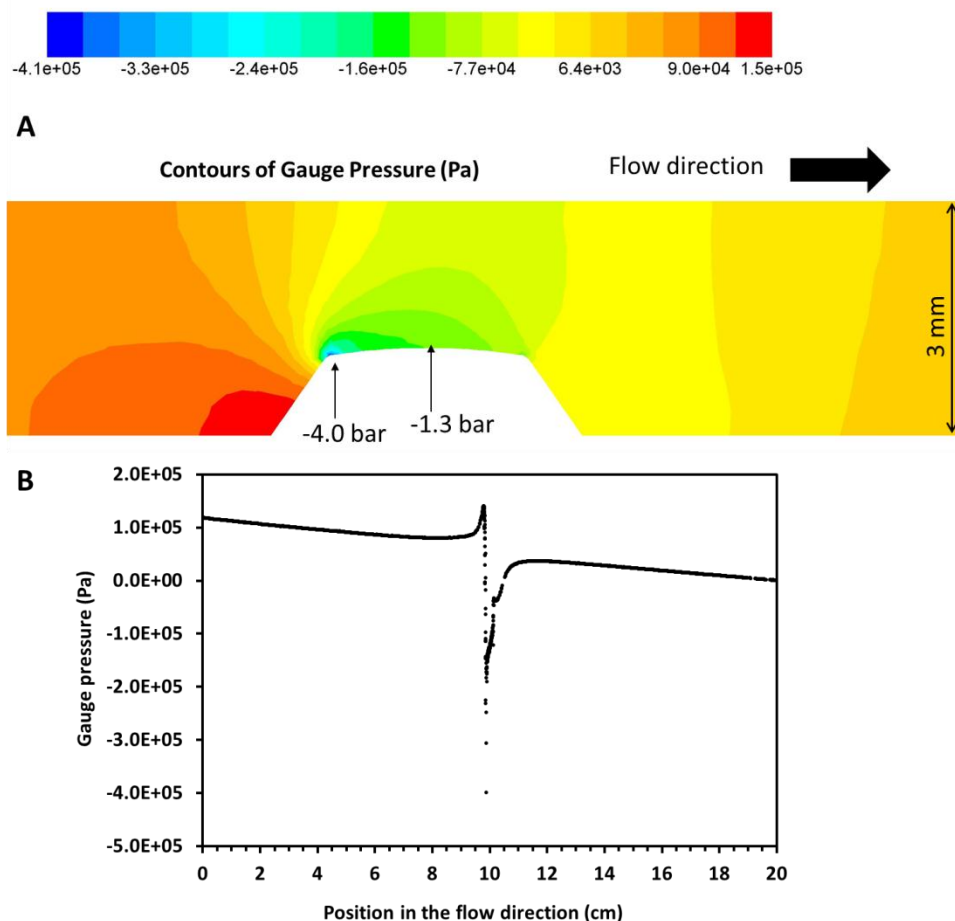


Figure 6-27: Gauge pressure distribution: A. on the symmetric plane; B. on the bottom wall of the symmetric plane.

This unusual large pressure fluctuation at the leading edge may be the cause of the pitting corrosion. During an additional experiment, pressure measurements at multiple

locations along the TCFC were conducted. Based on the pressure readings, the dimensions of the TCFC and the dimensions of the simulation domain, the absolute static pressure at the simulation inlet was calculated to be approximately 4.2 bara (see Appendix 4). Therefore, the absolute static pressures at the leading edge and in the middle of the top protrusion area were calculated to be -0.9 bara and 1.8 bara, respectively. Although the absolute pressure at the leading edge cannot be negative, the calculations strongly suggest that an extremely low pressure zone existed at the leading edge. It is highly possible that the local pressure was reduced to the water vapor pressure (3.2 kPa at 25°C), and vapor bubbles were formed due to cavitation.

It was hypothesized that cavitation on the top of the protrusion would cause the loss of inhibitor and initiation of localized corrosion. Formation of bubbles at the leading edge would have created a large gas-liquid interface and consumed a fraction of the inhibitor leading to a local depletion. These bubbles were then swept downstream by the flow where they collapsed when the local pressure recovered above the water vapor pressure (0.032 bar). The collapsed bubbles would have also generated significantly large mechanical stresses that could locally remove inhibitors and induced localized corrosion. Calculations found in the open literature indicate that mechanical stresses of the order of  $10^8 - 10^9$  Pa are possible due to implosions of cavitation bubbles [96–98], which exceed the required forces to remove inhibitor films from a steel substrate. This is a plausible explanation for the experimental results.

In order to verify the cavitation mechanism derived from CFD results and experimental evidence, an additional test was designed. The idea was to eliminate the

hydrodynamic conditions that lead to cavitation. Therefore, localized corrosion would not be expected if cavitation was the cause. For the previous experiments, the protrusion specimen was located at the most downstream port (port 4), as shown in Figure 6-4. The measured pressure drop between port 1 and port 4 was 1.2 bar at the flow velocity of 16 m/s (see Appendix 4). Hence, by moving the protrusion specimen to port 1 (closest to the flow upstream), the inlet pressure of the protrusion should gain 1.2 bar. According to the simulation in the previous section, the new calculated absolute pressure at the leading edge of the protrusion would be 0.3 bara, which is higher than the water vapor pressure at this temperature. Therefore, neither cavitation nor localized corrosion would be expected.

Except for the change of the protrusion specimen location in the TCFC, all other experimental conditions were maintained the same as previous experiments. Figure 6-28 shows the LPR corrosion rate for this experiment. A similar general corrosion rate as compared to previous tests indicates that the bulk test conditions remained the same. The surface morphologies of both flat and protrusion specimens after the test were examined by SEM, as shown in Figure 6-29 and Figure 6-30, respectively. No localized corrosion was found for both specimens. By changing the protrusion specimen location, the local flow condition for cavitation occurring was eliminated. Therefore, the results indicate that cavitation is the likely cause of the localized corrosion observed in previous tests.

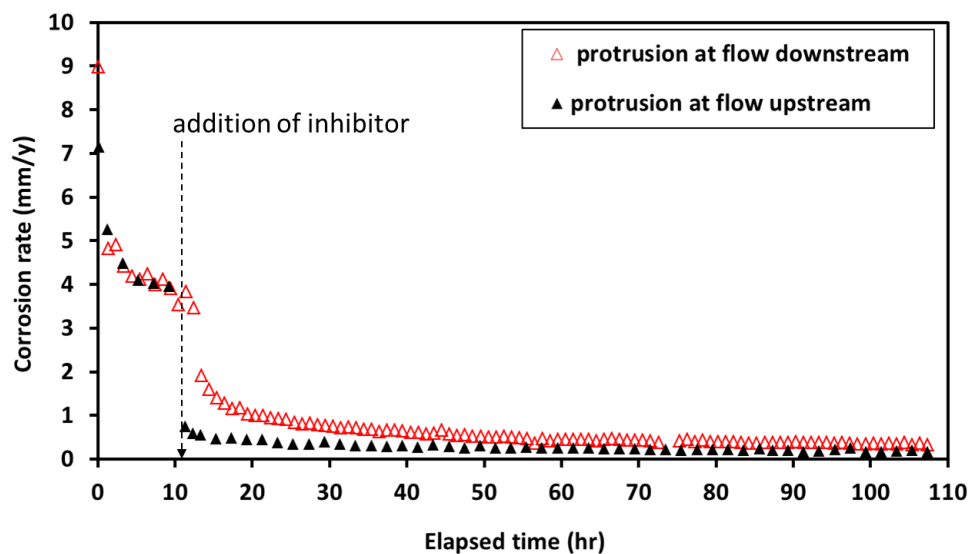


Figure 6-28: LPR corrosion rate for 72 ppm<sub>v</sub> inhibitor tests with changes of the protrusion specimen location, B = 65 mV. 1 wt.% NaCl, pH 5, 0.97 bar CO<sub>2</sub>, 25°C, 16 m/s, 4 day test duration, X65, O<sub>2</sub> < 2 ppb.

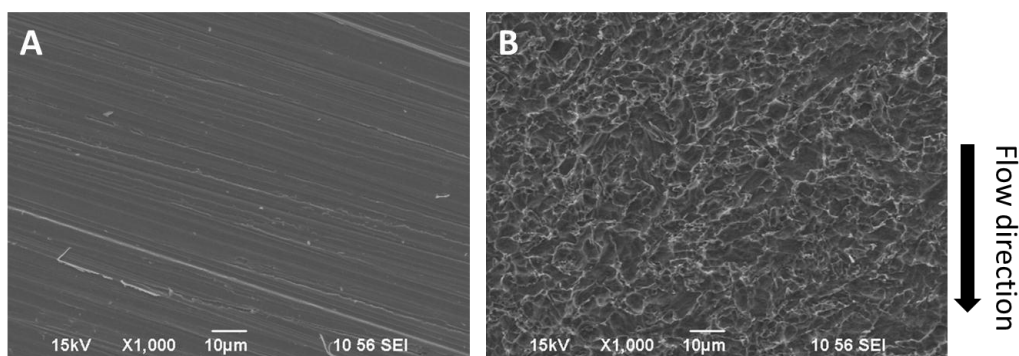


Figure 6-29: SEM images of flat Specimen 1 (600 grit finish) at 1000X magnification. 1 wt.% NaCl, pH 5, 0.97 bar CO<sub>2</sub>, 25°C, 72 ppm<sub>v</sub> inhibitor, 16 m/s, 4 day test duration, X65, O<sub>2</sub> < 2ppb: A. Specimen 1 before test; B. Specimen 1 after test.

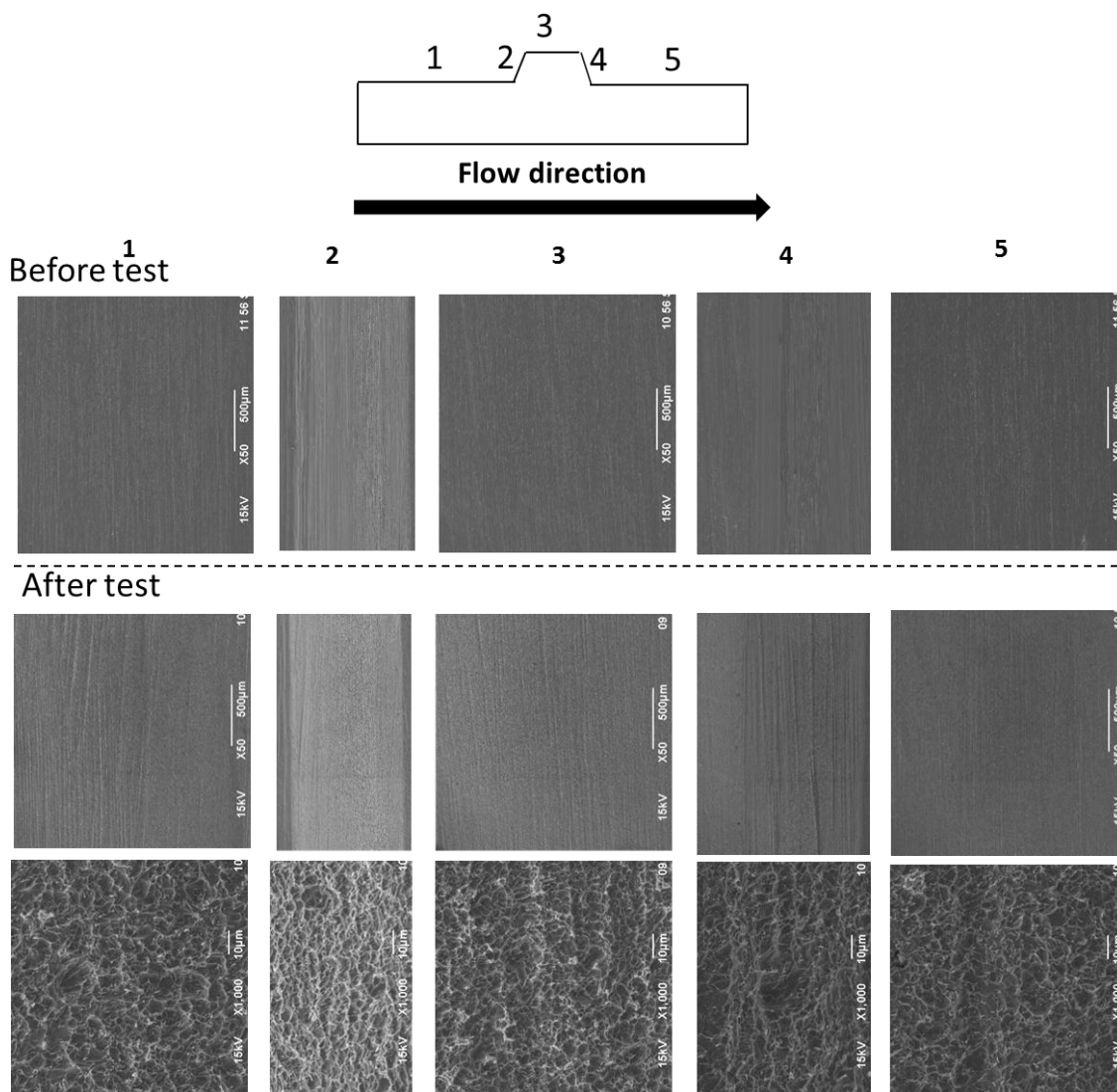


Figure 6-30: SEM images of protrusion Specimen 3 on the most upstream port in the TCFC (port 1). Before test: 1st row at 50X magnification. After test: 2nd row at 50X magnification; 3rd row at 1000X magnification. Physical locations are defined by using 5 numbered individual regions in Figure 6-2. 1 wt.% NaCl, pH 5, 0.97 bar CO<sub>2</sub>, 25°C, 72 ppm<sub>v</sub> inhibitor, 16 m/s, 4 day test duration, X65, O<sub>2</sub> < 2 ppb.

### *6.3.6 Mitigation of cavitation induced localized corrosion*

#### *6.3.6.1 Effect of inhibitor concentration*

By now, it is understood that cavitation on the protrusion was able to disrupt the adsorbed inhibitors on the metal surface and led to pitting corrosion. But if an excess amount of inhibitor is used, can this type of localized corrosion be suppressed? Subsequently, an experiment with a very high inhibitor concentration (720 ppm<sub>v</sub> inhibitor, 10 times the concentration used in previous tests) was conducted. This test would examine if a sufficient amount of inhibitor could be used to mitigate localized pitting corrosion due to cavitation. The specimen arrangement remained the same as shown in Figure 6-4 with the protrusion specimen at the most downstream port (port 4) where cavitation occurred. Figure 6-31 shows the LPR corrosion rate for the 720 ppm<sub>v</sub> inhibitor test along with results from other tests. As expected, the trend is similar to other tests indicating that the general corrosion was effectively inhibited. The surface morphologies of the flat and protrusion specimens before and after the experiments are shown in Figure 6-32 and Figure 6-33, respectively. No localized corrosion was observed.

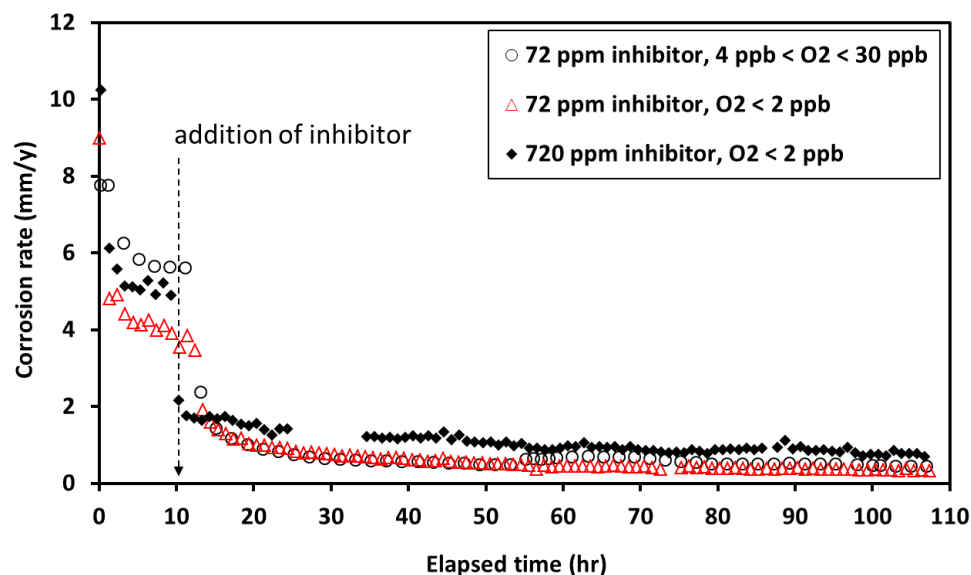


Figure 6-31: LPR corrosion rate for 720 ppm<sub>v</sub> inhibitor test, B = 65 mV. 1 wt.% NaCl, pH 5, 0.97 bar CO<sub>2</sub>, 25°C, 16 m/s, 4 day test duration, X65.

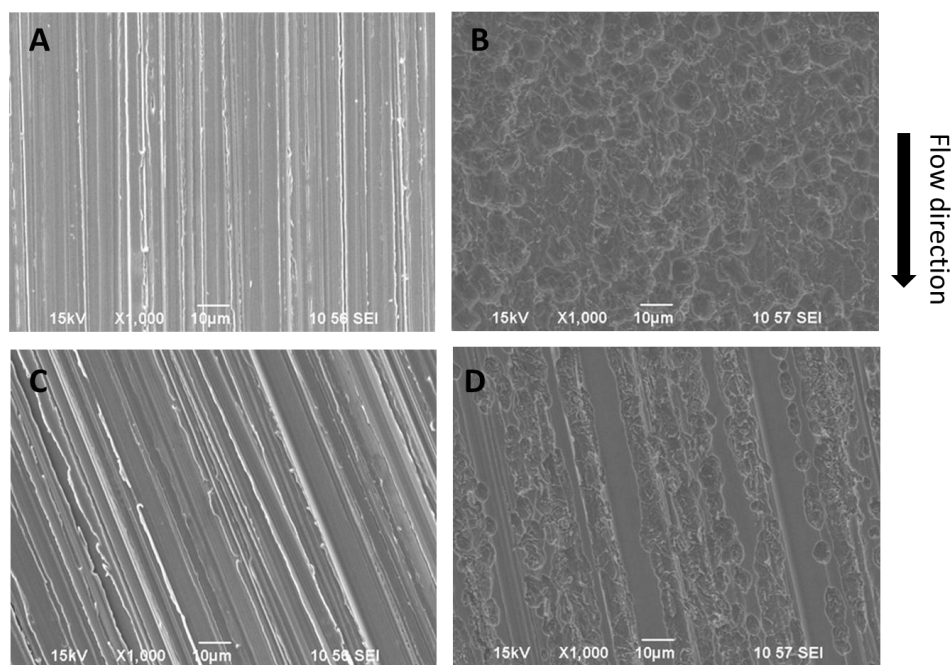


Figure 6-32: SEM images of flat Specimen 1 (600 grit finish) and Specimen 2 (150 grit finish) at 1000X magnification. 1 wt.% NaCl, pH 5, 0.97 bar CO<sub>2</sub>, 25°C, 720 ppm<sub>v</sub> inhibitor, 16 m/s, 4 day test duration, X65, O<sub>2</sub> < 2ppb: A. Specimen 1 before test; B. Specimen 1 after test; C. Specimen 2 before test; D. Specimen 2 after test.

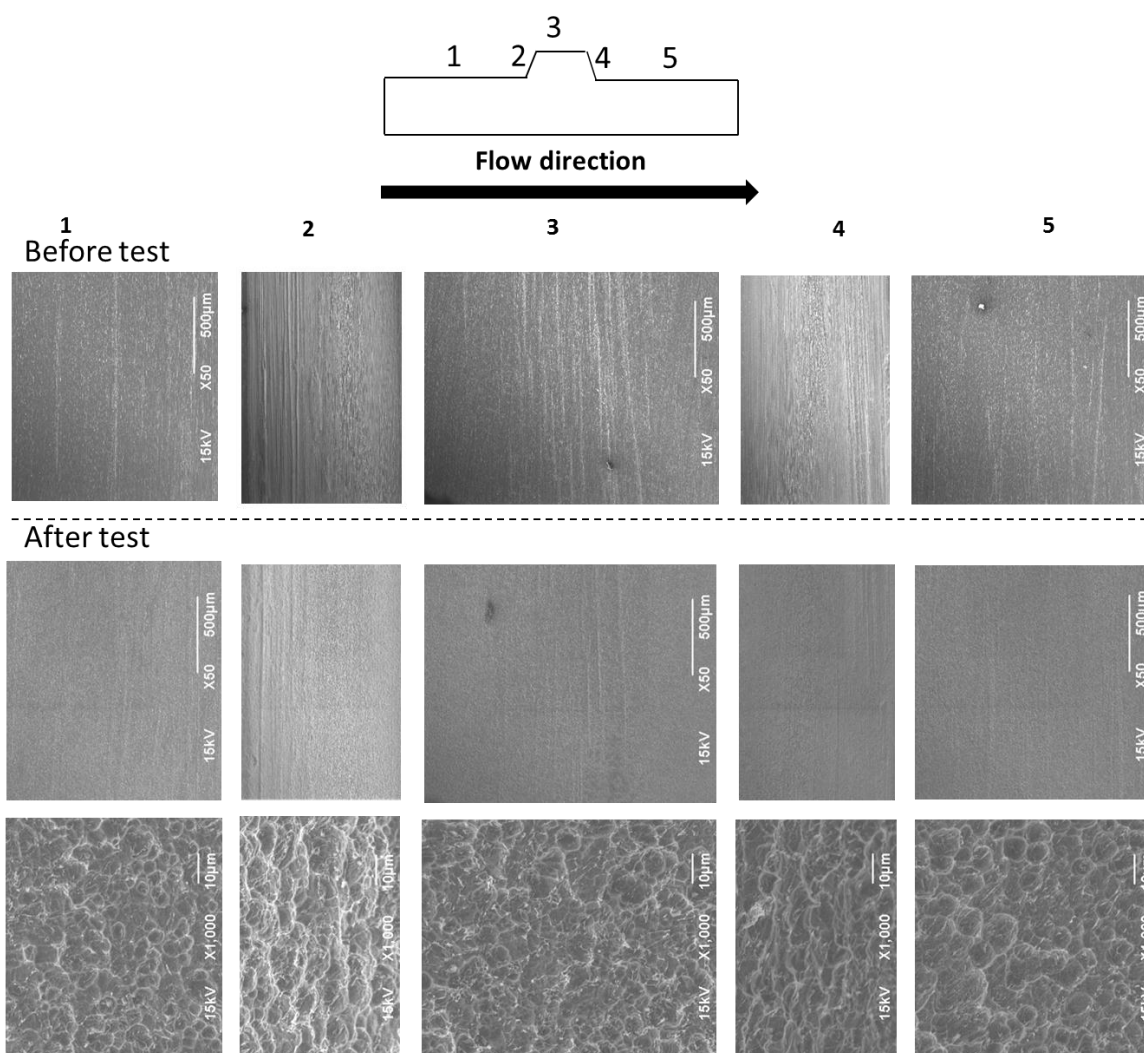


Figure 6-33: SEM images of protrusion Specimen 3. Before test: 1st row at 50X magnification. After test: 2nd row at 50X magnification; 3rd row at 1000X magnification. Physical locations are defined by using 5 numbered individual regions in Figure 6-2. 1 wt.% NaCl, pH 5, 0.97 bar CO<sub>2</sub>, 25°C, 720 ppm<sub>v</sub> inhibitor, 16 m/s, 4 day test duration, X65, O<sub>2</sub> < 2 ppb.

The chemical composition of flat and protrusion specimens before and after the test was analyzed by EDS, as shown in Figure 6-34 and Figure 6-35, respectively. The results suggest that the flat and protrusion specimens were under a similar type of uniform corrosion attack and there was no formation of corrosion product layers.

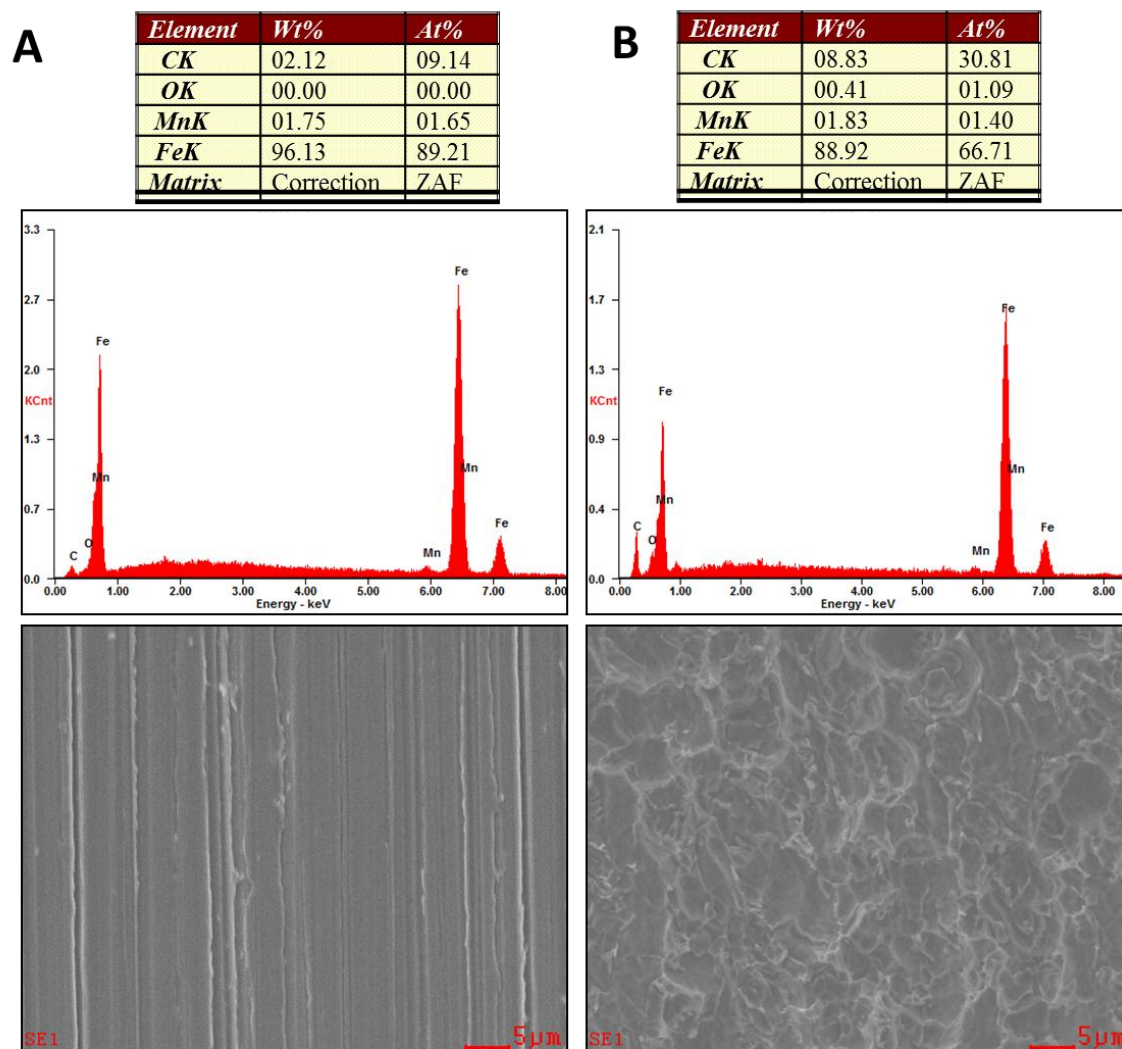


Figure 6-34: EDS analysis of flat Specimen 1 (600 grit finish). A: before experiment; B: after experiment. 1 wt.% NaCl, pH 5, 0.97 bar CO<sub>2</sub>, 25°C, 720 ppm<sub>v</sub> inhibitor, 16 m/s, 4 day test duration, X65, O<sub>2</sub> < 2 ppb.

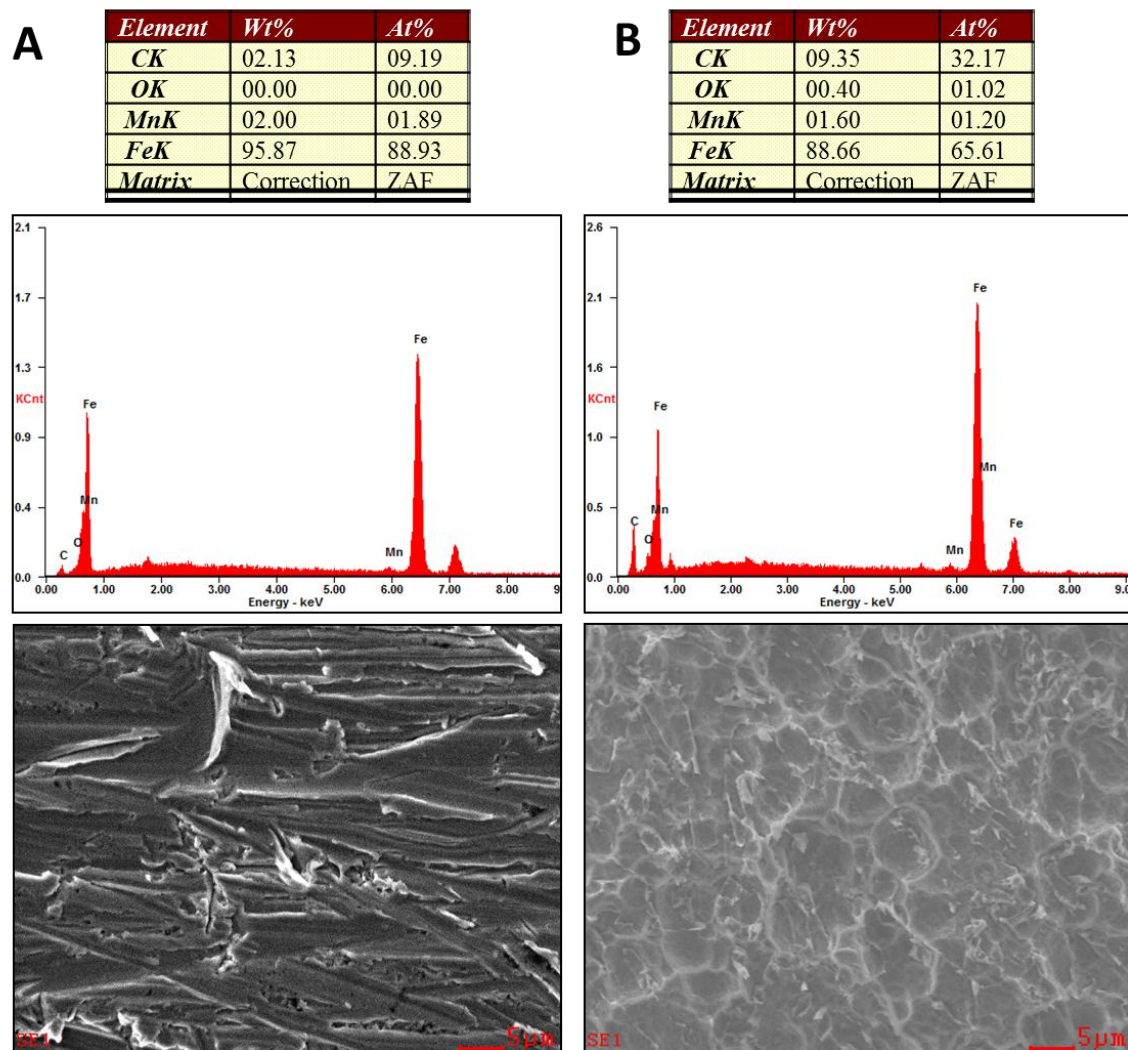


Figure 6-35: EDS analysis of protrusion Specimen 3. A: before experiment; B: after experiment, at the top of protrusion, region 3 in Figure 6-2. 1 wt.% NaCl, pH 5, 0.97 bar CO<sub>2</sub>, 25°C, 720 ppm<sub>v</sub> inhibitor, 16 m/s, 4 day test duration, X65, O<sub>2</sub> < 2 ppb.

All the experimental results in this series of tests demonstrate that with an excess amount of inhibitor, the localized corrosion was mitigated even in the presence of cavitation.

### *6.3.6.2 Effect of turbulence reduction due to inhibitors*

It has been reported in the literature that excess inhibitor can form rod-like micelles and directly interact with small turbulence vortices in the near wall region and reduce the turbulence of the system [99]. To explain the mitigation of localized corrosion, it was hypothesized that excess inhibitor could significantly reduce the pressure drop along the TCFC and thereby eliminate cavitation. An additional series of test on the TCFC was conducted to evaluate the effect of inhibitor concentration on the flow turbulence by measuring the pressure drop across the thin channel. Figure 6-36 shows the pressure drop results between port 3 and port 4 in the TCFC (as shown in Figure 6-4) measured by a differential pressure transducer. No significant difference was observed for pressure drop measurements across the TCFC when using various inhibitor concentrations from 0 to 720 ppm<sub>v</sub> with both low and high flow velocities. Thus, the turbulence reducing effect of excess inhibitor was not the cause for the mitigation of localized corrosion under cavitation.

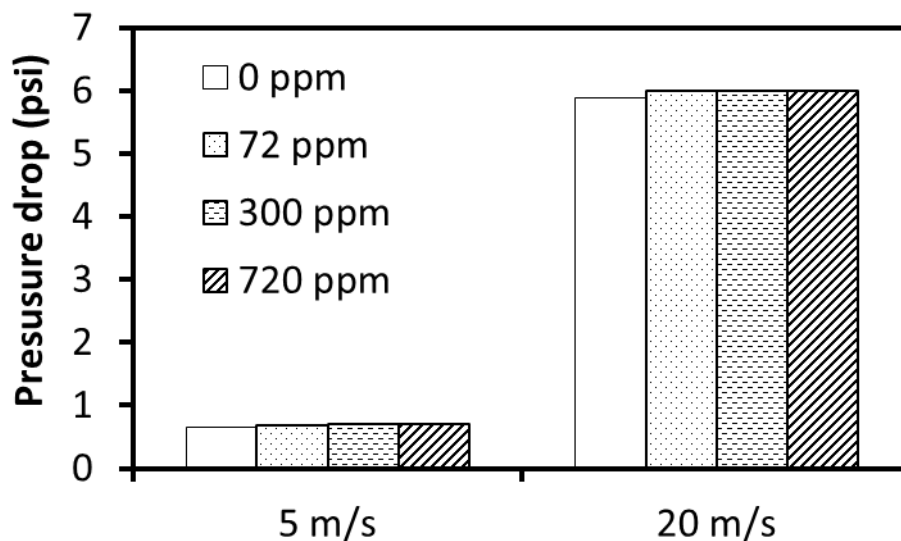


Figure 6-36: Pressure drop measurements between port 3 and port 4 in the TCFC with various inhibitor concentrations. 1 wt.% NaCl, pH 5, 0.97 bar CO<sub>2</sub>, 25°C.

So far, without a doubt, it was found that cavitation led to inhibitor failure at 72 ppm<sub>v</sub> and caused pitting corrosion, while this did not happen by using 720 ppm<sub>v</sub> of the same inhibitor under the same experimental conditions. The mechanism related to this phenomenon is discussed in the next section.

#### 6.4 Discussion

In this work, it was found that the WSS of the order of 10<sup>3</sup> Pa introduced by the highly turbulent single phase flow with a locally disturbed flow by a surface protrusion was unable to affect the corrosion inhibitor adsorption/desorption process on a steel surface. This is in line with other authors' experimental observations [17] and calculations that a much higher stress or energy would be needed to disrupt the inhibitor films adsorbed on a steel surface [22].

#### *6.4.1 Effect of pre-corrosion on corrosion inhibition at high flow velocity*

Different surface polishing treatments on the steel surface did not influence the inhibitor performance as evidenced by similar corrosion behaviors of Specimen 1 (600 grit sand paper polished) and Specimen 2 (150 grit sand paper polished). This was due to the pre-corrosion procedure during the experiments. In order to obtain a stable blank corrosion rate before an addition of inhibitor, the pre-corrosion periods were generally 10 to 12 hours in these tests. It was possible that a uniformly corroded steel surface was created in the presence of such a high flow velocity (high uniform corrosion rate) regardless of the initial surface polish. It has been reported that pre-corrosion on a steel surface generally impaired the inhibitor performance at relative low flow velocity (1 m/s) due to the formation of a cementite layer on the steel surface [100]. However, in the presented work, the detrimental effect of pre-corrosion due to the formation of a cementite layer was unlikely. This is because the formed cementite was probably mechanically removed by the high general WSS and local WSS fluctuations (order of  $10^3$  Pa).

#### *6.4.2 B value at high flow velocity*

In this study, weight loss and LPR measurements were used to determine the corrosion rates. The weight loss results gave an accurate time-averaged corrosion rate but with no indication of momentary corrosion rate changes when the inhibitor was added. LPR is a suitable technique for online corrosion rate monitoring and is capable of capturing the transients with the addition of an inhibitor. However, a suitable B value

needs to be determined in order to obtain correct instantaneous corrosion rates. A B value of 65 mV was used throughout the present tests for LPR corrosion rate calculation. The B value was calibrated through the blank test and was assumed unchanged after the addition of inhibitor. It is noted that this B value is much larger than the typical value in a CO<sub>2</sub> corrosion system (e.g., B= 26 mV). This is because the limiting current for H<sup>+</sup> reduction in the present study was drastically enhanced by the high flow velocity, which increased the cathodic reaction rate. It is found in the literature that the CO<sub>2</sub> corrosion rate at pH 5 is flow dependent due to the increase of mass transfer controlled H<sup>+</sup> reduction reaction [64]. The calculated large B value indicates that the cathodic reaction is to some extent controlled by the mass transfer process. The time-averaged corrosion rate that is calculated from the LPR technique by integrating the area underneath the corrosion rate – time curve are compared with the averaged corrosion rates calculated from weight losses of specimens, as shown in Figure 6-37. The corrosion rates are generally coherent except for the 720 ppm<sub>v</sub> test, where the corrosion rate from LPR is much larger than the weight loss corrosion rate. This discrepancy may be due to the measurement error from that individual test.

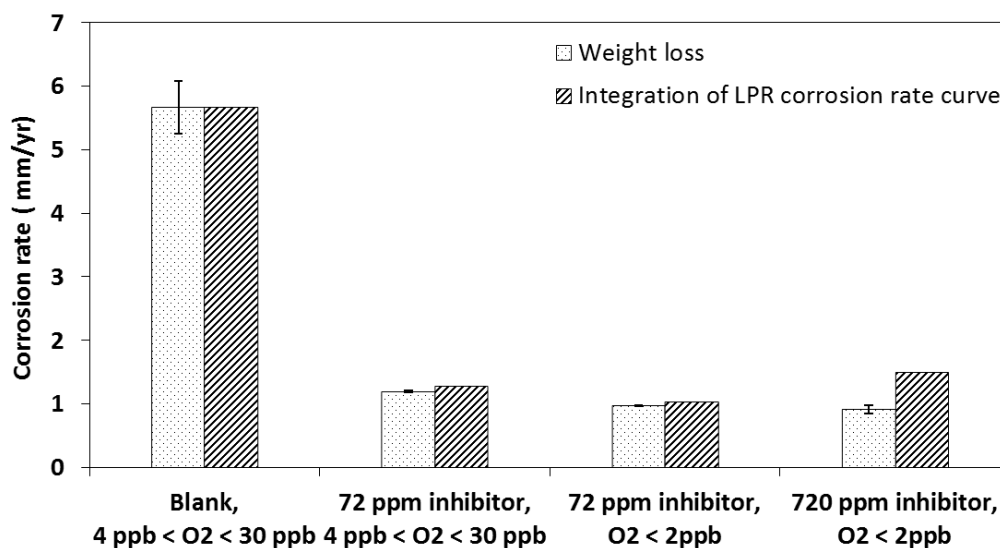


Figure 6-37: Corrosion rates calculated from averaged weight losses of specimens and from LPR corrosion rate curves with  $B = 65$  mV. 1 wt.% NaCl, pH 5, 0.97 bar CO<sub>2</sub>, 25°C, 16 m/s, 4 day test duration, X65.

#### 6.4.3 Mechanisms of flow cavitation induced pitting corrosion and its mitigation

##### 6.4.3.1 Effects of flow on inhibitor adsorption / desorption equilibrium

In this research, it was found that pitting corrosion occurred at the leading edge and at the top of the protrusion in the presence of 72 ppm<sub>v</sub> inhibitor with local flow velocities up to 28 m/s. With an excess amount of inhibitor (720 ppm<sub>v</sub>), this pitting corrosion was mitigated under the same environmental and flow conditions. The pitting corrosion was determined to be caused by local flow cavitation using experimental and computational evidence. However, the effect of inhibitor concentration on the mitigation of this cavitation induced pitting corrosion is not yet clear. Unlike the mechanical removal of a solid corrosion product layer by high hydrodynamic stresses produced by flow, the interactions between flow stresses and inhibitor films are less straightforward. As discussed, the collapsed cavitation bubbles may generate significantly high stresses that

locally remove inhibitor molecules from the steel surface. The mechanical impacts of collapsing bubbles onto a surface can reach MPa, even GPa magnitude [101,102]. Undoubtedly, this stress exceeds the adhesion strength of the inhibitor films to the steel surface and mechanical removal of inhibitor is expected. However, the inhibitor adsorption / desorption process on a steel surface is not static, but is considered to be in a dynamic equilibrium. The adsorption kinetics of inhibitors is usually fast, especially in this highly turbulent flow where the mass transfer is significantly enhanced. It is not easy to interpret why the inhibitors on the steel surface, which were mechanically removed by flow, were not replenished by the remaining inhibitors readily available in the bulk solution. Instead of a standpoint derived from flow hydrodynamics, it may be useful to discuss the flow effects on corrosion inhibition in relation to adsorption / desorption reaction equilibria.

Experimental results from various researchers suggest that the adsorption of imidazoline-type inhibitors follows the Langmuir adsorption model [4,93,103,104]. Thus, the adsorption and desorption rates of the inhibitor ( $R_{ads}$  and  $R_{des}$ ) are simply written as:

$$R_{ads} = k_{ads}(1 - \theta)c_{inhib}^b \quad (6-4)$$

$$R_{des} = k_{des}\theta \quad (6-5)$$

where  $k_{ads}$  and  $k_{des}$  are the reaction rate constants for adsorption and desorption processes, respectively;  $c_{inhib}^b$  is the inhibitor concentrations in the bulk;  $\theta$  is the surface coverage of inhibitor ( $0 < \theta < 1$ ). At equilibrium, the adsorption and desorption rates should be equal, which yields:

$$k_{ads}(1 - \theta)c_{inhib}^b = k_{des}\theta \quad (6-6)$$

Rearrangement of Equation (6-6) for a single equilibrium constant results in:

$$\left(\frac{1}{\theta} - 1\right) c_{inhib}^b = \frac{1}{K} \quad (6-7)$$

where  $K$  is the inhibitor adsorption equilibrium constant, defined as:

$$K = \frac{k_{ads}}{k_{des}} \quad (6-8)$$

The explanation for a series of small pits found along the leading edge of the protrusion specimen is straightforward. As discussed in previous sections, formation of cavitation bubbles at this location created large areas of gas-liquid interface and consumed a fraction of the inhibitors which are amphiphilic and tend to aggregate at any available interface. This led to a local depletion of inhibitor and caused localized corrosion due to the incomplete inhibitor coverage on the steel surface. Consideration from the view of adsorption / desorption reaction equilibria draws the same conclusion. From Equation (6-7), if the bulk concentration of inhibitor ( $c_{inhib}^b$ ) is reduced due to the consumption by cavitation bubbles, and if the adsorption equilibrium constant ( $K$ ) remains unchanged, the only way to hold the balance in this equation is to have a decreasing surface coverage of inhibitor ( $\theta$ ), which results in a local depletion of inhibitor.

In the present research, the majority of pits were found at the top of the protrusion region, where the cavitation bubble implosions presumably occurred. Bubble collapses at the top of the protrusion are supported by fundamental calculations. The streamwise length at the top of the protrusion region is approximately 4 mm. When assuming that the bubbles obtain the streamwise core flow velocity of 25 m/s (Figure 6-24), the time for

bubbles to travel across the top of the protrusion region would be approximately 160  $\mu\text{s}$ . This is generally coherent with findings in the literature that the collapse time of cavitation bubbles vary from 100  $\mu\text{s}$  to a few ms [102,105,106]. Thus, bubble collapses on top of the protrusion would occur, as also were corroborated by the present experimental results.

The dynamics of cavitation bubbles near a solid wall have been extensively researched [101,102,107–109]. During bubble collapses, the potential energy of vaporous bubbles is converted into mechanical energy (including shock waves), heat, chemical energy, sound and light emissions [101,110]. It is assumed that the energy releases in various forms during bubble collapses negatively affect the inhibitor adsorption equilibrium constant ( $K$ ) by enhancing the desorption reaction (increasing the  $k_{des}$ ), which results in a decreasing surface coverage of inhibitor according to Equation (6-7).

As discussed, the high mechanical stresses generated by collapsing bubbles can directly remove the adsorbed inhibitors on the steel surface, which essentially facilitates the desorption reaction. Because of that, the overall inhibitor adsorption equilibrium would shift to the direction of desorption reaction, leading to the local depletion of inhibitor and localized corrosion.

Besides the high magnitude of mechanical energy, collapsing cavitation bubbles can also release an enormous amount of heat (thermal energy) and even emit light [111–113]. The temperature surrounding the collapsing cavitation bubbles can reach several thousands of Kelvins (K) [110,114]. It is also possible that some of the released heat is also transferred to the steel surface, resulting in local temperature increase. It is found in

the literature that the desorption reaction of imidazoline-type inhibitors is favorable when the surface temperature increases [4,103,115]. From Equation (6-7), if the  $K$  decreases and the bulk concentration of inhibitor remains the same, the surface coverage has to decrease to balance this equation.

#### *6.4.3.2 Energy consideration in the thin channel flow cell system*

As mentioned earlier, it is assumed that the flow can negatively affect the inhibitor adsorption/desorption reaction equilibrium by enhancing the desorption reaction rate. Several forms of energy are involved in this process and are discussed below.

The reaction equilibrium is controlled by the chemical thermodynamics. A vast amount of research has been conducted focusing on the thermodynamic properties of inhibitor adsorption reactions. For example, it has been generally accepted that the standard free energy change due to surfactant inhibitor adsorption reaction ( $\Delta_{rxn}G^{\circ}$ ) is approximately -40 kJ to -20 kJ per mole of adsorbed inhibitors [116,117], which suggests that the adsorption reaction is thermodynamically favored at standard conditions.

The reaction rate of inhibitor adsorption is controlled by the chemical kinetics. The kinetic activation energy of the inhibitor adsorption reaction ( $\Delta G_{ads}$ ) is estimated to be approximately  $19 \pm 2$  kJ per mole of inhibitor [118,119]. The relationship between the thermodynamic and kinetic energy changes due to the inhibitor adsorption/desorption process can be illustrated by an energy diagram (as shown in Figure 6-38). From this diagram, it can be seen that the desorption process has a much larger activation energy ( $\Delta G_{des}$ ) than the adsorption reaction. Obviously, if the flow would affect the inhibitor

desorption reaction rate, an energy input of the same magnitude as the desorption kinetic activation energy should be provided.

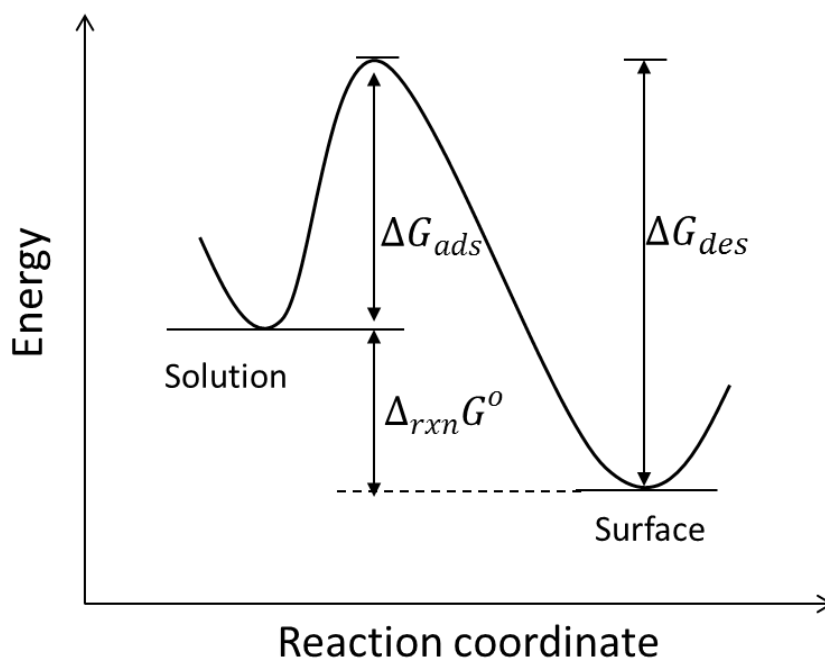


Figure 6-38: Energy diagram of inhibitor adsorption/desorption reactions.

An energy analysis in the TCFC system has therefore been conducted to examine if the flow can provide sufficient energy input.

The thermal (kinetic) energy of the system on the molecular level can be written as:

$$E_t = \frac{3}{2} kT \quad (6-9)$$

where  $k$  is the Boltzmann constant ( $1.38 \times 10^{-23}$  J/K) and  $T$  is absolute temperature (K).

When calculating the thermal energy ( $E_t'$ ) on a molar basis, it yields:

$$E_t' = \frac{3}{2} RT \quad (6-10)$$

where  $R$  is the gas constant (8.314 J/K·mole).

Besides random motions of the molecules, there is also an ordered directional movement of the liquid molecules in a flow system, referred to as the bulk flow velocity.

The additional kinetic energy ( $E_k$ ) due to the directional flow can be written as:

$$E_k = \frac{1}{2}mv^2 \quad (6-11)$$

where  $m$  is the molar mass of the liquid molecules (kg/mole); and  $v$  is the flow velocity (m/s).

The bulk temperature in the TCFC was 298 K, while the flow stream velocity on the top of the protrusion was 25 m/s (Figure 6-24). According to Equation (6-10) and (6-11), the thermal energy and flow kinetic energy are calculated to be 3.7 kJ and 5.6 J per mole of water, respectively.

The Langmuir adsorption of inhibitor is essentially the displacement of adsorbed water molecules at the steel surface, as given by [120]:



Because the stoichiometric coefficients for all substances in this reaction are equal, the molar energies of inhibitor adsorption and water flow can be directly comparable. It shows that the energy level of the bulk flow kinetic energy (only several J/mole) is several orders of magnitude smaller than the adsorption/desorption activation energies (several kJ/mole). It may be therefore concluded that the energy due to bulk flow in the TCFC (e.g., wall shear stress) could not affect the inhibitor adsorption/desorption process.

Although bulk flow seems unable to provide enough energy to affect inhibitor adsorption/desorption processes, the collapses of cavitating bubbles in the TCFC may do so. The total potential energy by a single spherical cavitation bubble is given by [102]:

$$E_p = \frac{4}{3}\pi r^3(P_\infty - P_v) \quad (6-13)$$

where  $P_\infty$  is the ambient pressure at infinite distance;  $P_v$  is the vapor pressure of the liquid;  $r$  is the bubble radius; and  $E_p$  is the bubble potential energy. The potential energy on a molar basis may be written as:

$$E_p' = \frac{m}{\rho_v}(P_\infty - P_v) \quad (6-14)$$

where  $m$  is the molar mass of the liquid (kg/mole); and  $\rho_v$  is the vapor density of the liquid (kg/m<sup>3</sup>). At 298 K, the vapor pressure and vapor density of water are 3200 Pa and 0.024 kg/m<sup>3</sup> (ideal gas law), respectively. The ambient pressure at infinite distance in the TCFC is  $1 \times 10^5$  Pa. Consequently, the bubble potential energy is calculated to be 72.6 kJ per mole of water vapor, which is much larger than the energy levels of inhibitor adsorption reactions.

The collapsing cavitation bubbles with their various forms of energy releases, particularly the mechanical energy release, undoubtedly reach the magnitude of the inhibitor desorption activation energy. It is therefore proposed that the desorption activation energy is decreased as the surface energy level is increased due to the energy input from collapsing cavitation bubbles (shown in Figure 6-39).

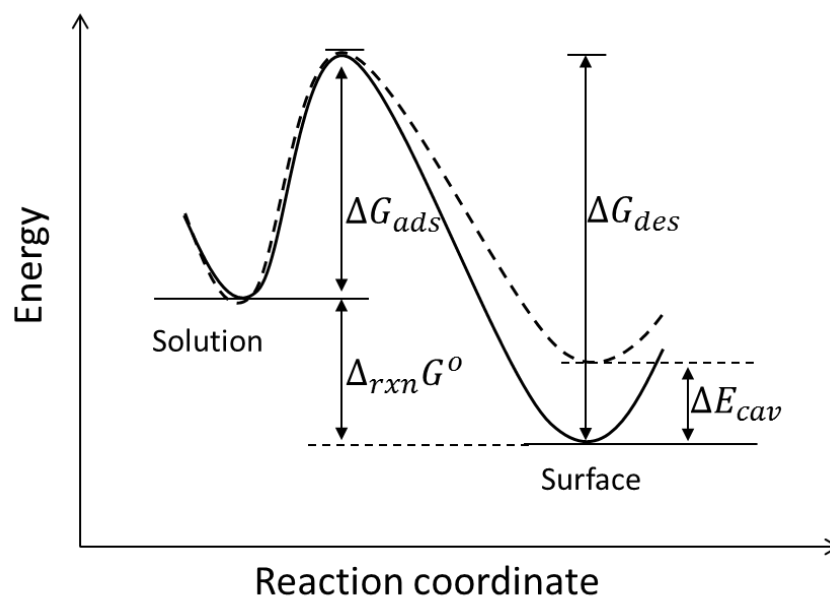


Figure 6-39: Energy diagram of inhibitor adsorption/desorption reactions with the additional energy due to collapsing cavitation bubbles.

The relationship between the kinetic activation energies and the reaction rate constants can be calculated by the Arrhenius equation [121,122]. Consequently, the original reaction rate constants without the effect of cavitation energy can be written as:

$$k_{ads} = Ae^{\left(-\frac{\Delta G_{ads}}{RT}\right)} \quad (6-15)$$

$$k_{des} = Be^{\left(-\frac{\Delta G_{des}}{RT}\right)} \quad (6-16)$$

where  $A$  and  $B$  are the pre-exponential factors for adsorption and desorption reactions, respectively. In addition, the new reaction rate constants with the effect of cavitation energy input can be written as:

$$k_{ads}' = Ae^{\left(-\frac{\Delta G_{ads}}{RT}\right)} \quad (6-17)$$

$$k_{des}' = Be^{\left[-\frac{(\Delta G_{des} - E_{cav})}{RT}\right]} \quad (6-18)$$

where  $E_{cav}$  is the energy input due to collapsing cavitation bubbles. When substituting these reaction rate constants into Equation (6-8), it reveals that the adsorption/desorption reaction equilibrium shifts to the direction of desorption reaction ( $K' < K$ ). According to Equation (6-7), when the equilibrium constant decreases and the bulk inhibitor concentration is unchanged, the surface coverage of inhibitor has to decrease, which explains the inhibitor failure at 72 ppm<sub>v</sub>.

From the energy analysis, a same postulate can be made that the bulk flow seen in typical systems is very unlikely to affect the inhibitor adsorption/desorption process. However, the physical effects of collapses of cavitation bubbles, e.g., releases of high magnitude mechanical energy and thermal energy, may influence the inhibitor adsorption/desorption equilibrium.

#### *6.4.3.3 Mitigation of cavitation induced localized corrosion*

It has been shown above that collapsing cavitation bubbles affect the inhibitor adsorption/desorption equilibrium by facilitating the desorption process, which leads to a decreasing coverage of inhibitor on the steel surface and induces localized corrosion. From Equation (6-7), a higher bulk concentration of inhibitor ( $c_{inhib}^b$ ) would be required in order to maintain a sufficient surface coverage of inhibitor and mitigate the localized corrosion. This was corroborated by the experimental results that an excess amount of inhibitor (720 ppm<sub>v</sub>) mitigated the cavitation induced localized corrosion at the protrusion.

In a nutshell, collapsing cavitation bubbles disrupt the original inhibitor adsorption/desorption equilibrium by enhancing the desorption process, which results in a decreasing surface coverage of inhibitor. Excess inhibitor reverses this situation by enhancing the inhibitor adsorption process and thereby mitigates cavitation induced localized corrosion.

#### *6.4.4 Microscopic expressions for continuum hydrodynamics*

The present study shows that some flow conditions can mechanically affect the inhibitor adsorption/desorption equilibrium by hydrodynamic stresses, e.g., impacts of shock waves due to cavitation bubble implosions. However, the link between bulk flow hydrodynamics and inhibitor behaviors on the surface is not yet established. The inhibitor adsorption/desorption process occurs at molecular length scales (order of nm), which are much smaller than the spatial resolution of continuum hydrodynamics. A means to connect the macroscopic and molecular hydrodynamics is crucial in order to interpret the interactions between bulk flow and inhibitor molecules. Fortunately, such a bridge has already been built, for example, by molecular dynamics simulation (MD) [123,124].

In molecular dynamics simulation, the movements of individual molecules in the simulated system are governed by prescribed intermolecular potentials. The time evolution of the system is obtained by solving Newton's equations of motion for all the molecules [123]. By averaging the quantities of molecules, such as their trajectories and intermolecular potentials, the continuum hydrodynamic properties may be obtained

[124]. For example, the microscopic expression of the shear stress tensor may be given by [123]:

$$\tau_{xy} = \frac{1}{V} \left[ \sum_i m(v_{xi} - \bar{v}_x)(v_{yi} - \bar{v}_y) + \frac{1}{2} \sum_{i=1}^N \sum_{j \neq i=1}^N x_{ij} \frac{\partial u(\mathbf{r}_{ij})}{\partial y_{ij}} \right] \quad (6-19)$$

where  $\mathbf{r}_{ij}$  is the trajectory between molecule  $i$  and  $j$ ;  $u$  is the intermolecular potential;  $x_{ij}$  and  $y_{ij}$  are projections of  $\mathbf{r}_{ij}$  in x and y directions;  $v_{xi}$  and  $v_{yi}$  are velocities of molecule  $i$  in x and y directions;  $\bar{v}_x$  and  $\bar{v}_y$  are the averaged velocities of all molecules in x and y directions;  $m$  is the mass of molecule; and  $V$  is the volume of the simulated system.

Molecular dynamics simulation bridges the gap between measured macroscopic hydrodynamic quantities and the motions of individual molecules beneath the length and time scales of continuum fluid mechanics. Therefore, molecular dynamics simulation can be used for future research as a diagnostic tool to investigate the effects of bulk flow on inhibitor adsorption/desorption processes.

## 6.5 Summary

Mechanical removal of inhibitor by flow cavitation was confirmed. Based on the presented results and discussion, the findings can be summarized as:

- Specimens protruded into the flow stream drastically changed the local hydrodynamic conditions and caused cavitation in a highly turbulent flow system.
- The protrusion led to a local wall shear stress up to 4.8 kPa in the studied flow conditions. However, an effect of wall shear stress on the inhibitor adsorption/desorption process was not observed. This is because the wall shear

stress, even in “extreme” flow conditions, is several orders of magnitude lower than the adhesion strength of inhibitor films to the steel surface.

- The inhibitor adsorption/desorption equilibrium was significantly influenced by the collapsing cavitation bubbles, which enhanced the inhibitor desorption process, reduced the surface coverage of inhibitor, and caused localized corrosion due to local inhibitor depletion.
- An excess amount of inhibitor eliminated the cavitation induced localized corrosion by establishing a new adsorption/desorption equilibrium and maintaining a sufficient surface coverage of inhibitor.

## Chapter 7: Conclusions and Recommendations

### 7.1 Conclusions

In the research reported in this dissertation, the mechanical effects of flow on CO<sub>2</sub> corrosion inhibition of carbon steel pipelines have been investigated. The experimental studies mainly focused on two main topics: hydrodynamics relating to wall shear stress measurement in flow pipelines encountered CO<sub>2</sub> corrosion problems and failure of corrosion inhibition due to mechanical effects of extremely turbulent flow. Several conclusions based on the present research can be drawn:

- The floating element method was successful in directly measuring wall shear stress in the studied flow, which provides a new means for building better understanding of complex multiphase flow.
- In the studied multiphase flow patterns at ambient conditions, the highest wall shear stress occurred in the slug flow pattern on the top of the pipe when the slug front passed with the maximum in situ flow velocity.
- The maximum wall shear stress in slug flow can be evaluated by current flow modeling when a proper resolution of the local flow velocity profile is achieved.
- The maximum shear stress value was about 2 to 4 times higher than the calculated mean shear stress of the slug body using mixture velocity. This can serve as a guideline for improving slug flow modeling with applications to other areas, such as removal of corrosion inhibitor films and corrosion product layers.
- In the studied flow at ambient conditions, the maximum wall shear stress value for any horizontal two-phase flow pattern was of an order of 100 Pa, the value for

single-phase liquid flow did not exceed 1000 Pa. These stress values are several orders of magnitude lower than the reported adhesion strength of inhibitor films or  $\text{FeCO}_3$  layers. This suggests that mechanical removal of these films or layers solely by wall shear stress typically seen in flow lines is very unlikely.

- Results from corrosion inhibitor experiments and flow simulations at high flow velocity conditions confirmed that a local wall shear stress up to 4.8 kPa could not affect the protectiveness of corrosion inhibitor films on the steel surface.
- A flow disturbance caused by surface protrusion significantly changed the local hydrodynamics and caused flow cavitation at a high flow velocity.
- In laboratory experiments, flow cavitation was identified as being able to mechanically affect corrosion inhibitor films and cause localized corrosion.
- The inhibitor adsorption/desorption equilibrium was significantly influenced by the collapsing cavitation bubbles, which generated a mechanical stress that exceeds the magnitude of the adhesion strength of inhibitor, enhanced the inhibitor desorption process, and caused localized corrosion due to local inhibitor depletion.
- An excess amount of inhibitor eliminated the cavitation induced localized corrosion by establishing a new adsorption/desorption equilibrium and maintaining a high surface coverage of inhibitor.

## 7.2 Recommendations

This dissertation focuses on the hydrodynamics of extremely turbulent flow and the mechanical interactions between flow and CO<sub>2</sub> corrosion inhibition, both of which are complex. Although most of the initial research questions have been answered, some other aspects related to these topics have been identified in the present research, and should be taken into account for further investigation. Some recommendations are given below:

- The floating element probe provides direct and accurate measurements of wall shear stress fluctuations of relatively large time scale transients in single-phase and multiphase flow, e.g, the passage of slugs. However, a floating element probe with both high temporal and spatial resolutions may be necessary in order to investigate the local wall shear stress fluctuations due to the smallest turbulent eddies.
- The present research shows that a proper resolution of the flow field is essential for building understanding of multiphase flow, including evaluation of wall shear stress. Future research may focus on obtaining the complete flow velocity profile in multiphase flow patterns through experiments and/or computational simulations.
- Although a number of different multiphase flow patterns have been studied in the present research, some specific flow conditions found in the field, involving a discrete phase, were not covered. For example, entrained liquid droplets in annular-mist flow, that travel at high gas velocities, can lead to high energy wall impacts (high local mechanical stresses), particularly at locations of disturbed

flow, such as bends, valves, tees, weld beads, etc. A proper evaluation of the mechanical stresses during the impacts through experimental research or numerical simulation would be needed to assess the mechanical effect of discrete phases on corrosion inhibition.

- The present experimental research undoubtedly demonstrates that some flow conditions can mechanically affect inhibitor adsorption/desorption equilibria. However, the link between the macroscopic flow behavior and the microscopic inhibitor adsorption/desorption process is not fully understood. Future investigation may use computer simulation approaches, for example, such as molecular dynamics simulation, in order to connect the macroscopic laboratory experiments to the microscopic behaviors of inhibitor molecules.

## References

- [1] U.S. Liquids Pipeline Usage & Mileage Report, Association of Oil Pipe Lines (AOPL) and American Petroleum Institute (API), November 2015.
- [2] S. Netic, W. Sun, Corrosion in acid gas Solutions, in: J.A. Richardson, et al. (Eds.), Shreir's Corrosion, Elsevier, Amsterdam, The Netherlands, 2010, pp. 1270–1298.
- [3] S. Netic, Carbon dioxide corrosion of mild steel, in: R. Winston Revie (Ed.), Uhlig's Corrosion Handbook, third ed., John Wiley & Sons, Inc., Hoboken, New Jersey, 2011, pp. 229–245.
- [4] S. Ramachandran, B.-L. Tsai, M. Blanco, H. Chen, Y. Tang, W.A. Goddard III, Self-assembled monolayer mechanism for corrosion inhibition of iron by imidazolines, *Langmuir* 12 (1996) 6419–6428.
- [5] T. Li, Y. Yang, K. Gao, M. Lu, Mechanism of protective film formation during CO<sub>2</sub> corrosion of X65 pipeline steel, *J. Univ. Sci. Technol. Beijing* 15 (2008) 702–706.
- [6] W. Li, B. Brown, D. Young, S. Netic, Investigation of pseudo-passivation of mild steel in CO<sub>2</sub> corrosion, *Corrosion* 70 (2014) 294–302.
- [7] J. Zhang, Z.L. Wang, Z.M. Wang, X. Han, Chemical analysis of the initial corrosion layer on pipeline steels in simulated CO<sub>2</sub>-enhanced oil recovery brines, *Corros. Sci.* 65 (2012) 397–404.
- [8] J. Han, D. Young, H. Colijn, A. Tripathi, S. Netic, Chemistry and structure of the passive film on mild steel in CO<sub>2</sub> corrosion environments, *Ind. Eng. Chem. Res.* 48 (2009) 6296–6302.

- [9] R.H. Hausler, G. Schmitt, Hydrodynamic and flow effects on corrosion inhibition, in: NACE International CORROSION 2004 conference, 2004, paper no. 04402.
- [10] S. Nestic, Effects of multiphase flow on internal CO<sub>2</sub> corrosion of mild steel pipelines, *Energy Fuels* 26 (2012) 4098–4111.
- [11] K. Gao, F. Yu, X. Pang, G. Zhang, L. Qiao, W. Chu, M. Lu, Mechanical properties of CO<sub>2</sub> corrosion product scales and their relationship to corrosion rates, *Corros. Sci.* 50 (2008) 2796–2803.
- [12] V. Ruzic, M. Veidt, S. Nestic, Protective iron carbonate films – part 1: mechanical removal in single-phase aqueous flow, *Corrosion*. 62 (2006) 419–432.
- [13] G. Schmitt, M. Mueller, Critical wall shear stresses in CO<sub>2</sub> corrosion of carbon steel, in: NACE International CORROSION 99 conference, 1999, paper no. 44.
- [14] B.F.M. Pots, E.L.J.A. Hendriksen, H.A.M. de Reus, H.B. Pit, S.J. Paterson, Field study of corrosion inhibition at very high flow velocity, in: NACE International CORROSION 2003 conference, 2003, paper no. 03321.
- [15] B. Poulson, Advances in understanding hydrodynamic effects on corrosion, *Corros. Sci.* 35 (1993) 655–665.
- [16] S. Seal, K. Sapre, A. Kale, V. Desai, M. Gopal, P. Jepson, Effect of multiphase flow on corrosion of C-steel in presence of inhibitor: a surface morphological and chemical study, *Corros. Sci.* 42 (2000) 1623–1634.
- [17] E. Gulbrandsen, A. Grana, Testing of carbon dioxide corrosion inhibitor performance at high flow velocities in jet impingement geometry. Effects of mass transfer and flow forces, *Corrosion* 63 (2007) 1009–1020.
- [18] F. Farelas, Thin channel flow cell study: mechanical and chemical removal of FeCO<sub>3</sub> scales in carbon steel, CCJIP Advisory Board Meeting, Institute for Corrosion and Multiphase Technology, Ohio Univ., Athens, OH, November 2008.

- [19] Y. Yang, B. Brown, S. Netic, M. Elena Gennaro, B. Molinas, Mechanical strength and removal of a protective iron carbonate layer formed on mild steel in CO<sub>2</sub> corrosion, in: NACE International CORROSION 2010 conference, 2010, paper no. 10383.
- [20] J. Huang, B. Brown, S. Netic, Localized corrosion of mild steel under silica deposits in inhibited aqueous CO<sub>2</sub> solutions, in: NACE International CORROSION 2013 conference, 2013, paper no. 2144.
- [21] J.R. Shadley, S.A. Shirazi, E. Dayalan, E.F. Rybicki, Prediction of erosion-corrosion penetration rate in a carbon dioxide environment with sand, *Corrosion* 54 (1998) 972–978.
- [22] Y. Xiong, B. Brown, B. Kinsella, S. Netic, A. Pailleret, Atomic force microscopy study of the adsorption of surfactant corrosion inhibitor films, *Corrosion* 70 (2014) 247–260.
- [23] G. Schmitt, C. Bosch, P. Plagemann, K. Moeller, Local wall shear stress gradients in the slug flow regime – Effects of hydrocarbon and corrosion inhibitor, in: NACE International CORROSION 2002 conference, 2002, paper no. 02244.
- [24] V.E. Nakoryakov, O.N. Kashinsky, A.P. Burdukov, V.P. Odnoral, Local characteristics of upward gas-liquid flows, *Int. J. Multiphase Flow* 7 (1981) 63–81.
- [25] H. Wang, T. Hong, J.Y. Cai, W.P. Jepson, C. Bosch, Enhanced mass transfer and wall shear stress in multiphase slug flow, in: NACE International CORROSION 2002 conference, 2002, paper no. 02501.
- [26] T.K. Villiger, M. Morbidelli, M. Soos, Experimental determination of maximum effective hydrodynamic stress in multiphase flow using shear sensitive aggregates, *AIChE J.* 61 (2015) 1735–1744.

- [27] D. Zheng, D. Che, Y. Liu, Experimental investigation on gas-liquid two-phase slug flow enhanced carbon dioxide corrosion in vertical upward pipeline, *Corros. Sci.* 50 (2008) 3005–3020.
- [28] J.W. Naughton, M. Sheplak, Modern developments in shear-stress measurement, *Prog. Aerospace Sci.* 38 (2002) 515–570.
- [29] T.J. Hanratty, J.A. Campbell, Measurement of wall shear stress, in: R.J. Goldstein (Ed.), *Fluid Mechanics Measurements*, second ed., Taylor & Francis, Washington, DC, 1996: pp. 575–649.
- [30] J.F. Kiefner, C.J. Trench, *Oil Pipeline Characteristics and Risk Factors: Illustrations from the Decade of Construction*, American Petroleum Institute (API), December 2001.
- [31] A. Danesh, *PVT and Phase Behaviour of Petroleum Reservoir Fluids*, Elsevier, Amsterdam, The Netherlands, 1998.
- [32] H.J. Herzog, What future for carbon capture and sequestration?, *Environ. Sci. Technol.* 35 (2001) 148A–153A.
- [33] J.C.M. Pires, F.G. Martins, M.C.M. Alvim-Ferraz, M. Simoes, Recent developments on carbon capture and storage: An overview, *Chem. Eng. Res. Des.* 89 (2011) 1446–1460.
- [34] S. Chu, Carbon capture and sequestration, *Science* 325 (2009) 1599.
- [35] H.J. Herzog, E.M. Drake, Carbon dioxide recovery and disposal from large energy systems, *Annu. Rev. Energy Environ.* 21 (1996) 145–166.
- [36] *Carbon Dioxide Enhanced Oil Recovery. Untapped Domestic Energy Supply and Long Term Carbon Storage Solution*, National Energy Technology Laboratory (NETL), U.S. Department of Energy, March 2010.

- [37] M.K. Verma, Fundamentals of Carbon Dioxide-Enhanced Oil Recovery (CO<sub>2</sub>-EOR) – A Supporting Document of the Assessment Methodology for Hydrocarbon Recovery Using CO<sub>2</sub>-EOR Associated with Carbon Sequestration, U.S. Geological Survey, Open-File Report 2015-1071, 2015.
- [38] J.P. Meyer, Summary of Carbon Dioxide Enhanced Oil Recovery (CO<sub>2</sub>EOR) Injection Well Technology, American Petroleum Institute (API), 2005.
- [39] M.B. Kermani, A. Morshed, Carbon dioxide corrosion in oil and gas production – A compendium, *Corrosion* 59 (2003) 659–683.
- [40] C. de Waard, D.E. Milliams, Carbonic acid corrosion of steel, *Corrosion* 31 (1975) 177–181.
- [41] L.G.S. Gray, B.G. Anderson, M.J. Danysh, P.R. Tremaine, Mechanisms of carbon steel corrosion in brines containing dissolved carbon dioxide at pH 4, in: NACE International CORROSION 89 conference, 1989, paper no. 464.
- [42] L.G.S. Gray, B.G. Anderson, M.J. Danysh, P.R. Tremaine, Effect of pH and temperature on the mechanism of carbon steel corrosion by aqueous carbon dioxide, in: NACE International CORROSION 90 conference, 1990, paper no. 40.
- [43] S. Netic, J. Postlethwaite, S. Olsen, An electrochemical model for prediction of corrosion of mild steel in aqueous carbon dioxide solutions, *Corrosion* 52 (1996) 280–294.
- [44] W. Sun, S. Netic, R.C. Woollam, The effect of temperature and ionic strength on iron carbonate (FeCO<sub>3</sub>) solubility limit, *Corros. Sci.* 51 (2009) 1273–1276.
- [45] E. Gulbrandsen, J.-H. Morard, J.-L. Crolet, Study of the possible mechanisms of steel passivation in CO<sub>2</sub> corrosion, in: NACE International CORROSION 99 conference, 1999, paper no. 624.

- [46] F.D. de Moraes, J.R. Shadley, J. Chen, E.F. Rybicki, Characterization of CO<sub>2</sub> corrosion product scales related to environmental conditions, in: NACE International CORROSION 2000 conference, 2000, paper no. 00030.
- [47] V.S. Sastri, Corrosion Inhibitors: Principles and Applications., John Wiley & Sons, Ltd, Chichester, England, 1998.
- [48] B. Sanyal, Organic compounds as corrosion inhibitors in different environments – A review, Prog. Org. Coatings 9 (1981) 165–236.
- [49] M.W. Ranney, Corrosion Inhibitor. Manufacture and Technology, Noyes Data Corporation, Park Ridge, New Jersey, 1976.
- [50] M.A. Migahed, A.M. Al-Sabagh, Beneficial role of surfactants as corrosion inhibitors in petroleum industry : a review article, Chem. Eng. Comm. 196 (2009) 1054–1075.
- [51] M.J. Rosen, Surfactants and Interfacial Phenomena, third ed., John Wiley & Sons, Inc., Hoboken, New Jersey, 2004.
- [52] R. Fuchs-Godec, Effects of surfactants and their mixtures on inhibition of the corrosion process of ferritic stainless steel, Electrochim. Acta 54 (2009) 2171–2179.
- [53] R. Zhang, P. Somasundaran, Advances in adsorption of surfactants and their mixtures at solid/solution interfaces, Adv. Colloid Interface Sci. 123-126 (2006) 213–229.
- [54] R. Atkin, Mechanism of cationic surfactant adsorption at the solid–aqueous interface, Adv. Colloid Interface Sci. 103 (2003) 219–304.
- [55] L.K. Koopal, E.M. Lee, M.R. Bohmer, Adsorption of cationic and anionic surfactants on charged metal oxide surfaces, J. Colloid Interface Sci. 170 (1995) 85–97.

- [56] P. Muller, Glossary of terms used in physical organic chemistry (IUPAC Recommendations 1994), *Pure Appl. Chem.* 66 (1994) 1077–1184.
- [57] D.A. Jones, *Principles and Prevention of Corrosion*, second ed., Prentice Hall, Upper Saddle River, NJ, 1996.
- [58] A. Edwards, C. Osborne, S. Webster, D. Klenerman, M. Joseph, P. Ostovar, M. Doyle, Mechanistic studies of the corrosion inhibitor oleic imidazoline, *Corros. Sci.* 36 (1994) 315–325.
- [59] J.A. Martin, F.W. Valone, The existence of imidazoline corrosion inhibitors, *Corrosion* 41 (1985) 281–287.
- [60] N. Pebere, M. Duprat, F. Dabosi, A. Lattes, A. de Savignac, Corrosion inhibition study of a carbon steel in acidic media containing hydrogen sulphide and organic surfactants, *J. Appl. Electrochem.* 18 (1988) 225–231.
- [61] A.J. McMahon, The mechanism of action of an oleic imidazoline based corrosion inhibitor for oilfield use, *Colloids Surf.* 59 (1991) 187–205.
- [62] O. Shoham, *Mechanistic Modeling of Gas-Liquid Two-Phase Flow in Pipes*, Society of Petroleum Engineers, Richardson, Texas, 2006.
- [63] S. Nestic, S. Wang, J. Cai, Y. Xiao, Integrated CO<sub>2</sub> corrosion - multiphase flow model, in: NACE International CORROSION 2004 conference, 2004, paper no. 04626.
- [64] S. Nestic, G.T. Solvi, J. Enerhaug, Comparison of the rotating cylinder and pipe flow tests for flow-sensitive carbon dioxide corrosion, *Corrosion* 51 (1995) 773–787.
- [65] L.P. Reiss, T.J. Hanratty, Measurement of instantaneous rates of mass transfer to a small sink on a wall, *AIChE J.* 8 (1962) 245–247.

- [66] G. Schmitt, C. Werner, M. Bakalli, Fluid mechanical interactions of turbulent flowing liquids with the wall – revisited with a new electrochemical tool, in: NACE International CORROSION 2005 conference, 2005, paper no. 05344.
- [67] Z. Zhang, D. Hinkson, M. Singer, H. Wang, S. Netic, A mechanistic model of top-of-the-line corrosion, *Corrosion* 63 (2007) 1051–1062.
- [68] K.G. Winter, An outline of the techniques available for the measurement of skin friction in turbulent boundary layers, *Prog. Aerospace Sci.* 18 (1977) 1–57.
- [69] L. Lofdahl, M. Gad-el-Hak, MEMS applications in turbulence and flow control, *Prog. Aerospace Sci.* 35 (1999) 101–203.
- [70] S. Tavoularis, *Measurement in Fluid Mechanics*, Cambridge University Press, New York, NY, 2005.
- [71] M.A. Schmidt, R.T. Howe, S.D. Senturia, J.H. Haritonidis, Design and calibration of a microfabricated floating-element shear-stress Sensor, *IEEE Trans. Electron. Dev.* 35 (1988) 750–757.
- [72] A. Padmanabhan, H. Goldberg, K.D. Breuer, M.A. Schmidt, A wafer-bonded floating-element shear stress microsensor with optical position sensing by photodiodes, *J. Microelectromech. Syst.* 5 (1996) 307–315.
- [73] J. Shajii, K.-Y. Ng, M.A. Schmidt, A microfabricated floating-element shear stress sensor using wafer-bonding technology, *J. Microelectromech. Syst.* 1 (1992) 89–94.
- [74] V.A. Sheverev, V. Stepaniuk, Shear stress measurement apparatus, United States patent no. US 8,276,463 B2, 2012.
- [75] H. Ludwig, W. Tillmann, Investigations of the Wall-Shearing Stress in Turbulent Boundary Layers, National Advisory Committee for Aeronautics, Technical Memorandum 1285, 1950.

- [76] W. Li, Y. Xiong, B. Brown, K.E. Kee, S. Netic, Measurement of wall shear stress in multiphase flow and its effect on protective  $\text{FeCO}_3$  corrosion product layer removal, in: NACE International CORROSION 2015 conference, 2015, paper no. 5922.
- [77] W. Li, B.F.M. Pots, B. Brown, K.E. Kee, S. Netic, A direct measurement of wall shear stress in multiphase flow – Is it an important parameter in  $\text{CO}_2$  corrosion of carbon steel pipelines?, *Corros. Sci.* <http://dx.doi.org/10.1016/j.corsci.2016.04.008>
- [78] V.C. Patel, M.R. Head, Some observations on skin friction and velocity profiles in fully developed pipe and channel flows, *J. Fluid Mech.* 38 (1969) 181–201.
- [79] B.E. Launder, D.B. Spalding, The numerical computation of turbulent flows, *Comput. Methods Appl. Mech. Eng.* 3 (1974) 269–289.
- [80] G.A. Gregory, M.K. Nicholson, K. Aziz, Correlation of the liquid volume fraction in the slug for horizontal gas-liquid slug flow, *Int. J. Multiphase Flow.* 4 (1978) 33–39.
- [81] J.L. Rodgers, W.A. Nicewander, Thirteen ways to look at the correlation coefficient, *Am. Stat.* 42 (1988) 59–66.
- [82] N.I. Heywood, J.F. Richardson, Slug flow of air-water mixtures in a horizontal pipe: determination of liquid holdup by  $\gamma$ -ray absorption, *Chem. Eng. Sci.* 34 (1979) 17–30.
- [83] B.D. Woods, Z. Fan, T.J. Hanratty, Frequency and development of slugs in a horizontal pipe at large liquid flows, *Int. J. Multiphase Flow.* 32 (2006) 902–925.
- [84] G.A. Gregory, D.S. Scott, Correlation of liquid slug velocity and frequency in horizontal cocurrent gas-liquid slug flow, *AIChE J.* 15 (1969) 933–935.
- [85] G.J. Zabaras, Prediction of slug frequency for gas/liquid flows, *SPE J.* 5 (2000) 252–258.

- [86] Y. Taitel, A.E. Dukler, A model for slug frequency during gas-liquid flow in horizontal and near horizontal pipes, *Int. J. Multiphase Flow*. 3 (1977) 585–596.
- [87] R. Barker, X. Hu, A. Neville, S. Cushnaghan, Assessment of preferential weld corrosion of carbon steel pipework in CO<sub>2</sub>-saturated flow-induced corrosion environments, *Corrosion* 69 (2013) 1132–1143.
- [88] H. Xu, E. Bodenschatz, Motion of inertial particles with size larger than Kolmogorov scale in turbulent flows, *Physica D* 237 (2008) 2095–2100.
- [89] G.A. Voth, A. La Porta, A.M. Crawford, J. Alexander, E. Bodenschatz, Measurement of particle accelerations in fully developed turbulence, *J. Fluid Mech.* 469 (2002) 121–160.
- [90] J.H. Gerretsen, A. Visser, Inhibitor performance under liquid droplet impingement conditions in CO<sub>2</sub>-containing environment, *Corros. Sci.* 34 (1993) 1299–1310.
- [91] A. Al-Sarkhi, T.J. Hanratty, Effect of pipe diameter on the drop size in a horizontal annular gas-liquid flow, *Int. J. Multiphase Flow* 28 (2002) 1617–1629.
- [92] Y. Xiong, AFM studies of the metallicity of single-walled carbon nanotubes and corrosion inhibitor adsorption, PhD dissertation, Ohio University, 2011.
- [93] I. Jevremovic, M. Singer, S. Nestic, V. Miskovic-Stankovic, Inhibition properties of self-assembled corrosion inhibitor talloil diethylenetriamine imidazoline for mild steel corrosion in chloride solution saturated with carbon dioxide, *Corros. Sci.* 77 (2013) 265–272.
- [94] I. Jevremovic, M. Singer, M. Achour, D. Blumer, T. Baugh, V. Miskovic-Stankovic, S. Nestic, A novel method to mitigate the top-of-the-line corrosion in wet gas pipelines by corrosion inhibitor within a foam matrix, *Corrosion* 69 (2013) 186–192.

- [95] D.F. Young, B.R. Munson, T.H. Okiishi, *A Brief Introduction to Fluid Mechanics*, John Wiley & Sons, Inc., New York, NY, 1997.
- [96] D. Carnelli, A. Karimi, J.-P. Franc, Evaluation of the hydrodynamic pressure of cavitation impacts from stress-strain analysis and geometry of individual pits, *Wear* 289 (2012) 104–111.
- [97] A.S. Grinspan, R. Gnanamoorthy, Development of a novel oil cavitation jet peening system and cavitation jet erosion in aluminum alloy, AA 6063-T6, *J. Fluids Eng.* 131 (2009) 061301-1 – 061301-8.
- [98] I. Tzanakis, D.G. Eskin, A. Georgoulas, D.K. Fytanidis, Incubation pit analysis and calculation of the hydrodynamic impact pressure from the implosion of an acoustic cavitation bubble, *Ultrason. Sonochem.* 21 (2014) 866–878.
- [99] G. Schmitt, Drag reduction by corrosion inhibitors – A neglected option for mitigation of flow induced localized corrosion, *Mater. Corros.* 52 (2001) 329–343.
- [100] E. Gulbrandsen, S. Nestic, A. Stangeland, T. Burchardt, B. Sundfaer, S.M. Hesjevik, S. Skjerve, Effect of precorrosion on the performance of inhibitors for CO<sub>2</sub> corrosion of carbon steel, in: *NACE International CORROSION 98 conference*, 1998, paper no. 13.
- [101] A. Philipp, W. Lauterborn, Cavitation erosion by single laser-produced bubbles, *J. Fluid Mech.* 361 (1998) 75–116.
- [102] A. Vogel, W. Lauterborn, R. Timm, Optical and acoustic investigations of the dynamics of laser-produced cavitation bubbles near a solid boundary, *J. Fluid Mech.* 206 (1989) 299–338.
- [103] X. Zhang, F. Wang, Y. He, Y. Du, Study of the inhibition mechanism of imidazoline amide on CO<sub>2</sub> corrosion of Armco iron, *Corros. Sci.* 43 (2001) 1417–1431.

- [104] J. Zhao, G. Chen, The synergistic inhibition effect of oleic-based imidazoline and sodium benzoate on mild steel corrosion in a CO<sub>2</sub>-saturated brine solution, *Electrochim. Acta* 69 (2012) 247–255.
- [105] I. Akhatov, O. Lindau, A. Topolnikov, R. Mettin, N. Vakhitova, W. Lauterborn, Collapse and rebound of a laser-induced cavitation bubble, *Phys. Fluids* 13 (2001) 2805–2819.
- [106] S.-H. Yang, S.-Y. Jaw, K.-C. Yeh, Single cavitation bubble generation and observation of the bubble collapse flow induced by a pressure wave, *Exp. Fluids* 47 (2009) 343–355.
- [107] A. Vogel, S. Busch, U. Parlitz, Shock wave emission and cavitation bubble generation by picosecond and nanosecond optical breakdown in water, *J. Acoust. Soc. Am.* 100 (1996) 148–165.
- [108] J.-C. Isselin, A.-P. Alloncle, M. Autric, On laser induced single bubble near a solid boundary: Contribution to the understanding of erosion phenomena, *J. Appl. Phys.* 84 (1998) 5766–5771.
- [109] R. Fortes-Patella, G. Challier, J.L. Reboud, A. Archer, Energy balance in cavitation erosion: from bubble collapse to indentation of material surface, *J. Fluids Eng.* 135 (2013) 011303-1 – 011303-11.
- [110] Y.T. Didenko, K.S. Suslick, The energy efficiency of formation of photons, radicals and ions during single-bubble cavitation, *Nature* 418 (2002) 394–397.
- [111] Y.T. Didenko, W.B. McNamara III, K.S. Suslick, Hot spot conditions during cavitation in water, *J. Am. Chem. Soc.* 121 (1999) 5817–5818.
- [112] T.J. Matula, Inertial cavitation and single-bubble sonoluminescence, *Phil. Trans. R. Soc. Lond. A* 357 (1999) 225–249.

- [113] J. Lee, S. Kentish, T.J. Matula, M. Ashokkumar, Effect of surfactants on inertial cavitation activity in a pulsed acoustic field, *J. Phys. Chem. B* 109 (2005) 16860–16865.
- [114] E.B. Flint, K.S. Suslick, The temperature of cavitation, *Science* 253 (1991) 1397–1399.
- [115] G. Zhang, C. Chen, M. Lu, C. Chai, Y. Wu, Evaluation of inhibition efficiency of an imidazoline derivative in CO<sub>2</sub>-containing aqueous solution, *Mater. Chem. Phys.* 105 (2007) 331–340.
- [116] W. Durnie, R. de Marco, A. Jefferson, B. Kinsella, Development of a structure-activity relationship for oil field corrosion inhibitors, *J. Electrochem. Soc.* 146 (1999) 1751–1756.
- [117] F. Bentiss, M. Lebrini, M. Lagrenee, Thermodynamic characterization of metal dissolution and inhibitor adsorption processes in mild steel/2,5-bis(n-thienyl)-1,3,4-thiadiazoles/hydrochloric acid system, *Corros. Sci.* 47 (2005) 2915–2931.
- [118] A. Honciuc, D.J. Baptiste, I.P. Campbell, D.K. Schwartz, Solvent dependence of the activation energy of attachment determined by single molecule observations of surfactant adsorption, *Langmuir* 25 (2009) 7389–7392.
- [119] A. Honciuc, A.L. Howard, D.K. Schwartz, Single molecule observations of fatty acid adsorption at the silica/water interface: Activation energy of attachment, *J. Phys. Chem. C* 113 (2009) 2078–2081.
- [120] J.O'M. Bockris, D.A.J. Swinkels, Adsorption of n-decylamine on solid metal electrodes, *J. Electrochem. Soc.* 111 (1964) 736–743.
- [121] D.D. Ebbing, S.D. Gammon, *General Chemistry*, ninth ed., Houghton Mifflin Company, Boston, MA, 2009.

- [122] P. Atkins, J. de Paula, *Physical Chemistry*, eighth ed., Oxford University Press, Great Britain, 2006.
- [123] G. Chen, *Nanoscale Energy Transport and Conversion: a Parallel Treatment of Electrons, Molecules, Phonons, and Photons*, Oxford University Press, Inc., New York, NY, 2005.
- [124] J. Koplik, J.R. Banavar, Continuum deductions from molecular hydrodynamics, *Annu. Rev. Fluid Mech.* 27 (1995) 257–292.

### Appendix 1. Measurement of the Mass Transfer Limiting Current Using the Ferricyanide-Ferrocyanide Couple

The mass transfer limiting current of the ferricyanide-ferrocyanide couple was measured in a three-electrode electrochemical cell, as shown in Figure A - 1.

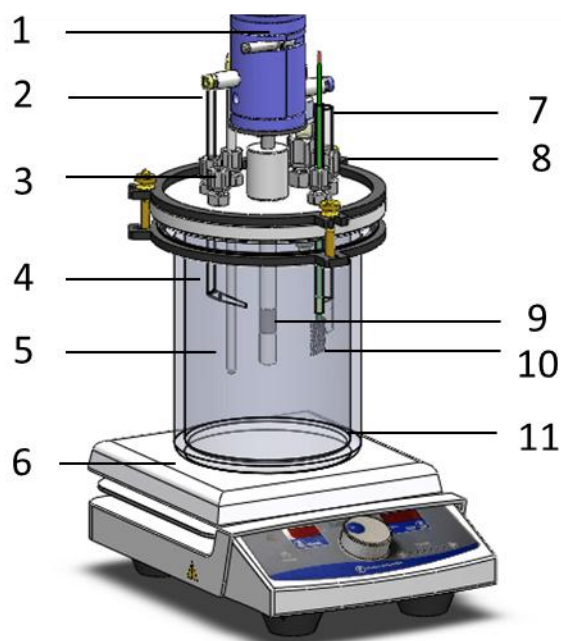


Figure A - 1: Schematic of the three-electrode electrochemical cell: (1) rotating motor; (2) reference electrode; (3) gas outlet; (4) Luggin capillary; (5) temperature probe; (6) hot plate; (7) pH probe; (8) gas inlet; (9) rotating cylinder (working) electrode; (10) counter electrode; (11) 2 L glass cell. (Courtesy of Cody Shafer)

A nickel rotating cylinder specimen (an outer diameter (OD) of 12 mm and length of 14 mm) was selected as the working electrode (WE). Saturated silver/silver chloride and platinum mesh were used as the reference electrode (RE) and counter electrode (CE), respectively. The reference electrode was connected to the working electrode using a Luggin capillary in order to reduce the ohmic drop due to solution resistance.

Before each test, an aqueous solution consisting of 0.01 M  $K_4[Fe(CN)_6]$  /  $K_3[Fe(CN)_6]$  and 2 M NaOH<sup>1</sup> was prepared in the glass cell, and was deaerated by continuously purging with nitrogen gas. In addition, the solution was kept in the dark to eliminate the decomposition of ferricyanide and ferrocyanide<sup>2</sup>.

For each rotating speed, potentiodynamic polarization (PDP) measurements were conducted, with a potential polarization range from -1.6 V to + 0.4 V (vs. open circuit potential). Clear and reproducible limiting currents were observed for both anodic and cathodic polarizations (see Figure 2-8). These limiting current values were later used to calculate the mass transfer coefficient under each flow condition.

---

<sup>1</sup> K.D. Efrid, Flow accelerated corrosion testing basics, in: NACE International CORROSION 2006 conference, 2006, paper no. 06689.

<sup>2</sup> M. Eisenberg, C.W. Tobias, C.R. Wilke, Ionic mass transfer and concentration polarization at rotating electrodes, J. Electrochem. Soc. 101 (1954) 306–320.

## Appendix 2. Procedures for Calibrating the Paddlewheel Flow Meter and the Orifice Plate Flow Meter

The liquid flow velocity in the 4-inch pipe loop was measured by using two flow meters. For higher superficial liquid velocity ( $> 1\text{m/s}$ ), a paddlewheel flow meter was used; while for lower superficial liquid velocity ( $< 1\text{m/s}$ ), an orifice plate flow meter was employed. The flow meters were calibrated against direct measurement of flow rate in a flow loop setup as shown in Figure A - 2.

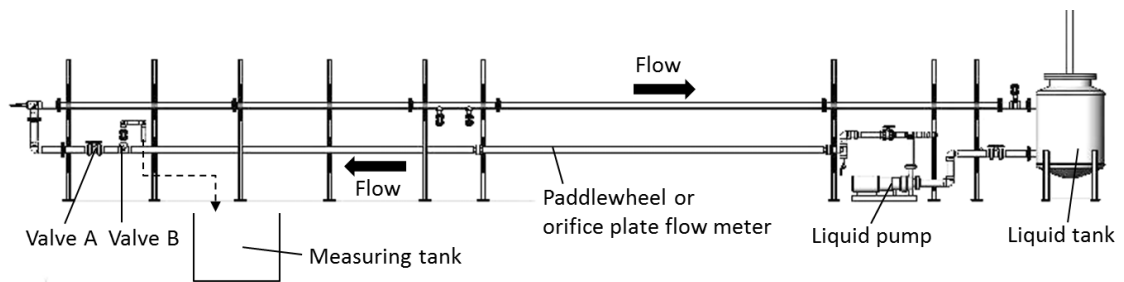


Figure A - 2: Schematic of the 4-inch loop setup for flow meter calibration.

The calibration procedure consists of several steps:

- (a) the liquid tank was filled with a fixed amount of water (350 gallons);
- (b) the main Valve A was open and the bypass Valve B was closed;
- (c) the liquid pump was set up to a predetermined speed and the flow in the loop was fully developed;
- (d) the flow was diverted to the measuring tank by opening the bypass Valve B and fully closing the main Valve A;
- (e) the real flow rate (velocity) was calculated from the measurement of the volume of discharged fluid over a given period of time in the measuring tank.

(f) the meter reading and the real flow rate for the given pump speed were documented; and step (a)-(f) were repeated at various pump speeds.

(g) the calibration coefficient was determined.

For paddlewheel flow meter, the meter reading should be linear with the real flow rate. By conducting direct flow rate measurements at several pump speeds, the calibration coefficient for the flow meter can be determined.

For the orifice plate flow meter, the pressure drop across the orifice is measured and correlated to the flow rate through Bernoulli's principle, as given by:

$$v_s = A_0 U_0 = A_p U_p = C_0 A_0 \sqrt{\frac{2\Delta p}{\rho}} \quad (\text{A } 1)$$

where  $v_s$  is the volumetric flow rate ( $\text{m}^3/\text{s}$ );  $A_0$  is the cross-sectional area of the orifice hole;  $U_0$  is the flow velocity at the orifice hole ( $\text{m}/\text{s}$ );  $A_p$  is the cross-sectional area of the pipe;  $U_p$  is the pipe flow velocity ( $\text{m}/\text{s}$ );  $C_0$  is the orifice coefficient;  $\Delta p$  is the pressure drop across the orifice (Pa); and  $\rho$  is the liquid density ( $\text{kg}/\text{m}^3$ ). The relationship between the measured pressure drop and the pipe flow velocity may be rewritten as:

$$U_p^2 = C_0' \Delta p \quad (\text{A } 2)$$

where  $C_0'$  is a calibration coefficient.  $C_0'$  can be determined by conducting pressure drop and real flow rate measurements at several pump speeds, which is illustrated by an example, as shown in Figure A - 3.

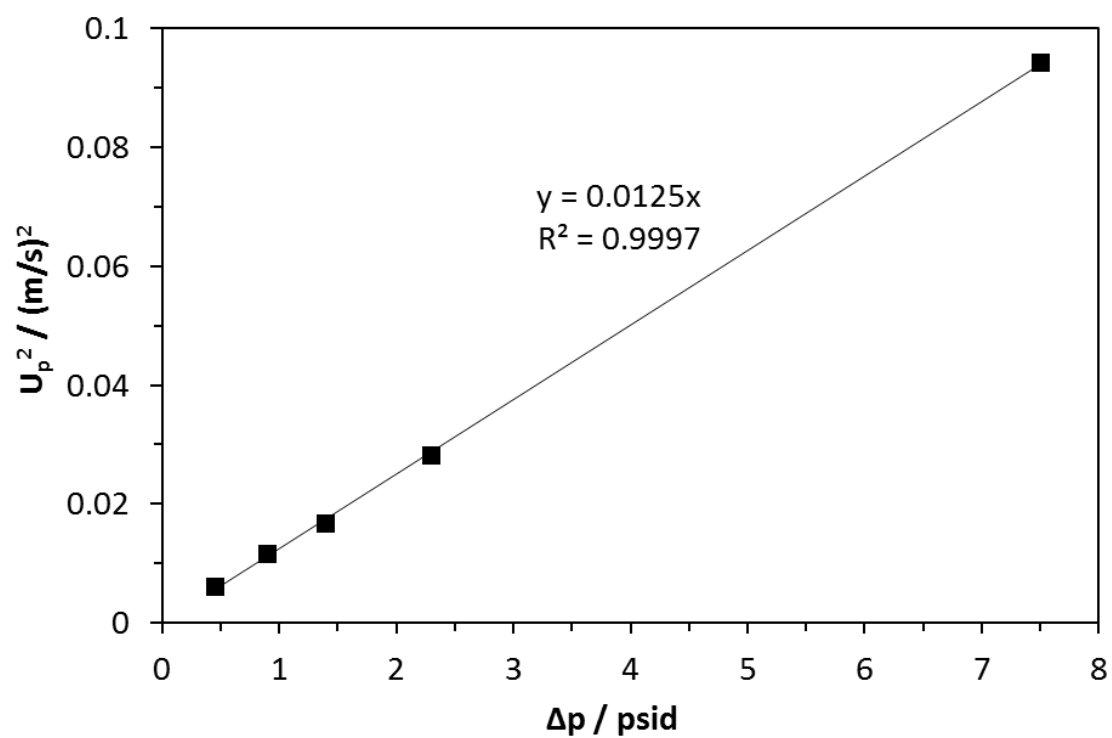


Figure A - 3: Measurements of pipe flow velocity and pressure drop across an orifice hole (2.5 cm ID) in the 4-inch ID flow loop for determination of the orifice calibration coefficient ( $C_0'$ ).

### Appendix 3. Calculation of Corrosion Rate by Weight Loss and Linear Polarization Resistance

In this study, weight loss and linear polarization resistance (LPR) measurements were used to determine the corrosion rates. Corrosion rate (CR) is defined as the metal loss in thickness per year:

$$CR = \frac{m}{\rho St} \quad (\text{A } 3)$$

where  $m$  is the metal loss;  $\rho$  is the metal density;  $S$  is the surface area of the metal; and  $t$  is the elapsed time. The measured weight losses can be directly used to calculate the time-averaged corrosion rate but with no indication of momentary corrosion rate changes.

To measure the instantaneous corrosion rate, LPR was used. LPR is a non-destructive technique for online corrosion rate monitoring and is capable of capturing the transients in a corrosion system, for example, such as the addition of an inhibitor. LPR measures the polarization resistance of the electrode ( $R_p$ ), and is correlated to the corrosion current ( $I_{corr}$ ) by the Stern-Geary equation:

$$I_{corr} = \frac{B}{R_p} \quad (\text{A } 4)$$

where  $B$  is the proportionality constant, B value (V).

The corrosion current can be used to calculate the metal loss due to the corrosion reaction from Faraday's law of electrolysis<sup>1</sup>, as given by:

---

<sup>1</sup> D.A. Jones, Principles and Prevention of Corrosion, 2nd ed., Prentice Hall, Upper Saddle River, NJ, 1996.

$$m = \frac{I_{corr}Mt}{nF} \quad (A 5)$$

where  $M$  is the molecular weight of the metal;  $t$  is the elapsed time;  $n$  is the number of electrons involved in the corrosion reaction; and  $F$  is the Faraday's constant. Substituting Equation (A 5) into Equation (A 3), the corrosion rate is calculated as:

$$CR = \frac{I_{corr}M}{nF\rho S} \quad (A 6)$$

For corrosion of steel (iron), the relationship between the corrosion current and the corrosion rate can be written as:

$$CR = 1.16 \cdot \frac{I_{corr}}{S} \quad (A 7)$$

where the units for  $CR$ ,  $I_{corr}$  and  $S$  are mm/yr, A and  $m^2$ , respectively. In order to calculate the corrosion current and the corrosion rate from LPR measurement, a proper B value needs to be assigned, as shown in Equation (A 4). The B value is defined as:<sup>1</sup>

$$B = \frac{b_a b_c}{\ln 10 (b_a + b_c)} \quad (A 8)$$

where  $b_a$  and  $b_c$  are anodic and cathodic Tafel parameters (mV/decade). The Tafel parameters can be predetermined or measured by the slopes in the potentiodynamic curves (E-log(i) curves), namely Tafel slopes.

---

<sup>1</sup> R.G. Kelly, J.R. Scully, D.W. Shoesmith, R.G. Buchheit, *Electrochemical Techniques in Corrosion Science and Engineering*, Marcel Dekker, Inc., New York, NY, 2003.

## **Appendix 4. Calculation of the Absolute Pressure at the Inlet of the CFD**

### **Simulation for Protrusion in the Thin Channel Flow Cell**

In Chapter 6, the hydrodynamic conditions surrounding the protrusion specimen were simulated by using CFD method. A large pressure decrease was found at the leading edge of the protrusion, as compared to the CFD inlet (see Figure 6-27). However, the CFD results only showed the relative pressure changes with respect to an arbitrary CFD inlet pressure. To evaluate the absolute pressure at the protrusion, the true pressure at the CFD inlet was needed, which required physical pressure measurements in the thin channel flow cell.

Pressure drop measurements between various pressure taps along the TCFC (“P1, P2, P3, P4, P5 and P6” in Figure A - 4) were conducted by using a differential pressure transducer. At the testing flow velocity of 16 m/s, the pressure drop results are given in Table A - 1. In addition, the pressure in the water tank was monitored by a pressure gauge.

Due to the computational cost, the CFD simulation only calculated the flow field 10 cm upstream and downstream of the protrusion. The relative positions of the CFD domain and the physical geometry of TCFC are shown in Figure A - 4. With the pressure drop measurements and the relative positions, the CFD inlet is calculated to be 40.5 psi (2.80 bar) smaller than that at location P1. The pressure drop between location P1 and P6 is 78.6 psi (5.42 bar). Considering the fact that the pipe length between location P6 and the water tank is approximately 160 cm and the tank pressure was measured to be 14.5 psi (1.00 bar), the actual pressure at P6 is calculated to be 1.56 bar, assuming that

the flow in the pipe section between P6 and the water tank is fully developed and the pressured drop is all due to wall shear stress. Therefore, the absolute pressure at P1 equals  $1.56 \text{ bar} + 5.42 \text{ bar} = 6.98 \text{ bar}$ ; and that at the CFD inlet is  $6.98 \text{ bar} - 2.80 \text{ bar} = 4.18 \text{ bar}$ . With knowing the true pressure at the CFD inlet, the absolute pressure surrounding the protrusion can be calculated by using the CFD results as shown in Figure 6-27.

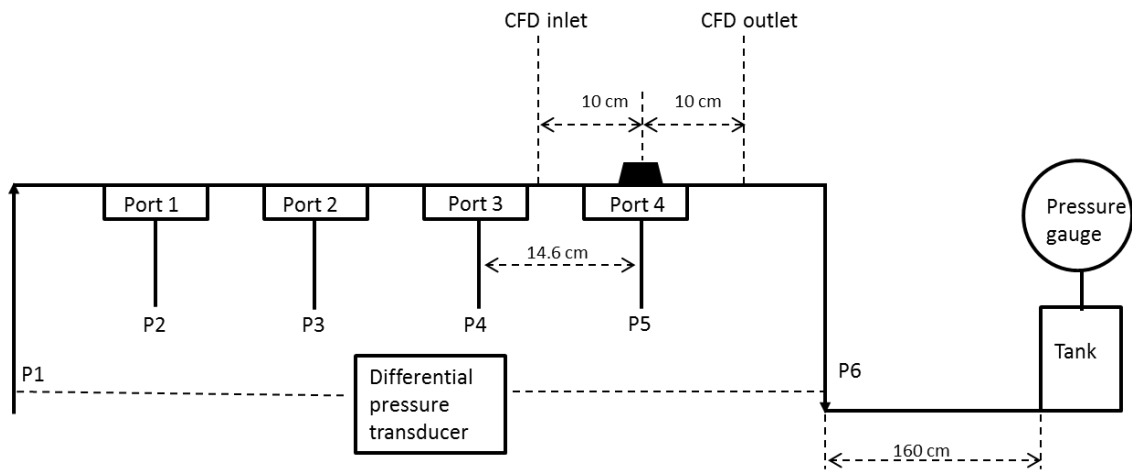


Figure A - 4: Schematic of thin channel flow cell with marked locations of pressure taps and the relative positions of the CFD domain.

Table A - 1: Pressure drop at various locations along the flow cell at

 $V = 16 \text{ m/s}$  and  $25^\circ\text{C}$ 

Location	Pressure drop / (psid)	Pressure drop / (bar)
P1 to P6	78.6	5.4
P1 to P2	26.6	1.8
P1 to P3	32.8	2.3
P1 to P4	38.6	2.7
P1 to P5	44.6	3.1



**OHIO**  
UNIVERSITY

Thesis and Dissertation Services